**Università degli Studi di Torino**

**PhD program in Pharmaceutical and Biomolecular Sciences**

# Biocatalysis of Immobilized Human Flavin-Containing Monooxygenase 1 on Nanostructured Surfaces

**Candidate: Hanna Cheropkina**

**Supervisor: Prof. Sheila J. Sadeghi**

**Coordinatore of PhD program: Prof. Roberta Cavalli**

**Academic year: 2018-2021**

# Abstract

Human flavin-containing monooxygenase 1 (FMO1) is a membrane protein bound to the endoplasmic reticulum expressed mainly in the kidney and involved in NADPH dependent oxidation reactions of soft nucleophilic heteroatoms of drugs, pesticides and dietary compounds. In this work, hFMO1 was heterologously expressed in *E. coli* and purified by affinity chromatography. The structure and functionality of purified protein were studied by using spectroscopical methods such as UV/Vis, CD, and Stopped-flow, differential scanning calorimetry and amperometry. The catalytic properties were tested *in vitro* and *in vivo* (in bacterial cells) using different substrates: drugs (methimazole, benzydamine, tamoxifen, dasatinib and vandetanib), pesticides (methiocarb, phorate and fenthion) and endogenous compounds (hypotaurine and indole).

The catalytic activity of hFMO is dependent on the formation and stability of the C4a hydroperoxyflavin intermediate that is responsible for the monooxygenation reaction. The formation of this highly stable C4a hydroperoxyflavin intermediate of hFMO1 upon reduction by NADPH and in the presence of $O_2$ was demonstrated by stopped-flow spectrophotometry. The measured half-life of this flavin intermediate revealed it to be stable and not fully re-oxidized even after 30 min at 15 °C in the absence of substrate, the highest stability ever observed for a human FMO. In addition, the investigated uncoupling reactions of FMO1 demonstrate that this enzyme is <1% uncoupled in the presence of the substrate, forming small amounts of $H_2O_2$ with no observable superoxide as confirmed by EPR spin trapping experiments. These data are consistent with the higher stability of the hFMO1 intermediate and shed light on the possible reason for the different behaviors of this enzyme in comparison with other members of the FMO family.

To assess the feasibility of an *in vitro* bioelectrochemical platform, hFMO1 was immobilized on glassy carbon electrodes modified with graphene oxide (GO) and cationic surfactant didodeycyldimethylammonium bromide (DDAB). Uv-vis, contact angle and AFM measurements support the effective decoration of the GO sheets by DDAB which appear as 3 nm thick structures. To demonstrate the possibility to mimic the metabolic pathway of xenobiotics using a bioelectrochemical platform, the pesticide phorate was tested. Two bioelectrodes were used in a tandem system with hFMO1 and CYP3A4 resulting in both phorate sulfoxide as well as phoratoxon sulfoxide i.e., the same two metabolites produced in humans.

Finally, another biotechnological application of FMOs as environmentally-friendly biocatalysts was demonstrated by the oxidation of indole leading to the production of indigoids such as indigo and indirubin. In this case, in addition to FMO1 a Baeyer-Villiger monooxygenase was also investigated resulting in yields of indirubin up to 5 mg/L and 138 mg/L respectively.

# Contents

# Chapter 1

# General Introduction

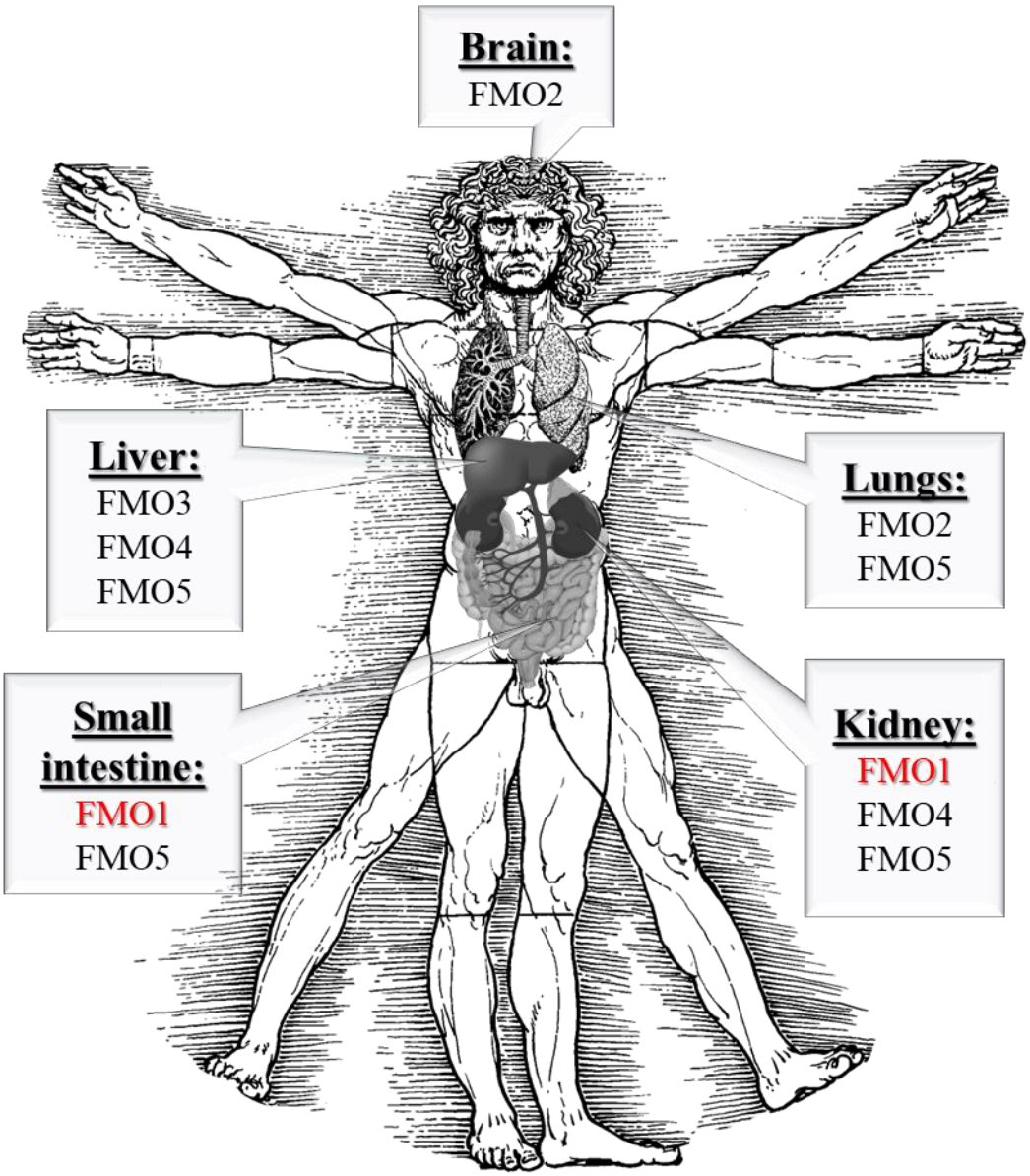

## 1.1 Human drug metabolizing enzymes

Understanding the mechanisms behind drug and xenobiotic metabolism in the human body is crucial for pharmaceutical, medical and health sciences. Investigating the mechanisms of the enzymatic reactions and determination of the metabolites being formed gives us the key to understanding the principles behind product formation, transformations and interactions between different drug metabolising enzymes.

As already well documented, human drug metabolism is the chain of biochemical reactions that occurs in our body and is driven by enzymes that mainly carry out two types of reactions: functionalization reactions known as Phase I reactions that include oxidations, reductions, hydrations/dehydrations and, conjugation reactions known as Phase II reactions that add endogenous hydrophilic groups to the original molecule in order to form water-soluble inactive compounds that can be excreted from the body [1]. Therefore, from a chemico-physical perspective drug metabolism lowers the hydrophobicity of the parent drug resulting in faster excretion [2]. Nevertheless, biotransformation reactions can sometimes result in the activation of a prodrug or in the generation of highly toxic metabolites [3,4]. Therefore, understanding how a drug can be modified by drug-metabolizing enzymes is crucial to predict its functionality upon administration [5].

Phase I reactions are mainly driven by two major classes of oxidative enzymes: cytochromes P450 (CYP) and flavin-containing monooxygenases (FMOs). Human FMOs are responsible for approximately 2.2% of all metabolic reactions in the human body and about 5.4% of Phase I metabolic reactions.

## 1.2 Human FMO family

The human flavin-containing monooxygenases (hFMOs) are Phase I drug metabolizing enzymes with a flavin adenine dinucleotide (FAD) as cofactor and are widely distributed in the human body. Humans possess five functional FMO genes, designated FMO1, FMO2, FMO3, FMO4 and FMO5 [6]. This is the family of enzymes bound to the membrane of the endoplasmic reticulum and mainly expressed in tissues listed in Table 1 (created by using the information published on Human Protein Atlas - www.proteinatlas.org)

**Table 1:** Summary of RNA expression of different hFMOs

| Human Tissues | FMO1 | FMO2 | FMO3 | FMO4 | FMO5 |
|---|---|---|---|---|---|
| Brain | ExL/ND | Low | Low | Low | Low |
| Endocrine tissues | Low | Medium | Low | Low | High |
| Respiratory system (Lung) | Low | High | Low | Low | Medium |
| Proximal digestive tract | Low | High | Low | Low | Medium |
| Gastrointestinal tract | Medium | Low | Low | Low | High |
| Liver & Gallbladder | Low | Low | High | High | High |
| Pancreas | Low | Low | Low | Low | Medium |
| Kidney & Urinary bladder | High | Low | Low | Medium | High |
| Male tissues | ExL/ND | Low | Low | Low | Low |
| Female tissues | Low | Medium | Low | Low | Medium |
| Muscle tissues | Low | High | Low | Low | Low |
| Connective & Soft tissue | Low | High | Medium | Low | Low |
| Skin | Low | Low | Low | Low | Low |
| Bone marrow & Lymphoid tissues | Low | Low | Low | Low | Low |

Where: **High** - > 50 nTPM, **Medium** - > 20, < 50 nTPM, **Low** - < 20 nTPM, **ExL/ND** - < 1 nTPM

Proteins of the FMO family prefer soft nucleophiles, sulfur- and nitrogen-containing heteroatoms as substrates which include many different types of organic compounds, pesticides, drugs and xenobiotics [6–9].

All members of hFMO family act in the same way with their catalytic cycle shown in Figure 1. However, the kinetic parameters and stability of the formed intermediates are different for each enzyme which causes variation in the substrate preferences and their natural functions [10–14]. The catalytic cycle consists of two main parts: reducing of the enzyme-bound FAD by NADPH/NADH to $FADH_2$, Figure 1(1) and reoxidation of the prosthetic group to its natural state, Figure 1(2-7) by binding of molecular oxygen to the reduced form with the formation of the reactive FAD-OOH intermediate. This intermediate is stabilized by $NADP^+/NAD^+$ until the substrate reaches the active site and becomes monooxygenated. Subsequently, the second oxygen atom is coupled with two hydrogens and produces water with complete reoxidation of the FAD cofactor.

Besides the main reactions within the catalytic cycle, there are other reactions named "uncoupling reactions" that result in the formation of reactive oxygen species forming $H_2O_2$ or superoxide as shown in Figure 1(a,b,c).

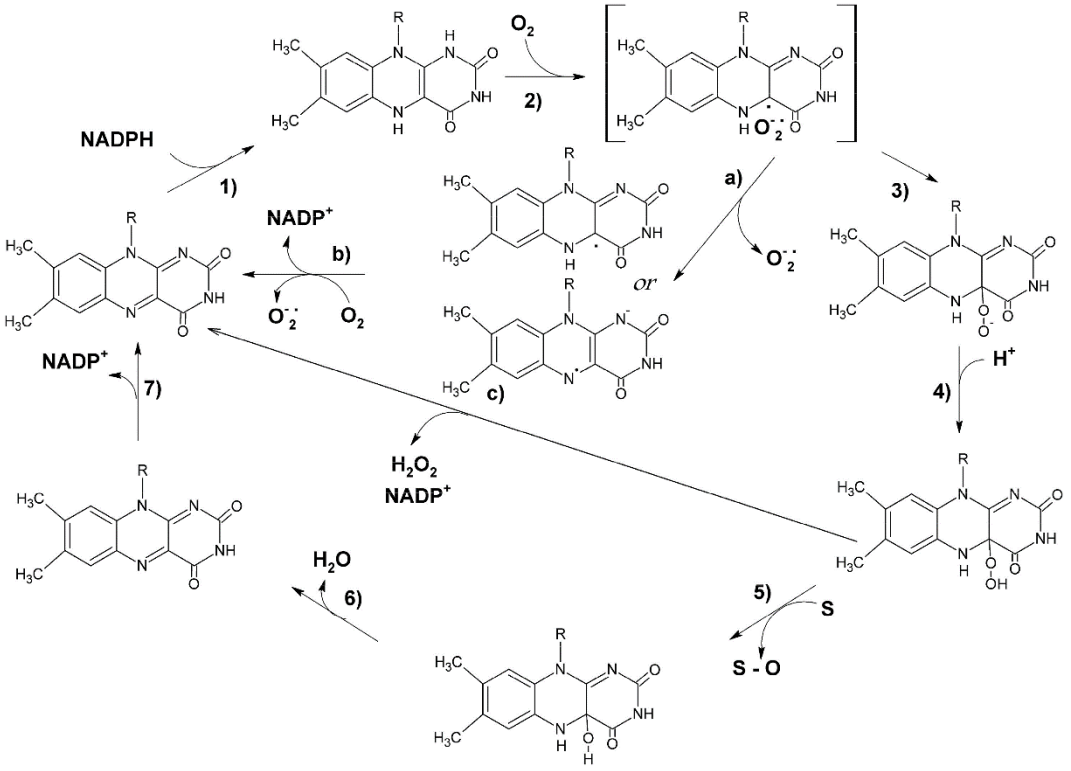


**Figure 1:** General scheme of the catalytic cycle of human FMOs [14]

As mentioned earlier, hFMOs are involved in a broad range of oxidation reactions with substrates including drugs, pesticides and dietary-derived compounds. However, the substrate spectrum of each member of this family of enzymes is different [15,16]. In addition, in the specific case of hFMO5 it has been shown that it is also capable of carrying out Baeyer–Villiger oxidation reactions [17–19].

## 1.3 Flavin-containing monooxygenase 1

The first evidence of FMO1 was presented in 1970s by Ziegler's lab [20] followed by the determination of its DNA sequence and mapping of this single gene to chromosome 1 by Dolphin and Shephard [21]. The protein contains 532 amino acid residues and has a molecular weight of approximately 60.32 kDa. It is expressed mainly in fetal liver and kidney tissues, but in adults it is detected only in the kidney, small intestine and skin [22,23].

It has been found that hFMO1 is highly polymorphic and these mutations may have an impact on the activity of the enzyme [9,24,25]. The most common polymorphic variants found are H97Q, I303V, I303T, R502X, T249T and V396V

[26] but approximately 129 single nucleotide polymorphic variants of FMO1 have been reported in the SNP database [27]. From a personalized medicine point of view, polymorphism plays an important role in drug metabolism and clearance which might lead to different response to therapy.

The hFMO1 protein structure has not been elucidated as yet, but recently Bailleul and colleagues successfully crystalized and obtained the X-ray crystal structure of an ancestral FMO1, AncFMO1, with 89.8% identity to the human FMO1 [28] shown in Figure 2A. The enzyme contains two distinct domains that are NAD(P)H and FAD-binding domains, characteristic of the human FMOs [29]. The structure also has a large transmembrane C-terminal helix, Figure 2B (dark brown zone), that plays the role of the anchor to the membrane [16,30].

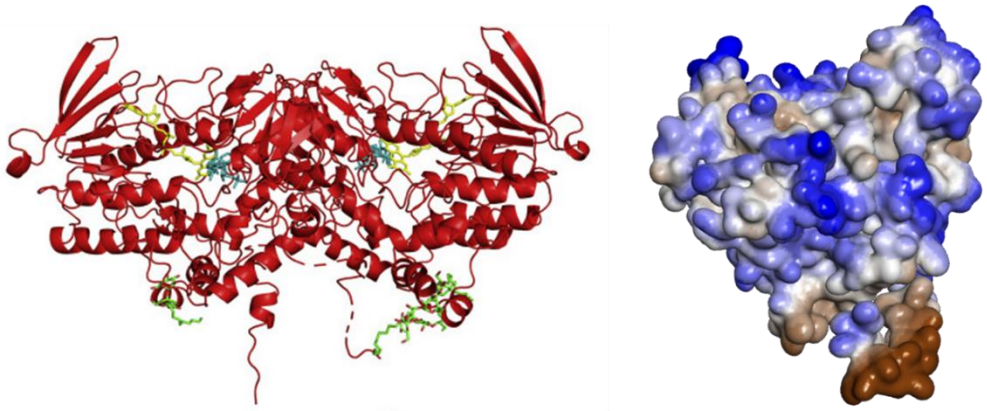

A B

**Figure 2: (A)** Dimeric representation of the AncFMO1 crystal structure. **(B)** Hydrophobicity surface representation wherein dark red demonstrates the large hydrophobic C-terminal helix that provides the interaction of the enzyme with the membrane.

Analysing the active site of the AncFMO1 the authors observed some structural differences between their obtained model and previously published data that point to the creation of a wider and hydrophobic pocket at the base of the active site. This observed structural difference might cause differences in the enzyme's activity.

Like other members of the hFMO family, FMO1 catalyzes the oxygenation of nitrogen-, sulfur-, phosphorus, selenium and some carbon-containing xenobiotics with high stereoselectivity [26,26,31,32]. But what is the role of this enzyme in the human body? Recently, Veeravalli et al. reported that hFMO1 is involved in taurine

production from hypotaurine [33]. Taurine is one of the most abundant amino acids that play an important role in cell volume regulation and is an essential organic osmolyte. The identification of hFMO1 as the enzyme responsible for the synthesis of this compound is therefore important.

As hFMO1 enzyme is expressed not only in the kidney but also other tissues such as the small intestine, adrenal gland, breast, skin, thymus and female tissues, it is also involved in drug metabolism of the substrates specific for those tissues. Table 2 reports the main substrates that can be metabolized by hFMO1.

**Table 2:** Substrates of human FMO1

| Substrate | Role | Reaction | Reference |
|---|---|---|---|
| **N1-Substituted-6-arylthiouracils** | Selective irreversible inhibitors of human myeloperoxidase | S-oxygenation | [34] |
| **4-fluoro-N-methylaniline** | Organ toxicant | C-oxygenation | [35] |
| **Aldicarb** | Carbamate insecticide | S-oxygenation | [36] |
| **Arecoline** | Nicotinic acid-based mild parasympathomimetic stimulant alkaloid | N-oxygenation | [37] |
| **Benzydamine** | Anti-inflammatory | N-oxygenation | [28,38–40] |
| **Cabozantinib** | Antitumor drug for patients with multiple cancer types | N-oxygenation | [41] |
| **Carbophenothion** | Insecticide | S-oxygenation | [31] |
| **Cediranib** | Highly potent vascular endothelial growth factor (VEGF) inhibitor | N-oxygenation | [42] |
| **Cimetidine** | Histamine H2-receptor antagonist of therapeutic utility in the treatment of peptic ulcer disease and gastric hypersecretory syndromes | S-oxygenation | [32] |
| **Darexaban maleate** | Anticoagulant and antithrombotic, direct competitive factor Xa inhibitor | N-oxygenation | [43] |
| **Demeton-O** | Insecticide and acaricide | S-oxygenation | [31] |
| **Deprenyl** | MAO-B inhibitor | N-oxygenation | [44] |
| **Disulfoton** | Organophosphate acetylcholinesterase inhibitor used as an insecticide | S-oxygenation | [45] |
| **Ethiofencarb** | Pesticide | S-oxygenation | [31] |
| **Ethionamide** | Antitubercular drug | S-oxygenation | [46,46–48] |
| **Fenthion** | Organothiophosphate insecticide, avicide, and acaricide | S-oxygenation | [26,31] |
| **Fonofos** | Organophosphate acetylcholinesterase inhibitor used as a pesticide | S-oxygenation | [31] |
| **GSK5182** | Anti-diabetic agent, inverse agonist for estrogen-related receptor γ | N-oxygenation | [49] |
| **Hypotaurine** | Endogenous neurotransmitter | S-oxygenation | [33] |
| **Imipramine** | Tricyclic antidepressants | N-oxygenation | [26] |
| **Ketoconazole** | Antifungal agent | N-hydroxylation | [50,51] |

| | | | |
|---|---|---|---|
| **Lorcaserin** | Selective 5-hydroxytryptamine 2C receptor agonist and a potential therapeutic agent for weight management | N-hydroxylation | [52] |
| **Methamphetamine** | Potent central nervous system (CNS) stimulant | N-oxygenation | [44] |
| **Methimazole** | Antithyroid agent that inhibits the actions of thyroid peroxidase | S-oxygenation | [26,39,53] |
| **Methiocarb** | Acetylcholinesterase inhibitor, and neurotoxin that is used as a pesticide | S-oxygenation | [31,45] |
| **MK-0767** | Peroxisome proliferator-activated receptor agonist | S-oxygenation | [54] |
| **N-(3R)-1-azabicyclo[2.2.2]oct-3-ylfuro[2,3-c]pyridine-5-carboxamide** | $\alpha_7$ nicotinic acetylcholinergic receptor agonist | N-oxygenation | [55] |
| **N,N-dimethylamphetamine** | Central nervous system stimulant | N-oxygenation | [56] |
| **Nomifensine** | Antidepressant drug with a powerful inhibitory effect on dopamine uptake | N-oxygenation | [57] |
| **N-substituted N′-(4-imidazole-ethyl)thioureas** | Histamine H3 antagonist, HIV-1 non-nucleoside reverse transcriptase inhibitors, cytotoxins | S-oxygenation | [58] |
| **Olopatadine** | Histamine H1 receptor-selective antagonist | N-oxygenation | [59] |
| **Pargyline** | MAO-B inhibitor with antihypertensive properties | N-oxygenation | [22] |
| **Phorate** | Organophosphorus insecticide and acaricide | S-oxygenation | [45] |
| **Procainamide** | Type I antiarrhythmic agent | N-oxygenation | [60] |
| **Quazepam** | Sedative and hypnotic used for insomnia treatment | Desulfuration | [61] |
| **S-Allyl-L-cysteine** | Antioxidant and antiproliferative effects on melanoma and prostate carcinoma cells | S-oxygenation | [62] |
| **Selenomethionine** | Amino acid, major component of selenium used for cancer chemoprevention in several clinical trials | Se-oxygenation | [63,64] |
| **S-methyl-esonarimod** | Inhibitor of the inflammatory cytokines production | S-oxygenation | [64] |
| **S-MethylN,N-diethyldithiocarbamate** | Metabolite of the alcohol deterrent disulfiram | S-oxygenation | [65] |
| **SNI-2011** | Parasympathomimetic and muscarinic agonist | N-oxygenation | [66] |
| **S-phenyl** | Pesticide | S-oxygenation | [31] |
| **Sulindac sulfide** | Non-steroidal anti-inflammatory drug | S-oxygenation | [39] |
| **Sulprofos** | Organophosphate acetylcholinesterase inhibitor used as a pesticide | S-oxygenation | [45] |
| **Tamoxifen** | Non-steroid anti-estrogen for the treatment of breast cancer | N-oxygenation | [67–69] |
| **Tazarotenic acid** | Potent and selective agonist of the retinoid receptor | S-oxygenation | [70] |
| **TG100435** | Multi-targeted Src family kinase inhibitor with demonstrated anticancer activity in preclinical species | N-oxygenation | [71] |
| **Thiacetazone** | Antitubercular drug | S-oxygenation | [46,48] |

| | | | |
|---|---|---|---|
| **Thione AGN11** | Pulmonary toxicants | S-oxygenation | [72] |
| **Tozasertib** | Anticancer chemotherapeutic pan-aurora kinase inhibitor | N-oxygenation | [39] |
| **Vandetanib** | Anti-thyroid-cancer drug | N-oxygenation | [73,74] |
| **Voriconazole** | Antifungal agent | N-oxygenation | [75] |
| **Xanomeline** | Muscarinic acetylcholine receptor agonist | N-oxygenation | [76] |

## 1.4. Bioelectrochemistry

Each year more areas are investigated to improve personalized medicine approaches which aim to help prescribe the specific therapy for the single patient to obtain the maximal drug efficiency and decrease the cost of the treatment. Genetic differences [77], family health history [78], place of residence and food preferences [79] play a key role in the response of the patient to the applied therapy. This is why different strategies for the implementation of personalized medicine in various fields such as oncology, neurodegenerative and genetic diseases [80–82] have been investigated.

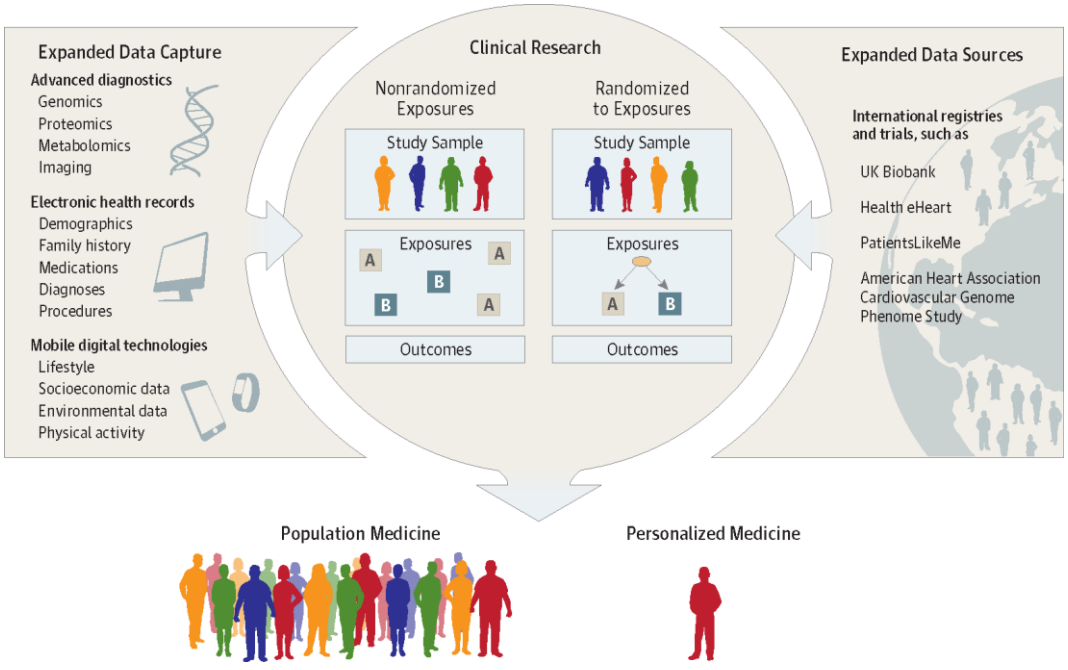


**Figure 3:** Tools being used in clinical research to understand the population and personalized medicine [83]

Digitalization and miniaturizing already help to create the devices, such as biosensors, for personal usage and monitoring the important vital parameters,

collecting them with ones own smartphone and, if required, staying in contact with the personal doctor by using novel telematic medicine.

Multidisciplinary sciences such as bioelectrochemistry are currently in the forefront of research due to interest in direct measurements of the interactions of biologically active molecules with artificial functional devices. Bioelectrochemistry itself contains a wide range of multidisciplinary scientific research fields such as biology, biophysics, electrochemistry and chemistry. Today the main aims of the scientific interest in the bioelectrochemical area could be divided into the following applications as shown in Figure 4: Pharmaceutical and Biotechnology, Bioenergetics, Biolayers and Biomembranes, Biosensors and Electrified interfaces, Electric and magnetic field and, Lab-on-chip. One of the most promising fields of study at all levels of biotechnology, pharmacology, and medicine is personalized and point-of-care approaches. Developing sensitive, selective, usable, low-cost, and rapid devices for controlling the concentrations of drugs, steroids, hormones, sugars, xenobiotics and hazardous chemicals in the human body will help to provide the correct diagnosis of various illnesses and predict the reaction of the organism with selected therapies. Moreover, the creation of a rapid system for monitoring the pharmacokinetics parameters of novel drugs or their full metabolic pathway in one-pot reactions could be a powerful approach to personalized medicine.

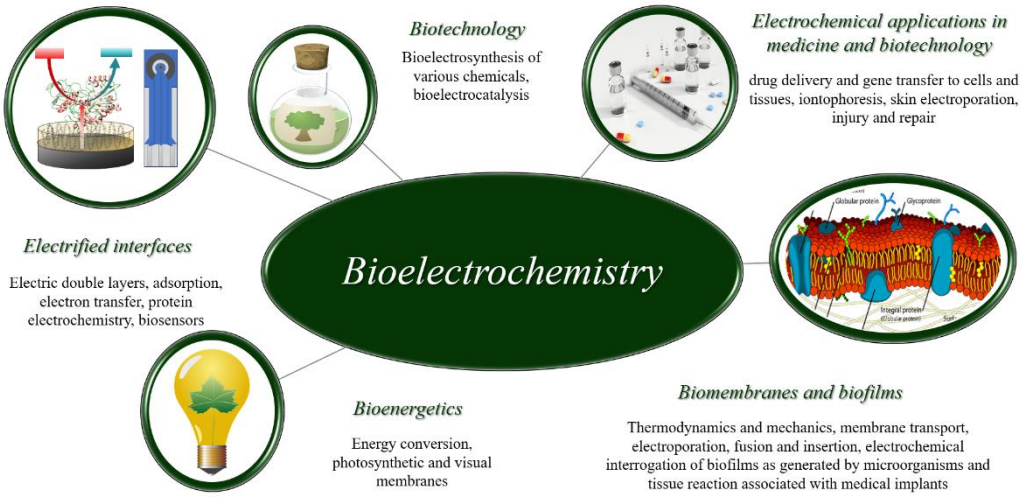


**Figure 4:** Bioelectrochemistry and its applications

The mimicking of the metabolism pathway, screening and estimating the properties and applications of new medications by using enzyme-based electrodes

is a way to personalized medicine. The metabolism of commonly used drugs and the main detoxification processes are carried out in Phase I, which correspond to the oxidation, reduction and hydrolysis reactions [84] mainly by the two human enzyme families of CYPs [85,86] and FMOs [87].

Recently, one of the main areas of research in biosensing has been focused on anticancer drugs tamoxifen, ftorafur, cyclophosphamide, ifosfamide [88,89] and antituberculosis drugs ethambutol, pyrazinamide, isoniazid and rifampicin [90,91]. The main target of these sensors is the detection and quantification of relevant metabolites in human blood plasma or urine to provide strict regulation and dosage during therapy.

Immobilized proteins on the electrode could be activated through the electron and proton transfer without the necessity of reducing agents such as NADPH or NADH. In the case of CYPs and FMOs that are membrane-bound human proteins, their immobilization on electrode surfaces has proven to be quite challenging, however, different strategies for their covalent and non-covalent immobilization have been reported by different research groups [92]. One of the most important limitations is the sensitivity of the signal and deceleration of electron transfer from the electrode to the immobilized protein active center through the surfactant layer. In order to miniaturize the electrode and enhance the sensing characteristics, different nanostructured materials have been used such as nanoparticles of noble metals, high-surface metal-oxides and organic polymers, 1D, 2D, and 3D nanostructured materials (graphene and its derivates, nanotubes, nanorods, nanoplates, nanodendrites), different types of lipids and surfactants, quantum dots, etc. The main advantages of using nanostructured materials for the design and fabrication of electrochemical biosensors are their efficient electrocatalyst properties, high surface area or surface-to-volume ratio, enhancement of electron transfer, high current density and capacity to deposition of molecules [93].

Graphene and its derivative graphene oxide have occupied a dominant place in the biosensing field due to their large surface area and efficient electrochemical and catalytical properties [94,95]. The biocompatibility of these materials has made them an excellent couple for the various biological structures such as DNA, enzymes, cell and tissues.

In the protein electrochemistry field other materials have also been used such as particles of gold, silver and palladium. [96]. The advantages of using carbon nanotubes (CNT) in the biosensing field is mainly due to their large

electrochemically active surface area and high sensitivity [97]. Nanoporous structures such as anodic aluminium oxide [98] and titanium oxide [99], are also promising materials due to their unique structure and tight regulation of shape, type and depth.

For the immobilization of membrane proteins on electrode surfaces, entrapment in lipid bilayers is the most common strategy. The lipids and surfactants are the optimal environments to stabilize these proteins in the native state. The structure, orientation and compactness of lipids could easily be controlled according to particular needs. The most commonly used lipids for enzyme biosensors are didodecyldimethylammonium bromide (DDAB), polydiallyldimethylammonium chloride (PDDA), cardiolipin and phospholipids [100]. Functionalization of the enzymatic electrode should be done according to the type and function of the protein and also the reaction conditions.

**Bioelectrochemistry of hFMO1**

In literature, the electrochemical approaches using hFMO1 were investigated initially to create a kind of "biosniffer" sensor for the detection of various sulfur and nitrogen-containing toxic and hazardous volatiles such as triethylamine, ammonia, trimethylamine (TMA), dimethyl sulfide and methylmercaptan in the liquid and gaseous phases [101–104]. The bioelectrochemical sensor consisted of a modified dialysis membrane with hFMOs (1, 3 and 5) within a Clark-type dissolved oxygen electrode. The principle of detection was based on the consumption of dissolved oxygen as a result of the enzymatic oxidation reaction of the enzymes in the presence of the specific substrate. Amplification of the electrode output signal was carried out by the substrate regeneration system base on ascorbic acid. Measurements were carried out at -600 mV (vs Ag/AgCl), with the sensor showing good selectivity and specificity for the FMO substrates tested.

Another method for the detection of trimethylamine was based on hFMO3 conductometric biosensor [105]. The enzyme was immobilized onto the surface of gold-interdigitated electrodes by using a cross-linking method together with bovine serum albumin in saturated glutaraldehyde vapor. The sensitivity of the obtained sensor was tested under certain optimal conditions in the range of TMA concentrations from 10 to 400 μg/mL. Improved enzymatic glutaraldehyde-BSA electrode was demonstrated by Castrignano et al. [106]. Redox properties of the bioelectrode were analyzed by cyclic voltammetry. Bioelectrocatalytic properties of the hFMO3 electrode were tested on well-known substrates such as

trimethylamine, ammonia, triethylamine and benzydamine. The kinetic parameters were estimated by the fitting of electrode response according to Michaelis–Menten equation owing to the titration in the presence of increasing concentrations of analytes under similar conditions.

Another type of trimethylamine bioelectric sensor for fish freshness detection was reported based on amperometric and impedimetric measurements [107]. Human FMO3 was covalently bound by exposed amine groups of lysine residues to the N-hydroxy phtalamide reactive group of poly(N-hydroxyphtalimidepyrrole-co-pyrrole) copolymer. The fresh enzymatic electrode was functionalized by ferrocene groups which played a role as redox mediator. The sensor's amperometric response upon the changing of TMA concentration was followed by decrease in the oxidation signal of the ferrocenyl groups. This was caused by the conversion of TMA to its N-oxide form as a result of reaction mediated by hFMO3. Detection measurements carried out by electrochemical impedance spectroscopy demonstrated similar behavior.

In order to improve the stability of the enzyme immobilized on the electrode it is best to covalently link it to the electrode surface. Creating this kind of interaction with human enzymes such as the FMOs is quite challenging, but Sadeghi and colleagues managed to solve this issue and provided the first successful immobilization of hFMO3 on gold and glassy carbon (GC) electrodes to obtain direct electron transfer for drug metabolism studies [88]. In the reported work, the GC electrode was modified by a mixture of cationic surfactant DDAB and pure hFMO3. The covalent binding strategy was chosen for the immobilization of the enzyme on the gold electrode by dithio-bismaleimidoethane (DTME) linkers. Formation of the maleimide-terminated crosslinkers helped to covalently bind the enzyme via the surface exposed sulfhydryl groups of cysteine residues. Bioelectrocatalytic properties of the immobilized protein were tested with two common substrates of hFMO3: benzydamine and tamoxifen.

Another reported method of modification of the gold electrode is by using naphthalenethiol (Np-S) thin-film before hFMO1 and hFMO3 immobilization [108]. Direct electron transfer and enzymatic catalytic activity were demonstrated for both bioelectrodes.

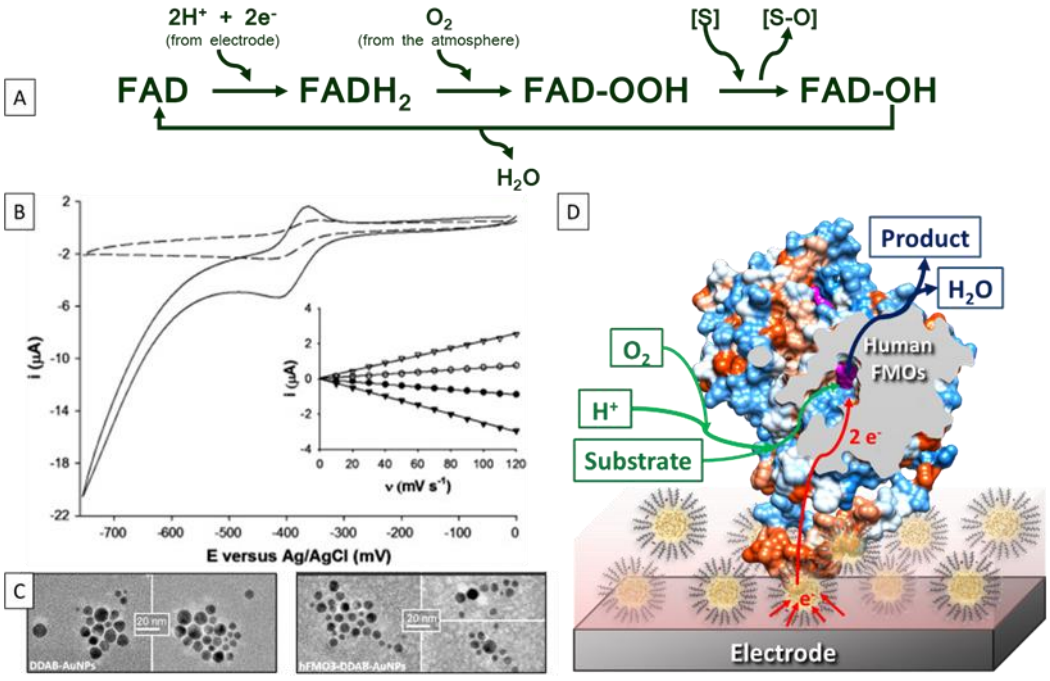


**Figure 5: (A)** Reaction scheme for the electrochemically driven catalytic cycle of the hFMOs. **(B)** Cyclic voltammograms of hFMO3 on DDAB glassy carbon electrodes in the absence (dashed line) and in the presence (solid line) of AuNPs. Inset: plot of cathodic (filled symbols) and anodic (empty symbols) peak currents versus scan rate for hFMO3 on DDAB glassy carbon electrodes in the absence (circles) and in the presence (triangles) of AuNPs **[109]**. **(C)** TEM images of DDAB stabilized AuNPs in the absence and in the presence of hFMO3 protein **[109]**. **(D)** Schematic representation of immobilized hFMO protein coupled with AuNPs.

The first successful implementation of nanostructured surfaces such as gold nanoparticles (AuNPs) coupled with hFMO3 protein was demonstrated by Castrignanò and co-workers [109]. The glassy carbon working electrode was modified by AuNps (6.5 - 8.5 nm in diameter) protected and stabilized with DDAB in the presence of purified hFMO3. As was reported, entrapped protein with nanoparticles inside the cationic surfactant layer showed an enhanced electrode response and improved electron transfer in comparison to the electrode without gold nanoparticles as shown in Figure 5. Square-wave voltammetry measurements also demonstrated a higher current response in the presence of AuNPs as expected. The electrocatalytic properties of hFMO3-DDAB-AuNPs electrode were tested in the presence of sulindac sulfide and benzydamine as substrates and estimated kinetic parameters were found to be in agreement with those published in the literature obtained by other analytical methods which characterized the current system as an optimal model for the therapeutic drugs screening. The next nanostructured material

that was tested was graphene oxide [110,111]. The hydrophilic properties of this material and the presence of a huge amount of oxygen-containing and carboxylic groups help to provide different types of surface functionalization to create an optimal environment for biomolecules used for biosensing and drug metabolism investigations. Enhancement of the direct electrochemical response in the presence of graphene oxide was studied with hFMO3 and its two polymorphic variants E158K and E308G. All proteins were immobilized onto a glassy carbon electrode modified by cationic surfactant DDAB and entrapped with graphene oxide inside. The electrocatalytic efficiency of the enzymes in the presence of graphene oxide was tested for benzydamine, tamoxifen and sulindac sulfide.

In the specific case of hFMO1, some of the immobilization strategies are summarized in Table 3.

**Table 3:** The main immobilization strategies reported for human FMO1

| **Human enzyme** | **Electrode system** | **Drug** | **Ref.** |
|---|---|---|---|
| **FMO3** | GC/DDAB/hFMO3<br>Au/DTME/hFMO3 | benzydamine and tamoxifen | [88] |
| | GC/hFMO3-BSA | benzydamine | [106] |
| | GC/DDAB/hFMO3<br>GC/AuNps/DDAB/hFMO3 | sulindac sulfide and benzydamine | [109,112] |
| | GC/DDAB/hFMO3<br>GC/DDAB/GO/hFMO3<br>GC/DDAB/GO/E308G<br>GC/DDAB/GO/E158K | benzydamine, tamoxifen and sulindac sulphide | [110,111] |
| **HLM** | GC/Au@RGO-CS/PDA/HLM | ketoconazole, testosterone, progesterone, estrone | [113] |
| | EPG/MNPamine/HLM | diclofenac | [114] |

Finally, the demonstration of various ways of using hFMOs coupled with nanostructured materials in electrochemical systems opens the possibility of creating *in vitro* bioelectrochemical platforms for high throughput drug screening, metabolite identification and more importantly, mimicking the fate of drugs during their metabolism in humans.

# Chapter 2

# Expression, purification, and characterization of hFMO1

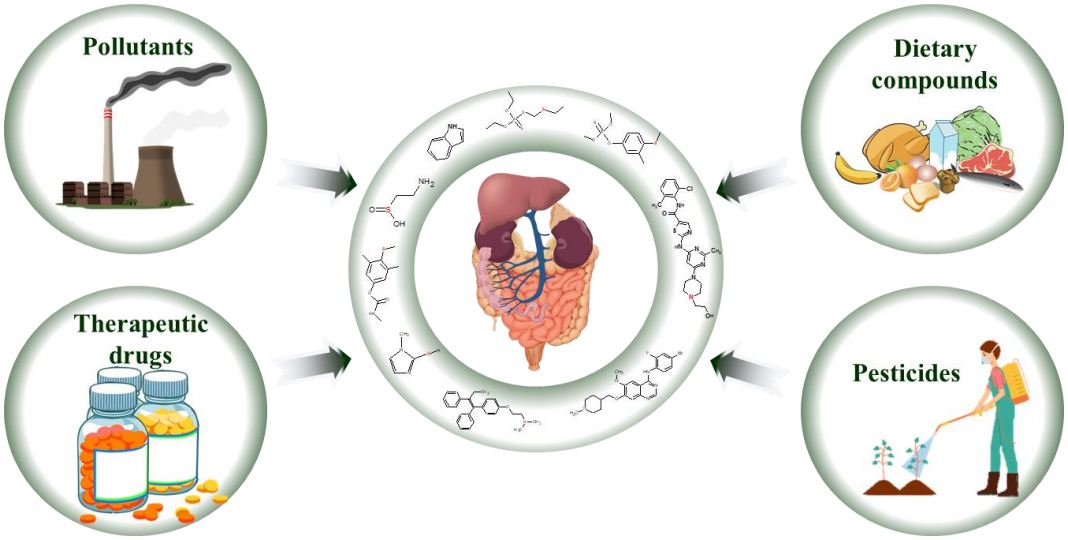

## 2.1. Introduction to the production of the recombinant hFMO1

Human FMO1 together with other monooxygenases plays an important role in different soft nucleophilic oxidation reactions involving the metabolism of drugs and xenobiotics. Investigation of its catalytic mechanism and properties are of high interest in pharmacology and toxicology fields. Dolphin and Shephard [21] isolated the full-length cDNA of hFMO1 from the human liver libraries and found that it encoded a polypeptide of the target enzyme with 532 amino acid residues and FAD and NADPH binding sites. Later studies showed that the sequence similarity between human flavin-dependent monooxygenases is in the range of 50% to 60% [115] but the identity between human and pig FMO1 was found to be higher, around 88% [21].

The primary structure analysis of hFMO1 was carried out by Phillips and co-workers [22]. They demonstrated the presence of a hydrophobic region located near the C-terminus which was identified as the small domain that could assist in the protein's attachment to the membranes of the endoplasmic reticulum. On the basis of this knowledge, the first recombinant hFMO1 was expressed in a baculovirus expression vector system [9,38,53,69,73,116,117] and purified using anion exchange diethylaminoethyl (DEAE) and hydroxyapatite chromatography [116]. Expression of hFMO1 in *E. coli* expression systems was also reported by other research groups [39] [28].

In the current work, the active recombinant hFMO1 was expressed in *E. coli* and purified from the membrane fractions using anionic and affinity chromatography. As the process of purification of folded and active human membrane proteins is generally challenging the main parameters such as pH, temperature and the amount and type of detergent should be regulated [116–119].

Once successfully purified, the secondary structure of the protein was investigated by circular dichroism (CD) and the stabilizing effect of bound $NAD^+$ and $NADP^+$ cofactors was determined by differential scanning calorimetry (DSC) and CD. The activity of the purified enzyme was initially measured by a colorimetric methimazole assay and subsequently by in vitro oxidation of known substrates of hFMO1 including benzydamine, tamoxifen, dasatinib and vandetanib.

# 2.2. Materials and methods

## Reagents

Human FMO1 plasmid purification was carried out by GenElute™ HP Plasmid Maxiprep Kit and gene extraction by GenElute™ Gel Extraction Kit purchased from Sigma Aldrich (Italy). *E. coli* JM109 was from Promega Corporation (Italy). Restriction enzymes HindIII and XbaI, buffer Tango (10X), SYBR Safe DNA Gel Stain and 6x Mass Loading Dye were purchased from Thermo Scientific™ (Italy). T4 ligase enzyme and 10×T4 DNA Ligase Buffer were from New England Biolabs (UK). Chromatographic resins were purchased from GE Healthcare (Italy). Chemicals including tryptone, yeast extract, glycerol, agar, ampicillin, isopropyl-beta-D-thiogalactopyranoside (IPTG), phenylmethanesulfonylfluoride (PMSF), riboflavin, flavin adenine dinucleotide (FAD), β-mercaptoethanol, glycerol, lysozyme, IGEPAL, NADPH, $NADP^+$, NADH, $NAD^+$, NaCl, KCl, $MgCl_2 \times 6H_2O$, $MgSO_4 \times 7H_2O$, $MnCl_2 \times 4H_2O$, $CaCl_2 \times 2H_2O$, $KH_2PO_4$, $K_2HPO_4$, RbCl, NaOH, MOPS, Tris-base, EDTA, potassium acetate, acetic acid, glucose, acetate, glycine, histidine, Tris-HCl, SDS, bromophenol blue, Coomassie Brilliant Blue buffer, glacial acetic acid, methanol, 5,5'-dithio-bis-[2-nitrobenzoic acid] (DTNB), dithiothreitol (DTT), methimazole, acetonitrile, formic acid, benzydamine, benzydamine N-oxide were all purchased from Sigma-Aldrich, tamoxifen and tamoxifen N-oxide from Toronto Research Chemicals (Canada); dasatinib and dasatinib N-oxide were purchased from BIOZOL Diagnostica Vertrieb GmbH (Germany) and vandetanib and vandetanib N-oxide from BioVision Incorporated (USA). All used chemicals were purchased HPLC grade and were used without any purification. All media, solutions and buffers were prepared with deionized Milli-Q water.

## Bacteria growth media preparation

*Super Optimal broth with Catabolite repression (SOC medium)* was prepared by dissolving 2 g of tryptone, 0.5 g of yeast extract, 1mL of 1 M NaCl and 0.25 mL of 1 M KCl in 98 mL of distilled water. The solution was autoclaved and cooled down to room temperature, after that under the sterile atmosphere the 1 mL of the filter-sterilized $Mg^{2+}$ stock (1 M $MgCl_2 \times 6H_2O$, 1M $MgSO_4 \times 7H_2O$) and 1 mL of 2 M filter-sterilized glucose was added (final concentration for both was 20 mM in the total medium). The complete medium was filtered through a 0.2 μm filter. The final pH was 7.0.

*Luria-Bertani (LB) liquid medium* was prepared by dissolving 10 g of tryptone, 5 g of yeast extract and 5 g of NaCl in 1 L of distilled water. Then the pH was adjusted to 7.5 with NaOH, the medium was autoclaved at 120 °C for 20 minutes. For preparing the LB agar for plates 15 g of agar was included before autoclaving.

*Terrific Broth (TB) liquid medium* was prepared by mixing 12 g of tryptone, 24 g of yeast extract and 5 mL of glycerol in 900 mL of distilled water. Separately the mixture of the salts for the buffering was made by dissolving 2.3 g of $KH_2PO_4$ (0.17 M final concentration) and 12.54 g of $K_2HPO_4$ (0.72 M final concentration) in water to reach 100 mL total volume. Both obtained solutions were autoclaved at 120 °C for 20 minutes. Salt was added to the medium before using it under a sterile atmosphere.

## *E. coli* JM109 competent cells preparation

*E. coli* JM109 was streaked onto an LB plate and incubated overnight at 37 °C. A single colony was picked and grown overnight in 3 mL of the sterile LB at 37 °C with shaking at 200 rpm. The 10 mL of LB was preheated for 30 min at 37 °C then the 200 µL of inoculum was added and bacteria were grown under agitation at 200 rpm at 37 °C until $OD_{600}$ reached 0.4 – 0.5. The 2 mL of the cell culture was diluted in 100 mL of preheated LB and continued growing at 37 °C and 180 rpm until the $OD_{600}$ was about 0.5 again. Obtained cells were transferred in two precooled sterile 50 mL falcon tubes and incubated on ice for 15 min. After that, the cells were centrifuged for 12 min at 2400 rpm at 4 °C. The supernatant was discarded and each pellet was resuspended in 16.5 mL of the ice-cold rubidium buffer (100 mM RbCl, 50 mM $MnCl_2 \times 4H_2O$, 30 mM potassium acetate, 10 mM, 15% glycerol v/v, pH 5.8 adjusted with 0.2 M acetic acid, filter-sterilized by 0.2 µm filter). Cells were incubated for 15 min on ice and centrifuged for 12 min at 2400 rpm at 4 °C. The supernatant was discarded again in the cold room and each pellet was resuspended with 4 mL of the second rubidium buffer (10 mM RbCl, 10 mM MOPS, 75 mM $CaCl_2 \times 2H_2O$, 15% v/v glycerol, pH 6.8 adjusted with 0.25 M NaOH, filter-sterilized by 0.2 µm filter). After 15 min incubation on ice, the competent cells were aliquoted and frozen in the liquid nitrogen and stored at -80 °C until use.

## *E. coli* JM109 transformation

One 100 µL aliquot of the competent cells was removed from -80 °C and placed on ice for 5 – 10 min until thawed. The aliquot was slightly mixed with a cold pipet tip and divided into two 50 µL portions. 25 – 50 ng of plasmid DNA were added to

the first portion of the competent cells and mixed gently with the pipet tip. The second part of the cells was used as negative control. Cells were immediately placed on ice and incubated for 30 min. The transformation reaction was heat-shocked for 90 seconds in the water bath at 42 °C and immediately transfered to ice for 2 min. After incubation, the 450 µL of room-temperature SOC medium was added to each reaction and incubated for 1 hour at 37 °C with shaking at 225 rpm. The cells were centrifuged for 2 min at 4000 rpm and the pellet was resuspended in the 100 µl of left-over supernatant. The transformed and control cells were plated on separate LB plates supplemented with 100 µg/mL ampicillin and incubated overnight at 37 °C approximately for 16 hours.

## Plasmid isolation and purification

Plasmid extraction and purification was carried out following the standard protocol of the GenElute™ Plasmid Miniprep Kit provided by Sigma-Aldrich. Briefly: *E. coli* cells containing target plasmid were distributed in the microcentrifuge tubes and pelleted at ≥3500 rpm for 5 minutes. The supernatant was discarded, and the pellet was resuspended in 200 µL of the Resuspension Solution. After adding 200 µL of the Lysis Solution to the resuspended cells total mixture was gently mixed by 6 – 8 inversions. After 2 -3 min the 350 µL of the Neutralization/Binding Solution was added to precipitate the *E. coli* residuals. The tubes were gently inverted 4 – 6 times and after that debris was pelleted by centrifuging at ≥12,000 × *g* for 10 minutes. GenElute Miniprep Binding Column was assembled and prepared by washing with 500 µL of the Column Preparation Solution by centrifugation at ≥12,000 × *g* for 1 minute after that all flow-through liquid was discarded. The transparent lysate fraction was transferred to the column and centrifuged at ≥12,000 × *g* for 1 minute, flow-through was discarded. In the next step, the column was washed with 750 µL Wash Solution and centrifugation at ≥12,000 × *g* for 1 minute. The flow-through liquid was discarded and the column was centrifuged again without the addition of any solution for 3 min. The column was transferred to the new collection tube and 50 µL of the preheated water was added. The target plasmid was eluted after centrifugation at ≥12,000 × *g* for 1 minute. The flow-through liquid contained target DNA and was collected and stored at –20 °C until use.

## Plasmid double digestion

The circular plasmid containing the hFMO1 gene was digested into two fragments, vector and gene, by restriction enzymes Xbal and HindIII using

corresponding restriction sites with further separation and visualization on the agarose gel. The reaction mixture contained 1 unit of each restriction enzyme for 1µg of the DNA, Milli Q water and the required amount of the 10X Tango buffer to reach the total single reaction volume of 20 µL.

## Agarose gel electrophoresis

Separation and visualization of the digested fragments were performed in 1% agarose gel. The gel was prepared by melting 1% agarose powder in 1X TAE buffer (40 mM Tris, 20 mM acetate and 1 mM EDTA, pH 8.6). SYBR Safe DNA Gel Stain (fluorescence dye) was added to the gel during the preparation steps to intercalate it in the agarose matrix and then, during the run, bind to the DNA and help to visualize under UV light. 6x Mass Loading Dye was mixed in the proportion with the double digestion reaction mixture and the sample was run for 1 h at 120 V at room temperature. The results were observed under UV of the Bio-Rad transilluminator device.

## DNA extraction from the agarose gel

The extraction and purification of the DNA from agarose gel were done by following the standard protocol of the GenElute™ Gel Extraction Kit provided by Sigma-Aldrich. Briefly: The slice of the agarose gel containing the target DNA fragment was isolated by excising with the scalpel and after that, the piece was weighed. Obtained gel was dissolved in the 3 gel volumes of the Gel Solubilization Solution by incubation at 50 – 60 °C for 10 minutes with the interval vortexing until complete solubilization. The binding column was assembled and washed with the Column Preparation Solution by centrifugation at ≥12,000 × *g* for 1 minute. To the yellow mixture 1 gel volume of 100% isopropanol was added and mixed until homogenous. The gel mixture was transferred into the binding column and centrifuged at ≥12,000 × *g* for 1 minute. After DNA binding the column was washed with 700 µL of Wash Solution by centrifugation at ≥12,000 × *g* for 1 minute, one extra step of the centrifugation without the addition of any solution was performed. Finally, the binding column was transferred to a fresh collection tube and DNA was eluted with 50 µL of the hot water after centrifugation at ≥12,000 × *g* for 1 minute. The flow-through liquid contained target DNA was collected and stored at –20 °C until use.

## Ligation of the hFMO1 gene into pJL2 vector

The isolated hFMO1 gene was ligated into the pJL2 vector using Xbal and HindIII restriction sites. The ratio between the insert and vector for the ligation reaction was decided based on the size and concentration of each. The optimal condition was found to be one unit of the vector with five units of the insert. The reaction mixture contained one unit of the T4 ligase enzyme (M2200S), one unit of the 10×T4 DNA Ligase Buffer, 1 unit of the pJL2 vector and 5 units of the hFMO1 insert and 2 units of the Milli Q water and incubated overnight at 4 °C. Obtained DNA was used for the bacterial transformation.

## FMO1 Expression in *E. coli*

Human FMO1 was expressed in *E. coli* JM109 cells in two-liter glass conical flasks containing 500 mL of Terrific Broth (TB). Inoculum of 5 mL, overnight growing cell culture in Luria-Bertani (LB) liquid medium with ampicillin (100 μg/mL), was diluted in TB media with the addition of 100 μg/mL ampicillin solution. Cells were grown until $OD_{600}$ reached 0.5 - 0.6 at 37 °C and 200 rpm. Protein expression was induced by the addition of IPTG (final concentration 1 mM) and the process was continued at 24 °C and 180 rpm. After 1 hour 50 mg/L of riboflavin was added. 24 hours post-induction cells were harvested by 20 min centrifugation at 4000 rpm at 4 °C, cell pellet was stored at -20 °C until use.

## FMO1 Purification

Protein was purified from the membrane fractions via DEAE anion exchange and Ni-chelating Sepharose fast-flow affinity column, following the procedure described by Catucci and co-workers [30]. Briefly: the pellet containing hFMO1 was resuspended in Buffer A (50 mM KPi pH 8.0, 20% glycerol, 5 mM β-mercaptoethanol) with 0.5 mM PMSF using 5 mL/g of cells. Then 0.5 mg/mL of lysozyme was added and stirred for 1 hour at 4 °C. The ultrasonication procedure was carried out on ice for 10 x 30 seconds with 1-minute intervals to prevent overheating. The lysate was ultracentrifuged at 41000 rpm for 60 min at 4 °C to isolate the membrane fraction. Then the pellet was resuspended using a Dounce homogenizer in Buffer A with 1% IGEPAL as detergent after that the membrane fraction was solubilized by stirring for 2 hours at 4 °C. The second step of ultracentrifugation was applied to the final suspension also at 41000 rpm for 60 min at 4 °C. The supernatant was loaded into preequilibrated, by Buffer B (Buffer A with 0.1% of IGEPAL), DEAE-Sepharose Fast Flow column (150 mL) at flow rate

of 0.5 mL/min. Human FMO1 protein was eluted from the DEAE column to the Nickel-chelating Sepharose Fast Flow column (25 mL) by Buffer B with 2 mM of KCl. After that, as His-tagged protein was bound to the Ni column, the washing procedure was started by following the next steps: 2 column volumes of Buffer C (Buffer B with 50 mM of KCl and 100 µM of FAD), 2 volumes of Buffer C with 50 mM of glycine, 2 volumes of Buffer C with 1 mM of histidine, 2 volumes of Buffer C with 5 mM of histidine. Protein was eluted and collected in 1 mL fractions by Buffer C with 40 mM of histidine. The elution profile was monitored by UV/Vis spectroscopy. Protein- containing fractions were concentrated using a 30 kDa cutoff Amicon™ Ultra Centrifugal Filter. The elution buffer was exchanged for storage buffer (100 mM KPi pH 8.0, 20% of glycerol, 1 mM EDTA), and protein was stored at -80 °C in small aliquots to prevent repeated thawing/freezing.

## Sodium dodecyl sulfate-polyacrylamide gel electrophoresis (SDS-PAGE)

The separation and visualization of the protein was carried out using 12.5% separation gel with 4% stacking gel, recommended for proteins with molecular weight in the range of 10 – 70 kDa, following the standard Bio-Rad's procedure for the gel preparation. The lysate of the cells, elution fractions and protein samples were prepared in 2x Laemmli Loading Buffer (62.5 mM Tris-HCl (pH 6.8), 2% SDS, 25% glycerol, 5% ß-mercaptoethanol, 0.01% bromophenol blue) in the proportion 1 volume of the analyte: 2 volumes of the buffer. The electrophoretic separation was carried out at 70 V until the frontline of the samples crossed boarded line between stacking and separation gels, then the voltage was increased to 120 V and the process was continued for 70 min for an optimal separation. After the separation, the gel was stained for 30 min in Coomassie Brilliant Blue buffer, and after rinsing with the water the gel was destained for another 30 min in the Destaining Buffer (10% glacial acetic acid, 40% methanol, 50% Milli Q water). After double washing with the water, the gel was analyzed.

## UV/Vis characterization

The UV/Vis spectra of the pure enzyme and its reduction/reoxidation state and pH preference were monitored by Agilent HP-8453E spectrophotometer under anaerobic conditions. All spectra were recorded at 15 °C. The enzyme stability and pH preference were measured in the 50 mM potassium phosphate buffer at pH range 5.5, 6.0, 6.5, 7.0, 7.4, 8.0 and time range from 0 to 30 min with the 5 min interval for each sample. Enzyme-bound FAD cofactor was monitored by the two

characteristic peaks at 375 and 450 nm in the presence of 0.1 M potassium phosphate buffer pH 7.4. The concentration and obtained yield of hFMO1 were estimated by Beer-Lambert law using the FAD molecular extinction coefficient of 11300 $M^{-1}cm^{-1}$ at 450 nm. To reduce the cofactor and stabilize the hydroperoxyflavin (FAD-OOH) intermediate the equimolar amount of aerated NADPH was used. Intermediate formation and decay were followed at 368 nm and reoxidation of FAD at 450 nm.

## Circular Dichroism

The CD spectra of hFMO1 were obtained by a J-815 CD spectrometer (JASCO International Co., Tokyo, Japan). The scan was performed in 0.1 M phosphate buffer pH 7.4 with protein concentration 3.5 μM at 25 °C. The spectral range was from 190 nm to 260 nm with a scan rate of 100 nm/min applied 1 nm data pitch using 1 nm bandwidth in a 0.1 cm path length cell. The protein secondary structure was estimated by fitting the experimental data by the Beta Structure Selection (BeStSel) method [120].

## Differential scanning calorimetry experiments

Investigation of the stabilization effect that occurred by binding the ligand to the enzyme was characterized by DSC using a Microcal VP-Capillary DSC, Malvern Instruments Ltd. Worcestershire, UK. All scans were performed at a scan rate of 90 °C/h in the temperature range from 27 to 90 °C in 0.1 M phosphate buffer pH 7.4 with a protein concentration of 10 μM in the absence and presence of ligand (0.5 mM of $NADP^+$ or $NAD^+$). Before the experiment, the working cell was pre-equilibrated with 10 cycles of working buffer and after that equilibrated for 10 min at 25 °C. According to the procedure, the scan of the work sample was followed by the control rescan to check the absence of refolding process and to use this control sample for background correction during the data proceed [121]. Protein melting temperature and all required deconvolution steps were performed by fitting the data with the Levenberg-Marquardt non-linear least-square method using Origin software of the MicroCal package.

## Activity assays

The monooxygenation activity of the purified hFMO1 was followed by the S-oxygenation of methimazole in the presence of NADPH or NADH as a reducing

agent, hypotaurine S-oxidation to taurine and N-oxidation of benzydamine, tamoxifen, dasatinib and vandetanib.

*Methimazole colorimetric assay*

Methimazole oxidation to its S-oxide mediated by FMO1 was monitored in the kinetic mode by Agilent HP-8453E spectrophotometer at 412 nm. The reaction mixture contained: 0.5 µM of the pure enzyme, 0.1 mM of NADPH or NADH, 60 µM of 5,5'-dithio-bis-[2-nitrobenzoic acid] (DTNB), 20 µM of dithiothreitol (DTT), 1 mM of methimazole and 0.1 M potassium phosphate buffer pH 7.4 up to 1 mL of total volume. Before starting, the required volume of the buffer was preheated in the cuvette to 37 °C then DTNB, DTT, FMO1 and NADPH/NADH were added and mixed. The cuvette was placed inside the spectrophotometer and the substrate-independent rate was recorded for 30 – 60 sec. When the stable baseline was reached the methimazole was added to the sample, and mixed gently and after a few seconds of the equilibration, the reaction rate was recorded following the disappearance of the yellow colour at 412 nm.

*Hypotaurine oxidation*

The confirmation of taurine production by hFMO1 from hypotaurine was performed in collaboration with Ion Source & Biotechnologies Srl (Milan, Italy). Analysis was carried out employing an LC-SACI-MS (LC - SANIST Ultimate 3000, Dionex; MS – SANIST platform, ISB) working in positive ion mode.

**Sample preparations:** 1 mL of reaction mixture contained: 0.1 M potassium phosphate buffer pH 7.4, 0.5 µM purified enzyme, 0.5 mM NADPH and substrate concentration 250 and 500 µM. The reaction was initiated by adding NADPH and incubated at 37 °C and after 4 or 24 hours immediately terminated by adding 500 µL of ice-cold acetonitrile. The mixture was centrifuged at 12000 × *g* for 5 min and the supernatant was used for analysis. Before the analysis, each sample was diluted 1:10 in double distilled $H_2O$.

**Preparations of standards for LC-SACI-MS analysis:** the standards of taurine (5.3 mg) and hypotaurine (1.9 mg) were both solubilized in 1 mL of double distilled $H_2O$, obtaining a concentration of 5.3 mg/mL and 1.9 mg/mL, respectively. Both were diluted 1:100 in double distilled $H_2O$ to a final concentrations of 53 µg/mL and 19 µg/mL, respectively.

**LC-APCI-MS setup:** Analysis was performed using an Ultimate 3000 HPLC (Thermofisher, USA). The column used was a Phenomenex Kinetex F5 50 x 4.6 µ. The analyses were performed using a biphasic gradient: Phase A ($H_2O$ + 0.1% formic acid) and Phase B ($CH_3OH$ + 0.1% formic acid) at a flow rate of 0.25 mL/min. The volume of the sample injected was 5 µL. The chromatographic gradient used: 0-5 min 2% of Phase B, 5-6 min 80% of Phase B, 6-14 min 80% of Phase B, 14-14.1 min 2% of Phase B, 14.1-21 min 2% of Phase B.

*Benzydamine N-oxidation*

The reaction mixture for benzydamine conversion mediated by hFMO1 contained: 0.5 µM enzyme, 0.5 mM NADPH, and 0.5 mM benzydamine in 0.1 M potassium phosphate buffer pH 7.4 up to 200 µl of total volume. The reaction was initiated by adding the NADPH to the reaction mixture and incubating for 15 min at 37 °C. The reaction was terminated by adding 100 µl of ice-cold acetonitrile to the reaction mixture . The reaction mixture was subsequently centrifuged at 12000 × *g* for 5 min and the supernatant was used for HPLC analysis of metabolite formation.

The separation and quantitation of the reaction mixture were performed by using the preliminary calibration of the system by commercially available analytical standards of benzydamine and its N-oxide. Analysis was performed with an Agilent 1200 quaternary pump HPLC System equipped with a diode array UV detector (Agilent Technologies, USA) with Kinetex 5µm EVO C18 100 Å LC column 150×4.6 mm. The substrate and its metabolite were separated by isocratic elution and were detected at a wavelength of 308 nm. The mobile phase consisted of 22% of acetonitrile and 78% of 0.1% formic acid, the analysis time was 18 min, and the flow rate was 0.5 mL/min. The retention time of benzydamine and benzydamine N-oxide were found to be 8.8 min and 12 min, respectively.

*Tamoxifen oxidation*

The reaction mixture for tamoxifen conversion mediated by hFMO1 contained: 0.5 µM pure enzyme, 0.5 mM NADPH, and a range of substrate concentration from 0 to 250 µM in 0.1 M potassium phosphate buffer pH 7.4 up to a total volume of 200 µl . The reaction was initiated by adding the NADPH to the reaction mixture and incubating for 30 min at 37 °C. The reaction was terminated by adding 100 µl of ice-cold acetonitrile. Subsequently the mixture was centrifuged at 12000 × *g* for 5 min and the supernatant was used for further HPLC analysis of metabolite formation.

The separation and quantitation of the reaction mixture were performed by using the preliminary calibration of the system by analytical standards of tamoxifen and its N-oxide. Analysis was performed with an Agilent 1200 quaternary pump HPLC System equipped with a diode array UV detector (Agilent Technologies, USA) with Kinetex 5µm EVO C18 100 Å LC column 250×4.6 mm. Tamoxifen and its N-oxide metabolite were separated by isocratic elution and were detected at a wavelength of 276 nm. The mobile phase consisted of 82% of methanol and 18% of 1% triethylamine, analysis time was 20 min with a flow rate of 1.1 mL/min [16]. The retention time of tamoxifen and its N-oxide product were 6.5 min and 3.5 min, respectively.

*Dasatinib oxidation*

The reaction mixture for dasatinib conversion mediated by hFMO1 contained: 0.5 µM of the pure enzyme, 0.5 mM of NADPH, and a range of substrate concentration from 0 to 250 µM in 0.1 M potassium phosphate buffer pH 7.4 in a total volume of 200 µL. The reaction was initiated by adding the NADPH to the reaction mixture and incubating 30 min at 37 °C and immediately terminated by adding 100 µl of ice-cold acetonitrile . The mixture was centrifuged at 12000 × *g* for 5 min and the supernatant was used for HPLC analysis of metabolite(s) formed.

The separation and quantitation of the reaction mixture were performed by using the preliminary calibration of the system by analytical standards of dasatinib and its N-oxide. Analysis was performed with an Agilent 1200 quaternary pump HPLC System equipped with a diode array UV detector (Agilent Technologies, USA) with Kinetex 5µm EVO C18 100 Å LC column 250×4.6 mm. Tamoxifen and its metabolite were separated by isocratic elution and were detected at a wavelength of 320 nm. The mobile phase consisted of 22% of acetonitrile and 78% of 0.1% formic acid, analysis time was 15 min with a flow rate of 1 mL/min. The retention time of dasatinib and its N-oxide product were 4.1 min and 5.4 min, respectively.

*Vandetanib oxidation*

The reaction mixture for vandetanib conversion by hFMO1 contained: 0.5 µM enzyme, 0.5 mM NADPH, and a range of substrate concentration from 0 to 250 µM in 0.1 M potassium phosphate buffer pH 7.4 in a total volume of 200 µL . The reaction was initiated by adding the NADPH to the reaction mixture and incubated for 30 min at 37 °C. The reaction was terminated by adding 100 µL of ice-cold acetonitrile. The mixture was centrifuged at 12000 × *g* for 5 min and the supernatant was used for HPLC analysis of metabolite formation.

The separation and quantitation of the reaction mixture were performed by using the preliminary calibration of the system by analytical standards of vandetanib and its N-oxide. Analysis was performed with an Agilent 1200 quaternary pump HPLC System equipped with a diode array UV detector (Agilent Technologies, USA) with Kinetex 5µm EVO C18 100 Å LC column 250×4.6 mm. Vandetanib and its metabolite were separated by gradient elution and were detected at a wavelength of 340 nm. The mobile phase consisted of Phase A: methanol and Phase B: 0.5% triethylamine pH 3, analysis time was 25 min with a flow rate of 1 mL/min. Gradient profile was: 0-2 min 70% Phase B, 2-5 min 35% Phase B, 5-15 min 20% Phase B, 15-20 min 20% Phase B, 20-21 min 70% Phase B, 21-25 min 70% Phase B. Retention time of vandetanib and its N-oxide product were 13 min and 9 min, respectively.

## 2.3. Cloning, expression and purification

Oligonucleotides encoding the amino- and carboxy-termini of wild type hFMO1 were synthesized by GenScript company. Initially, the hFMO1 gene was digested from the commercial pUC57 plasmid using the XbaI – HindIII restriction sites with the further separation of the linearized DNA fragments in the 1% agarose gel. The hFMO1 gene was extracted from the gel and successfully ligated into the pJL2 expression vector as shown in Figure 6B [118]. The presence of the hFMO1 gene in the pJL2 vector was confirmed by the double digestion reaction and results are shown in Figure 6A lane 5, as a result, two bands were detected: the first linear fragment 2554 bp corresponds to the pJL2 vector without any insert, and the second one - 1623 bp to hFMO1 [with a polyhistidine tag, a stretch of four histidine residues (5’ CACCATCACCAT 3’) was inserted at the C-terminus to assist in the purification] [30]. The control samples of the undigested circular plasmid are shown in Figure 6A lane 2 and two single digestion reactions in lanes 3, 4 were also visualized in the gel.

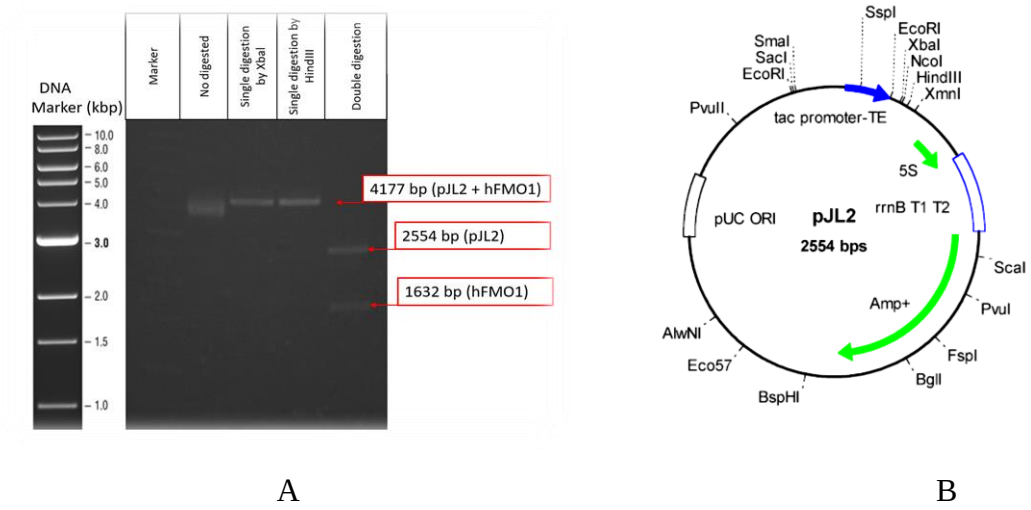


A B

**Figure 6: (A)** Agarose gel of the double digestion of -pJL2-hFMO1 where from the left;1st lane - HyperLadder marker; 2nd lane –undigested plasmid; 3rd lane – single digestion with XbaI; 4th lane – single digestion by HindIII; 5th lane – double digestion reaction **(B)** The full map of the pJL2 plasmid where the gene that encodes hFMO1 was inserted between HindIII and XbaI.

To confirm the presence of the FMO1 gene inside the designed expression vector, four plasmid samples obtained from the different transformations were sequenced by Eurofins Genomics. Four sequencing primers, three forward and one reverse, were designed as mentioned earlier and are shown in Table 4. The results of the DNA sequencing were analyzed by NCBI Basic Local Alignment Search Tool and as expected 99 – 100% identity with Homo sapiens FMO1 was found.

**Table 4:** Designed primers for the hFMO1-pJL2 plasmid sequencing

| **Primer** | **N of sample** | **5'-Sequence-3'** |
|---|---|---|
| Forward Sequencing Primer-1 (350-800): | ASM0041881 | ATGCTCAGATTCTGCTGTCT |
| Forward Sequencing Primer-2 (801-1200): | ASM0041882 | TCATGCAAATTACGGCTTAA |
| Forward Sequencing Primer-3 (1201-1623): | ASM0041883 | CCTGGCCATTATTGGCCTCA |
| Reverse Sequencing Primer (400-1): | ASM0041884 | CATGCATAGTGACCACCTCC |

The obtained plasmid was successfully used for the transformation of the *E. coli* JM109 competent cells and the full-length hFMO1 enzyme was heterologously expressed. After cell harvesting, little traces of a blue insoluble compound were detected at the top of the pellet. This unexpected observation is due to hFMO1 conversion of indole, produced by *E. coli* from tryptophan to indoxyl which after dimerization forms indigo (see Chapter 5). To obtain a high levels of holoprotein riboflavin as the precursor of the FAD cofactor must be used.

The purification process is based on two sequential chromatographic steps, mentioned in the method section. As defined by the "ExPASy Compute pl/Mw tool" the theoretical isoelectric point of the hFMO1 is 6.92, including the His-tag, which means that at pH 7.4 or 8.0 the protein has a slightly negative charge. The flow-through sample after the DEAE Sepharose column was showed the presence of the characteristic protein-bound FAD with the absorbance maxima at 375 and 450 nm. The enzyme-containing fractions were loaded onto the Ni-chelating affinity column where the FMO1 protein was bound through its His-tag to the Ni column. The elution profile from the Ni columns shown in Figure 7A, recorded using an HP-8453E spectrophotometer.

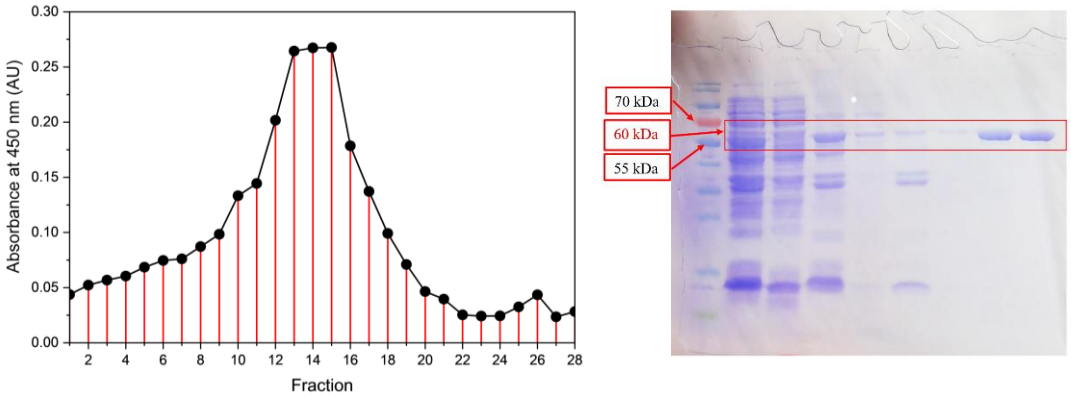


A B

**Figure 7: (A)** Elution profile of hFMO1 from the Ni-chelating column. **(B)** SDS-PAGE of the hFMO1 purification steps: from left; Lane 1 Thermo Scientific PageRuler Prestained Protein Ladder 10 - 80 kDa; Lane 2 crude cell extract after lysis and ultrasonication; Lane 3 supernatant after the first ultracentrifugation (cytosolic fraction); Lane 4 pellet after the first ultracentrifugation (membrane fraction); Lane 5 supernatant after the second ultracentrifugation; Lane 6 pellet after the second ultracentrifugation; Lane 7 fraction after DEAE column; Lane 8 fraction Ni-affinity column; Lane 9 fraction after 30 kDa cut-off Amicon membrane.

Samples from the different stages of the hFMO1 purification were run on SDS-PAGE following the standard procedure described in the methods section. The progress in the enzyme purification can be seen following the band at 60 kDa. Overexpression of the target protein in the cell lysate is shown in lane 2. After the first cycle of ultracentrifugation, FMO1 is still bound to the membrane, lane 4. After membrane solubilization, in the presence of IGEPAL and the second cycle of ultracentrifugation, hFMO1 was detected in the soluble fraction. Lanes 7 – 9 show samples after DEAE and Ni chromatography followed by protein concentration with the 30 kDa cut-off Amicon membrane.

## 2.4. Spectroscopic characterization

The physiological pH within the human kidney where FMO1 is mainly expressed is in the range of 7.0 – 7.3, and before carrying out any experiments with the purified enzyme it was important to determine the optimal buffer pH where the stability of the enzyme was maximal. As described in the methods section, the UV/Vis spectra of enzyme-bound FAD were recorded in the phosphate buffer with various pH values, from 5.5 to 8.0. The normalized spectra of the time-dependent measurements are shown in Figure 8. It can be seen that at pH 5.5 and 6.0 the enzyme is not stable and the lowest pH value which could be used was 7.0. The spectra at 7.4 and 8.0 demonstrated the highest stability of FMO1. However, all subsequent experiments were carried out at pH 7.4 closest to the physiological pH.

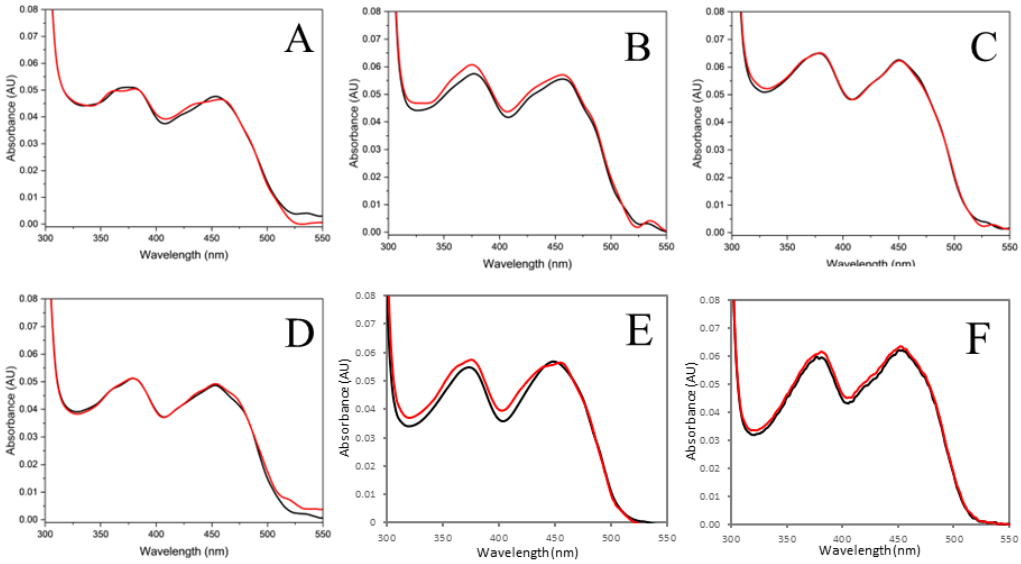


**Figure 8:** Effect of pH on the absorption spectra of hFMO1. Spectra collected after 1 min (black) and 30 min (red), pH range 5.5 – **(A)**, 6.0 – **(B)**, 6.5 – **(C)**, 7.0 – **(D)**, 7.4 – **(E)**, 8.0 – **(F)**.

The UV/Vis spectrum of the purified hFMO1 is shown in Figure 9. As can be seen in Figure 9A, the characteristic peaks of the enzyme-bound FAD cofactor are observed at 375 and 450 nm. The concentration and yield of the purified protein were calculated considering a 1:1 molar content of FAD. The final protein purification yield was 5 mg/L of culture.

The possibility of the enzyme receiving reducing equivalents from NADPH could be used as a preliminary characterization of the purified hFMO1 activity. The purified enzyme was reduced by equimolar concentration of NADPH, Figure 9B.

The disappearance of the characteristic 450 nm peak was detected together with the simultaneous formation of the hydroperoxyflavin intermediate followed at 368 nm. In the presence of molecular oxygen the cofactor was re-oxidized, with the absorbance increase at 450 nm.

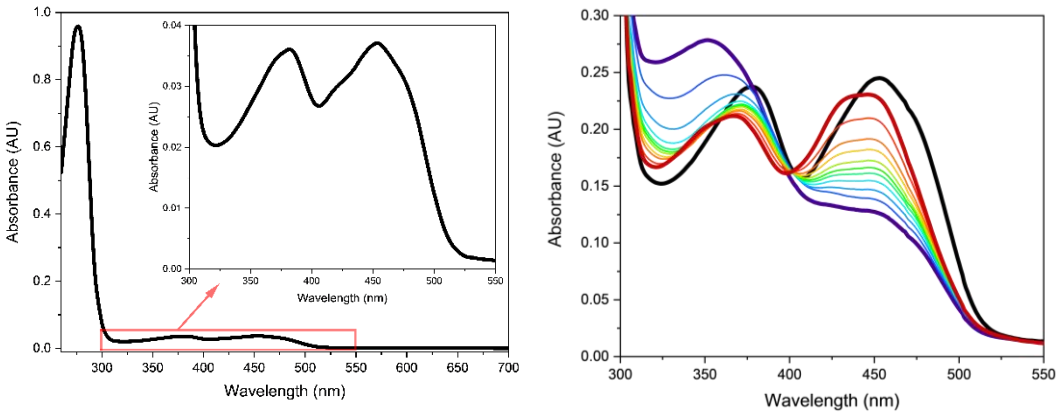


A B

**Figure 9: (A)** UV/Vis spectra of the purified hFMO1, inset typical absorption peaks of the enzyme-bound FAD in the oxidized state. **(B)** Spectra of the hFMO1 reduction by NADPH in aerobiosis: the black spectrum is the oxidized FAD, the violet spectrum is after reduction by NADPH, and blue to the red spectra are the re-oxidation of the FAD cofactor.

The observed formation and stabilization of the FAD-OOH intermediate under aerobic conditions and its slow re-oxidation process have not been observed in other hFMO enzymes [14,28]. For this reason, the reduction and re-oxidation of the purified hFMO1 were further studied by stopped-flow spectroscopy and will be discussed in the following chapter.

## 2.5. Circular dichroism

Secondary structure content of hFMO1 protein was determined using circular dichroism (CD) spectroscopy. No CD data or crystal structure have been published for this protein. The experimentally obtained CD spectrum was then used to predict the secondary structure content using the PDB2CD [122,123] webserver. This is a new in silico tool that makes the prediction on the basis of the protein atomic coordinates and comparison of the secondary structure of the analyzed protein with the already known and well-studied homologous proteins. As the initial input, the PDB file of the 3D model of hFMO1 (constructed by the Phyre2 server and with the FAD cofactor docked inside) was uploaded. In the subsequent step, the predicted CD spectrum was superimposed with the experimental one. Finally, the

superimposition resulted in the estimation of the secondary structure, and the content was calculated by curve fitting and analysis by the BeStSel [124,125] webserver.

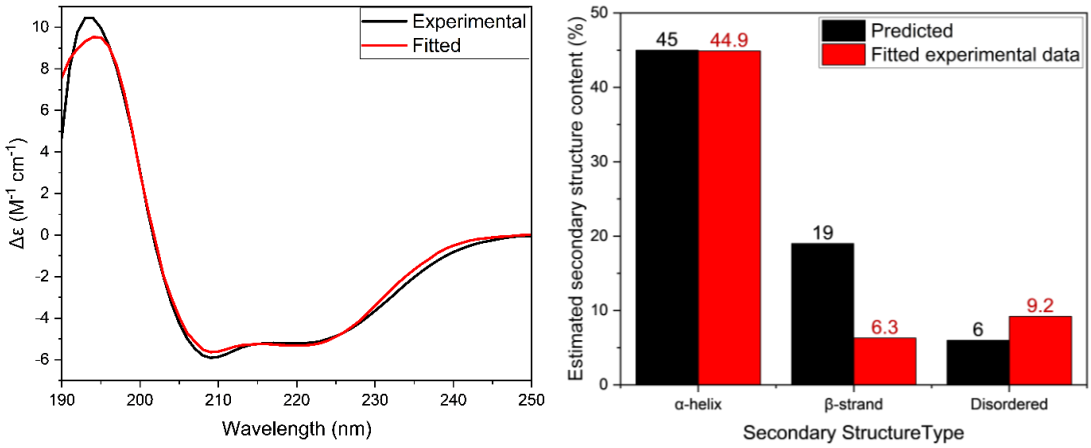


A B

**Figure 10**: **(A)** CD spectrum of the purified hFMO1 (black) and predicted by PDB2CS (red). **(B)** Estimated secondary structure content on the basis of the fitting of the CD spectrum to BeStSel webserver.

The method used by Beta Structure Selectin (BeStSel) can recognize the protein fold, essentially membrane ones, by analyzing the twist and orientation of the β-sheets. The advantage of this tool is that it is not only adequate for fold prediction but also distinguishing the CATH protein fold, i.e. to detect and predict the presence of certain fold motifs in the structure. The experimental spectrum of the purified hFMO1 at 25 °C shown in Figure 10 has minima at 208 and 222 nm, which overlap the predicted spectrum, Figure 10A. The estimated secondary structure content, Figure 10B, is also in line with published data for the hFMOs family [126].

Protein fold recognition and classification prediction for secondary structure composition were provided by the BeStSel webserver analyzing experimental CD spectra. The obtained result is based on the CATH classification [127] and identified the three (3.40.50) Rossmann folds typical for FMOs [24,128,129].

## 2.6. Differential scanning calorimetry

Recent findings on hFMO3 have highlighted the key role of $NADP^+$ in stabilizing the protein structure, measured as a significant shift of the melting temperature ($T_m$) from 45.1 ± 0.1 °C to the higher value of 49.1 ± 0.2 °C [126]. For

this reason, we followed the unfolding of hFMO1 in the absence and in the presence of $NADP^+$ or $NAD^+$ using differential scanning calorimetry (DSC) and the results are shown in Figure 11A. As can be seen in the figure, in the absence of either cofactor (black line) a $T_m$ of 40.8 ± 0.2 °C is measured. Addition of 0.5 mM $NADP^+$ causes a shift of the $T_m$ to 47.5 ± 0.1 °C (red line) with an unfolding process starting at higher temperatures (above 34 °C). On the other hand, when $NAD^+$ is added no significant change is detected in $T_m$ (green line) in comparison to the protein in the absence of cofactor.

As these data do not exclude a possible role of $NAD^+$ in FMO1 catalysis, the ability of the enzyme to use both NADH or NADPH as source of reducing unit was investigated. Since pH 7.4 represents a physiological benchmark and for hFMO1 it has been previously reported that both cofactors are equally effective for catalysis at this pH [33], all experiments were conducted at pH 7.4.

**Table 5:** The melting temperatures of the unfolding process for hFMO1 in the presence or absence of ligands

| **Protein** | **$T_{m1}$, °C** | **$T_{m2}$, °C** | **$T_{m3}$, °C** |
|---|---|---|---|
| hFMO1 | 38.46 ± 0.85 | 40.82 ± 0.15 | - |
| hFMO1/$NADP^+$ | 44.30 ± 0.52 | 50.08 ± 0.092 | 47.54 ±0.11 |
| hFMO1/$NAD^+$ | 37.61 ± 0.52 | 40.50 ± 0.095 | - |

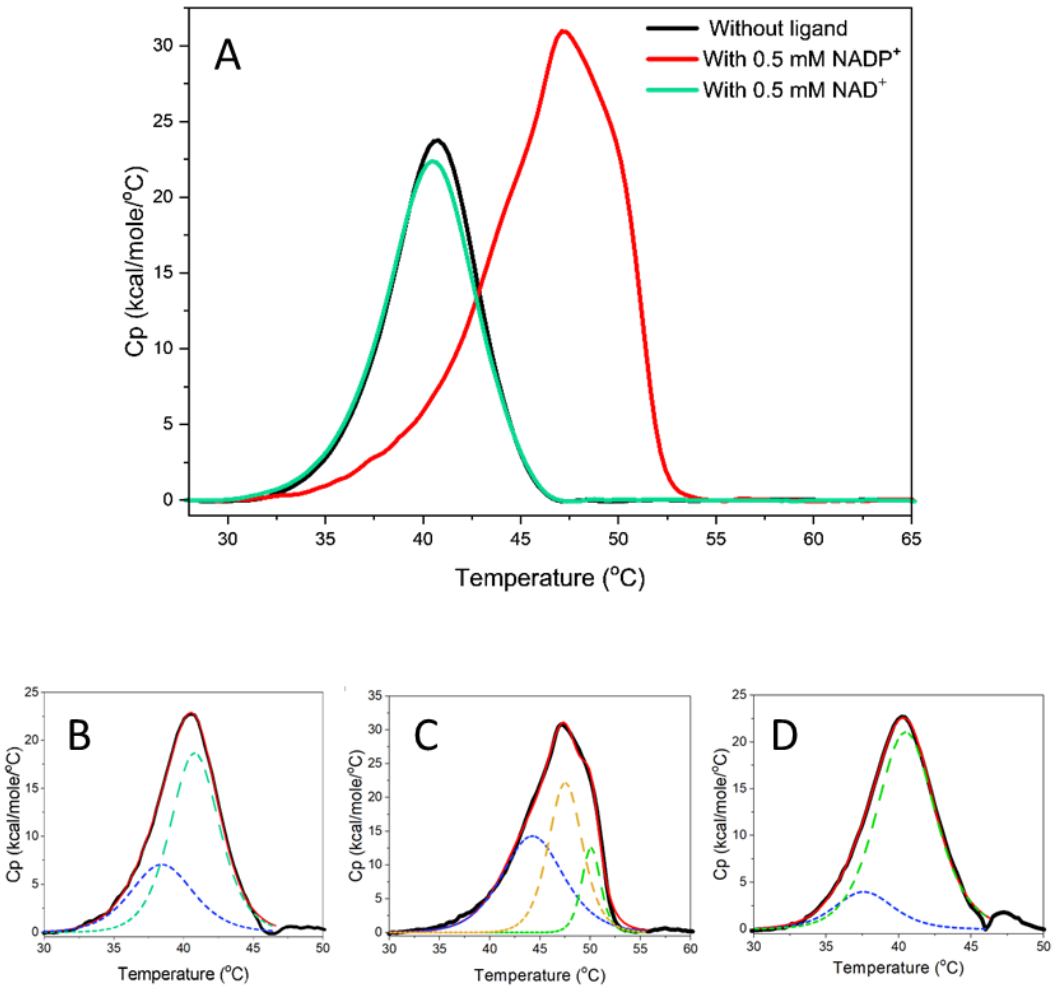


**Figure 11:** DSC data of hFMO1: **(A)** scan of protein without ligand is shown in black, in the presence of 0.5 mM $NADP^+$ in red and with 0.5 mM $NAD^+$ in green. Deconvoluted DSC thermograms: **(B)** hFMO1 without ligand; **(C)** hFMO1 with 0.5 mM - $NADP^+$; **(D)** hFMO1 with 0.5 mM - $NAD^+$. Experimental thermograms are shown in black, the derived peak 1, 2 and 3 are in blue, yellow and green respectively and their deconvolution is in red.

Experimental thermograms were deconvoluted to determine the number of states of the thermal unfolding process together with the melting temperatures in the absence or presence of the two ligands. The obtained data are summarized in Table 5. Two peaks were obtained for the enzyme as shown in Figure 11B and in the presence of the $NAD^+$, Figure 11C corresponds to the existence of two melting processes that related to the two domains (NADPH/NADH and FAD-binding domain). The second peak, higher temperature, derives from the transition from the native folded state to a disordered conformation resulting in total unfolding and aggregation. The third transition process, observed only in the presence of $NADP^+$

is more difficult to assign and due to occurring at a higher temperature might be attributed to a more stable state yet unidentified.

## 2.7. Activity assays

To prove the catalytic activity of the purified hFMO1 several know substrates of this enzyme were used: methimazole – an antithyroid agent that inhibits the actions of thyroid peroxidase [9,53,130], benzydamine – locally-acting nonsteroidal anti-inflammatory drug [38–40], hypotaurine – an endogenous neurotransmitter, organic osmolyte and cytoprotective agent, the precursor in the biosynthesis of taurine [13,33], tamoxifen – selective estrogen receptor modulator used for early- and advanced-stage breast cancer treatment [69,88], dasatinib – potent protein kinase inhibitor for the treatment of chronic myeloid leukemia [131–133] and vandetanib - an inhibitor of vascular endothelial growth factor receptor 2 (VEGFR-2) and epidermal growth factor receptor (EGFR) [73,74,134,135].

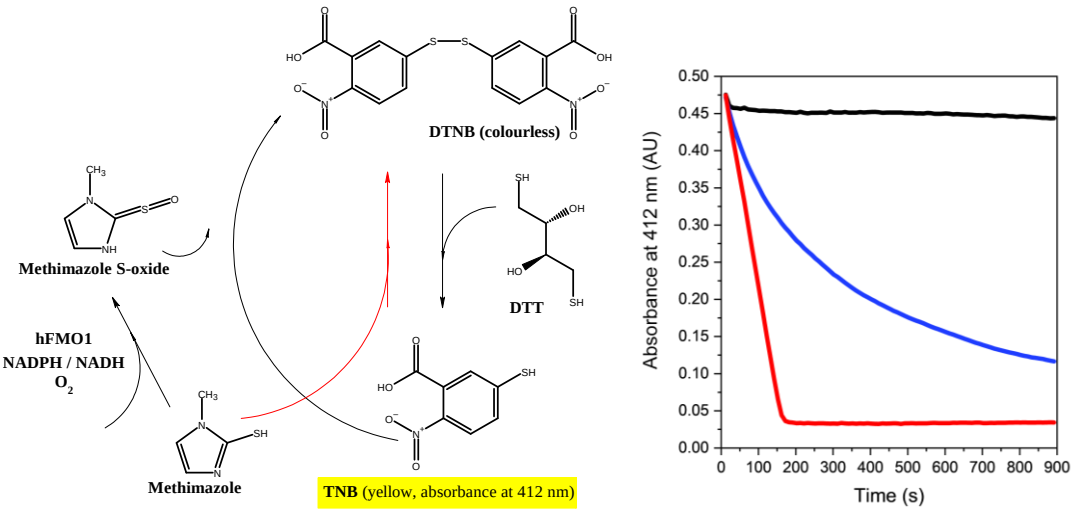


A B

**Figure 12: (A)** The scheme of methimazole oxidation mediated by hFMO1 as activity colorimetric assay. **(B)** Time course methimazile S-oxide production by FMO1 without cofactor (black line), in the presence of NADPH (red line) and NADH (blue line).

Oxidation of the methimazole to its S-oxide by hFMO1 was measured using Dixit and Roche assay [136]. The chemical reactions of the methimazole assay are illustrated in Figure 12A, briefly: in the first step, the 5,5-dithio-bis-(2-nitrobenzoic acid) (DTNB/Ellman's Reagent) was reduced by dithiothreitol (DTT) to the nitro-5-thiobenzoate (TNB) a yellow colored product that can be followed spectrophotometrically at 412 nm. Methimazole S-oxide, produced by FMO1 from

methimazole in the presence of NADPH, inhibits the reaction of TNB formation and enzyme activity could be estimated by following the rate of decrease in 412 nm absorption until the reaction mixture becomes colorless. The reaction was done as described in the Methods section and results are shown in Figure 12B. The results obtained demonstrate that the purified hFMO1 is active and can use both, NADPH and NADH, as reducing agents, but with NADPH having a higher affinity to the enzyme.

As a second known substrate, the enzymatic conversion of hypotaurine to taurine by hFMO1 was tested. This reaction has recently been identified and proposed as the possible natural role of FMO1 in the chain of biological processes in humans, Figure 13A [33]. In order to confirm that the purified hFMO1 is also capable of converting the hypotuaurin to taurin, enzymatic reactions were analysed by LC-MS. The reaction conditions are summarized in Table 6. The ion extraction chromatograms of the hypotaurine m/z 110 and the taurine m/z 126 are shown in Figure 13B and 13C, respectively. The fragmentation results obtained for both control experiments and the enzymatic reactions are reported in Table 6. As can be seen in the table, in all control samples no taurine was observed whereas all enzymatic reactions with hFMO1 showed the taurine fragmentation peak at m/z 126.10, as expected for the active enzyme.

**Table 6:** Mass spectra analysis of hypotaurine oxygenation

| Sample | Reaction time | Reaction conditions | Area hypotaurine | Area taurine |
|---|---|---|---|---|
| **S1 (control)** | 4 hours | hypotaurine - 250 µM<br>hFMO1 - 0.5 µM | 96439 | - |
| **S2** | | hypotaurine -250 µM<br>NADPH - 0.5 mM<br>hFMO1 - 0.5 µM | 47333 | 19954 |
| **S3 (control)** | 4 hours | hypotaurine - 500 µM<br>hFMO1 - 0.5 µM | 126744 | - |
| **S4** | | hypotaurine - 500 µM<br>NADPH - 0.5 mM<br>hFMO1 - 0.5 µM | 95195 | 24899 |
| **S5 (control)** | 24 hours | hypotaurine - 500 µM<br>hFMO1 - 0.5 µM | 145962 | - |
| **S6** | | hypotaurine - 500 µM<br>NADPH - 0.5 mM<br>hFMO1 - 0.5 µM | 62771 | 36376 |
| **Std 1** | - | - | 253073 | - |
| **Std2** | - | - | - | 1967509 |

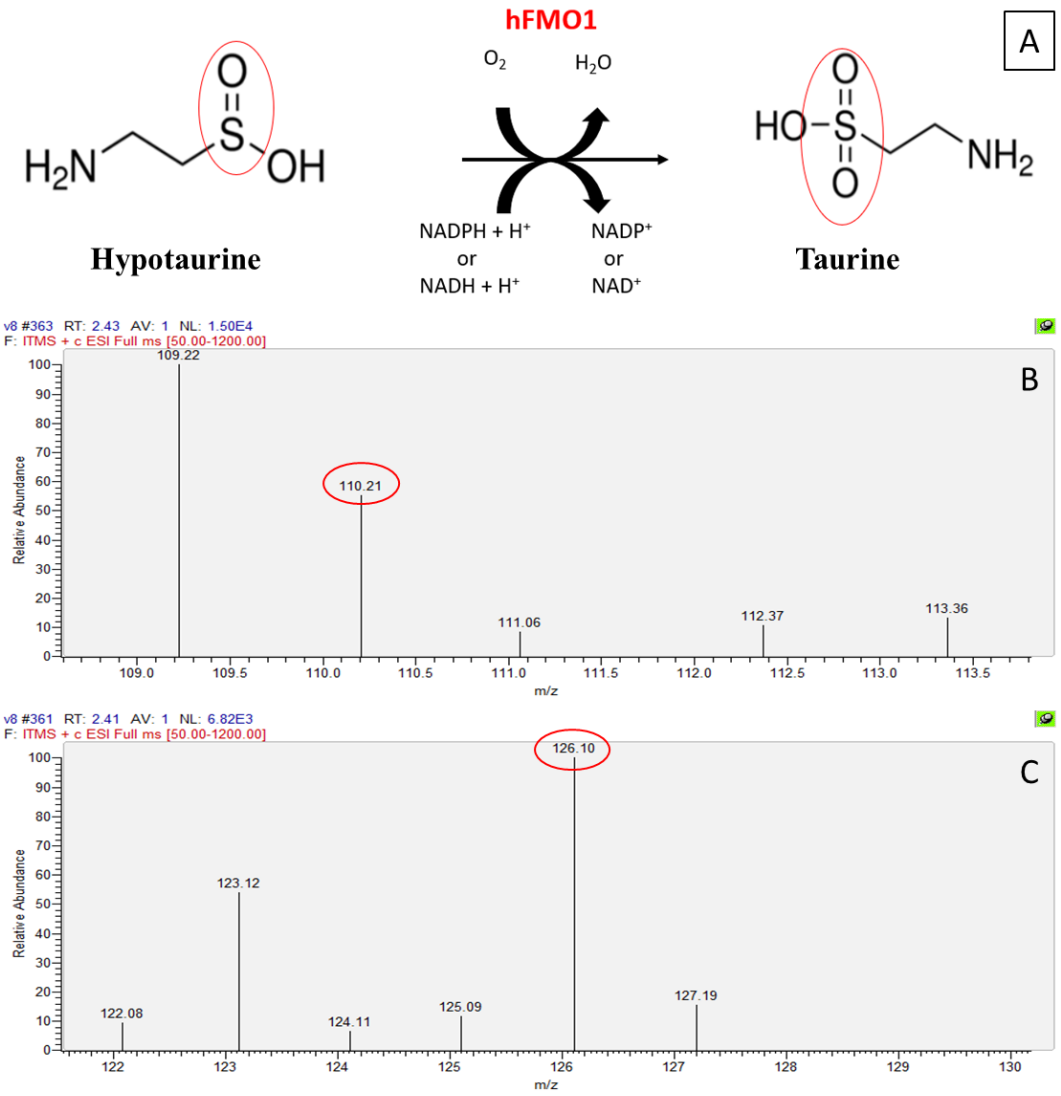


**Figure 13: (A)** The scheme of hypotaurine conversion to taurine by hFMO1. The mass spectra of Sample 6: **(B)** fragmentation profile of hypotaurine (m/z 110.21), **(C)** fragmentation profile of taurine (m/z 126.10)

The next substrate to be tested was benzydamine. The enzymatic reaction mixture in this case was analysed HPLC and the results are shown in Figure 14A. The HPLC chromatogram in Figure 14B demonstrates that the product, benzydamine N-oxide, was formed and detected with a retention time of 12 min only in the sample with hFMO1 (red trace). The chromatogram of the control reaction carried out with the denatured enzyme, shows only the presence of benzydamine with a retention time of 8.8 min.

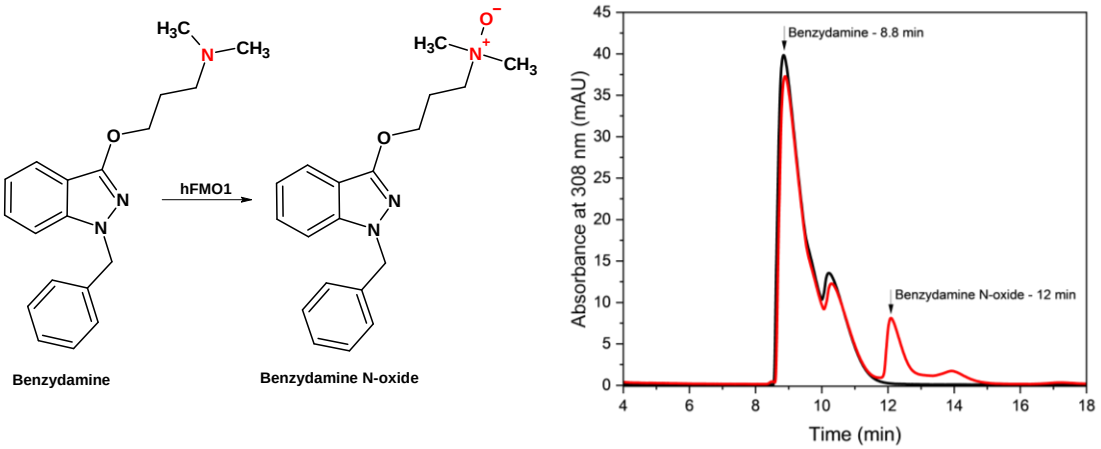


**Figure 14: (A)** The scheme of benzydamine oxidation mediated by hFMO1. **(B)** HPLC chromatograms of the in vitro oxidation of the benzydamine by hFMO1 (red trace) and the control (black trace).

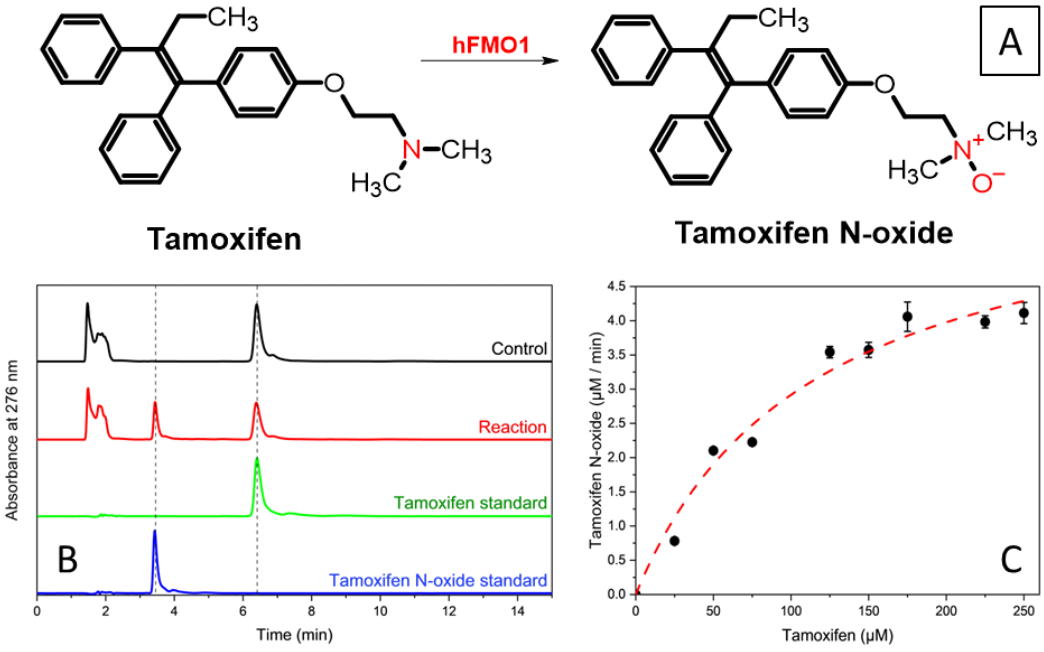


**Figure 15: (A)** The scheme of tamoxifen oxidation mediated by hFMO1. **(B)** HPLC chromatograms of the in vitro oxidation of tamoxifen by hFMO1, with the active enzyme (red trace) and control sample with the denatured enzyme (black trace). Standards of tamoxifen and tamoxifen N-oxide are shown in green and blue, respectively. **(C)** Michaelis-Menten kinetics for the formation of tamoxifen N-oxide. Estimated standard errors of three different experiments are represented as error bars.

The next substrate to be tested with the purified hFMO1 was tamoxifen, currently used for the treatment of breast cancer. The reaction mixute of tamoxifen oxidation to its N-oxide mediated by hFMO1, Figure 15A, was also analysed by HPLC and the resulting chromatograms are shown in Figure 15B. Tamoxifen N-oxide was eluted with a retention time of 3.5 min and only observed in the sample with the active hFMO1 (red trace) whereas the control reaction showed only the presence of tamoxifen with a retention time of 6.5 min. In this case, different concentrations of tamoxifen were used in order to calculate the kinetic parameters. The kinetic parameters $K_m$ and $k_{cat}$ were calculated from the amount of the product formed and were found to be 114.1 µM and 0.21 $s^{-1}$, respectively. These kinetic data are in line with previously published values [68], confirming the structural as well as functional integrity of the purified enzyme.

The penultimate substrate to be tested was dasatinib, a targeted therapy medication used for the treatment of chronic myelogenous leukemia. Dasatinib and its N-oxide were also separated by HPLC and identified by comparison with commercially available standards as shown in Figure 16B. The retention times of dasatinib and its N-oxide were 4.1 min and 5.4 min, respectively. Product was only present in the sample where the active hFMO1 was incubated in the presence of dasatinib and NADPH (red trace). The kinetic parameters $K_m$ and $k_{cat}$ were calculated from the amount of the product formed and were 40.9 µM and 0.11 $s^{-1}$, respectively. These kinetic data are in line with previously published values for the family of hFMOs [132].

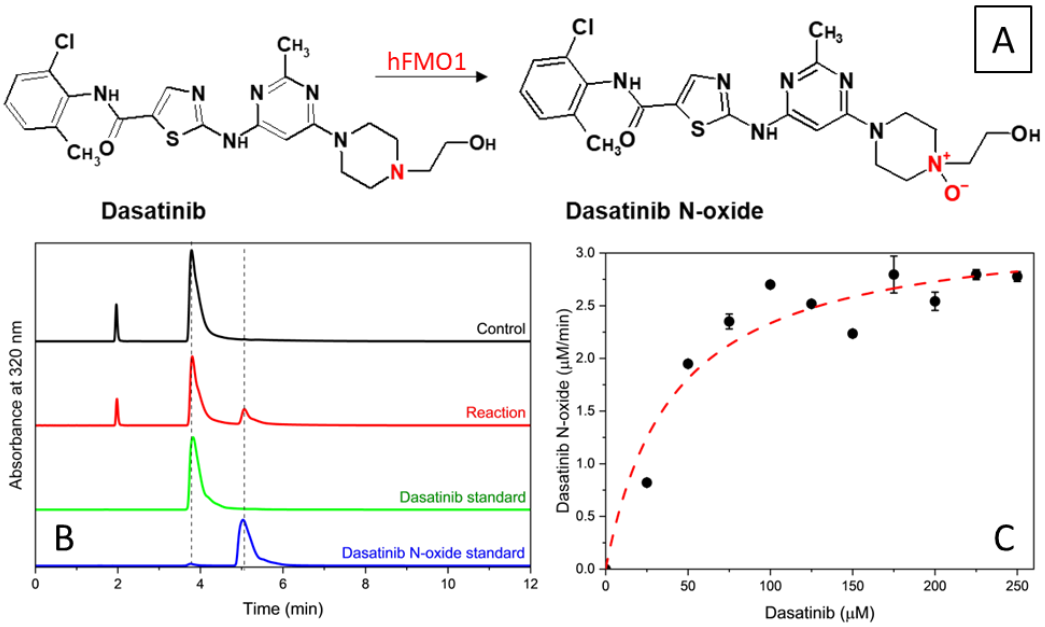


**Figure 6: (A)** The scheme of dasatinib oxidation mediated by hFMO1. **(B)** HPLC chromatograms of the in vitro oxidation of dasatinib by hFMO1 (red trace) and control sample with the denatured enzyme (black trace). Standards of dasatinib and dasatinib N-oxide are shown in green and blue, respectively. **(C)** Michaelis-Menten curve for the formation of the dasatinib N-oxide by hFMO1 with different concentrations of dasatinib. Estimated standard errors of three different experiments are represented as error bars.

The last substrate to be tested with the purified hFMO1 was vandetanib, used in treatment of certain tumours of the thyroid gland. Similar to previous enzymatic reactions, vandetanib and vandetanib N-oxide were separated by HPLC and identified by comparison with commercially available standards, Figure 17B, with observed retention times of 13 min and 9 min, respectively. As was expected, the product of the catalytic reaction was detected only in the sample where the active hFMO1 was incubated in the presence of vandetanib and NADPH (red trace). The kinetic parameters $K_m$ and $k_{cat}$ were calculated from the amount of the product with values of 45.4 μM and 0.06 $s^{-1}$, respectively. These kinetic data are also found to be in line with previously published values for the family of hFMOs [73].

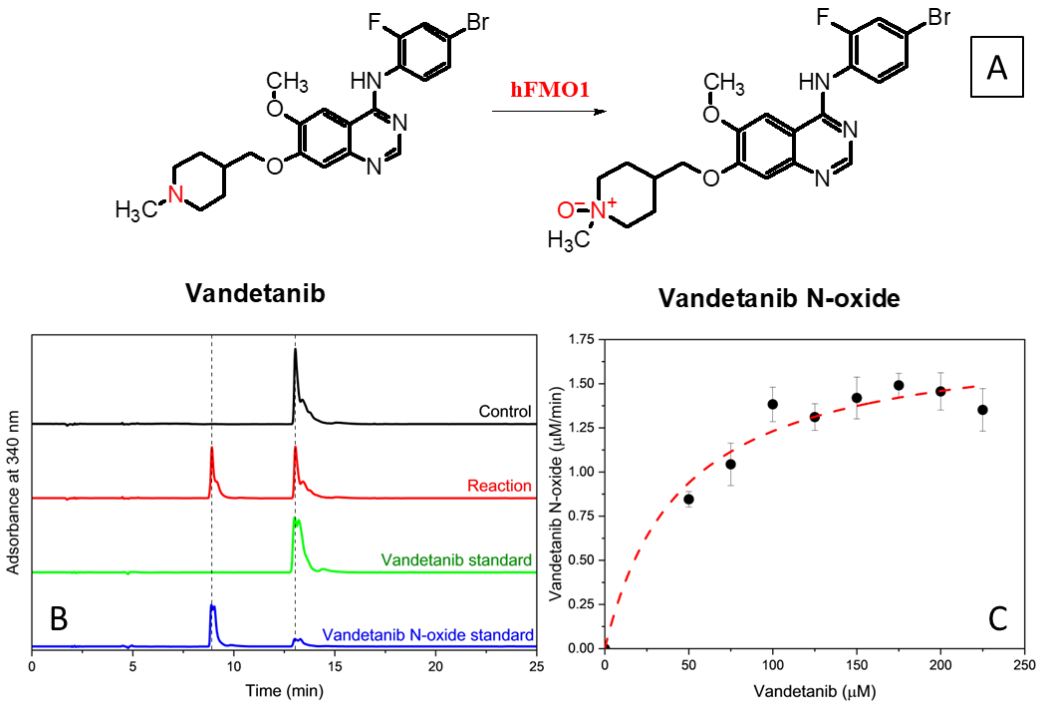


**Figure 17: (A)** The scheme of vandetanib oxidation mediated by hFMO1. **(B)** HPLC chromatograms of the in vitro oxidation of vandetanib by hFMO1 (red trace) and the control sample with the denatured enzyme (black trace).Standards of vandetanib and vandetanib N-oxide are shown in green and blue, respectively. **(C)** Michaelis-Menten curve for the formation of the vandetanib N-oxide by hFMO1 in the presence of different concentrations of the substrate. Estimated standard errors of three different experiments are represented as error bars.

To summarize, human FMO1 was successfully expressed in *E. coli* and purified. The structural, as well as functional integrity of the enzyme, was confirmed by various spectroscopic measurements and the enzyme showed its monooxygenation activity for S- and N-containing substrates. The thermal stability of the enzyme was estimated by DSC in the presence and absence of the cofactors where NADPH and NADH demonstrated different behaviors. Using the colourimetric metimazole assay it was found that the enzyme can use both NADPH as well as NADH as reducing agent and this requires further and in more depth investigations.

# Chapter 3

# Transient kinetics of hFMO1

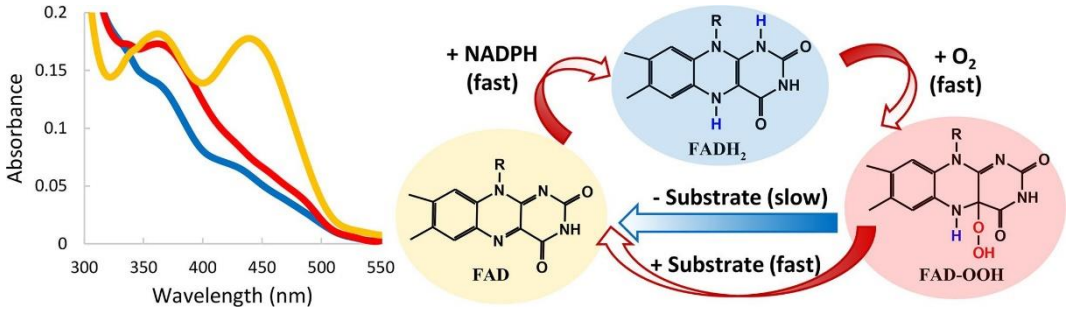


This work has been published:

**Cheropkina, H.**, Catucci, G., Marucco, A., Fenoglio, I., Gilardi, G., & Sadeghi, S. J. (2021). Human flavin-containing monooxygenase 1 and its long-sought hydroperoxyflavin intermediate. *Biochemical Pharmacology* 193.

DOI: https://doi.org/10.1016/j.bcp.2021.114763

# 3.1. Introduction

Phase I drug metabolism involves monooxygenase enzymes that are able to split the two atoms of molecular oxygen with the insertion of one of them in a stable, often unreactive, carbon atom or a heteroatom (sulfur or nitrogen) of the substrate (drug) with concomitant production of a water molecule [12,13,137,138]

The catalytic cycle of these enzymes involves the formation of an oxygen-reactive intermediate that is of a different nature depending on the cofactor present in the enzyme. In cytochrome P450 enzymes, the most studied monooxygenases, this intermediate consists of an oxyferryl intermediate of the haem cofactor. This intermediate has been spectroscopically identified [139] and in some cases characterized by trapping techniques and cryocrystallography [140,141]. As for the other most studied monooxygenase family, flavin-containing monooxygenases (FMOs), the C4a-hydroperoxyflavin intermediate of the FAD is responsible for the heteroatom oxidation of the substrate, and to this date, it has been spectroscopically characterized for the bacterial FMO [142], isoform-3 of the human enzyme (hFMO3) [126] and the isoform-1 of pig (pFMO1) [143–146]. The lifetime of these intermediates is very different, the pFMO1 lasting in the hour timescale, while hFMO3 lasts for minutes at 15 °C [126,144]. The lifetime of this reactive intermediate is a very important parameter because it has relevant consequences on the catalytic performance of the enzyme. Indeed, the catalytic cycle of the FMO enzymes involves the formation of the reactive intermediate before substrate binding. Consequently, a short-lived intermediate risk promotes the formation of hydrogen peroxide or superoxide, uncoupling the consumption of reducing units and oxygen from the formation of the oxidized product [14,146,147]. On the other hand, a long-lived intermediate results in highly coupled enzymes.

There are currently no published data on human FMO1 regarding pre-steady state or steady state characterization using NADPH/NADH. After the initial stopped-flow experiments of Beaty and Ballou more than 40 years ago, which led to the identification of the important intermediate in the catalytic cycle of these flavoenzymes [143], the C4a-hydroperoxyflavin for pig FMO1, this stable intermediate has been only inferred for human FMO1 and never observed spectroscopically. Only recently, AncFMO1 was tested in pre-steady state conditions, but the intermediate was unstable, and its formation could not be followed [28].

Dr. Daniel Ziegler's lab was the first to determine the catalytic mechanism of the first mammalian FMO, pig liver FMO, during 1970s to 1990s [148]. Later, Beaty and Ballou provided the first evidence of the full reaction mechanism of FMOs in the 1980s [143,144]. In a remarkable reference work for the field, it was shown how pFMO1 was initially reduced by NADPH followed by binding of molecular oxygen and stabilization of a long-lived hydroperoxy-intermediate [143] that still today is ascribed as the moiety responsible for catalysis.

As mentioned above, the stopped-flow experiments of Beaty and Ballou were performed using the pFMO1 [143], but five different FMO genes are present in humans [149,150]. The most relevant isoforms for drug metabolism are FMO1 and FMO3 which are also polymorphic [22,151,152]. In addition, FMO5 is also expressed in the liver and some recent publications suggest that it is an important drug-metabolizing enzyme capable of carrying out atypical Baeyer-Villiger oxidations in addition to soft nucleophilic heteroatom monooxygenation [17,19]. In the last 40 years bioinformatics and recombinant DNA technology have allowed for the designing of clones and the subsequent heterologous expression of FMOs in bacterial hosts such as *E. coli* [153]. More recently it has been shown that hFMO3, which for a long time was thought to behave like pFMO1, only transiently binds the substrate [154]. Stopped-flow experiments demonstrated that hFMO3 forms and stabilizes only a small amount of intermediate in the presence of oxygen that rapidly decays [11]. A role for $NADP^+$ in the stabilization of the intermediate and the overall structure of this enzyme was also demonstrated [11,121].

The real physiological substrate of hFMO1 was only discovered recently. The research group of Shephard used metabolite analysis by $^1H$ NMR spectroscopy to decipher the role of hFMO1 in the biosynthetic pathway of taurine using hypotaurine as its substrate. Taurine, a highly abundant amino acid in humans, can be synthesized de novo from hypotaurine. Furthermore, they also demonstrated the pH-dependent ability of hFMO1 to use either NADH or NADPH as a reducing cofactor [33].

As the chemical nature of the C4a-hydroperoxyflavin intermediate is the same in all the FMO enzymes, its lifetime and therefore reactivity is modulated by the protein environment. Two different approaches can be followed: (1) resolving the crystal structure and looking at the protein matrix surrounding the flavin cofactor to justify any differences observed in the catalytic activity of different FMOs and/or (2) investigating the formation and decay of the FAD intermediate by spectroscopy. Regarding the first option, to date no 3D structure of any human FMO has been

resolved since they are membrane-bound proteins and not stable in an aqueous environment [30]. Association with the membrane is a well-known hindrance to the general crystallization process of proteins. To overcome this obstacle, synthetic genes coding for ancestral FMO isoforms were recently synthesized and the resulting synthetic proteins were crystalized leading to the structures of AncFMO2, AncFMO3-6, AncFMO5 and AncFMO1 [28,155]. In this work the second option was followed in order to investigate the reactivity of this intermediate in hFMO1 and compare its behavior to other human FMOs as well as its homologous counterpart, pFMO1 (83.1% amino acid similarity).

## 3.2. Materials and methods

### Reagents

The main reagents such as NADPH, NADH, hypotaurine, $H_2O_2$, Amplex Red assay kit (Invitrogen), xanthine, xanthine oxidase, methanol, triethylamine and salts were all purchased from Sigma-Aldrich. Tamoxifen and tamoxifen N-oxide from Toronto Research Chemicals (Canada) and 5-(diethoxyphosphoryl)-5-methyl-1-pyrroline-N-oxide from DEPMPO (Enzo Life Sciences). All used chemicals were purchased HPLC grade and were used without any purification. All media, solutions, and buffers were prepared with deionized Milli-Q water.

### Rapid kinetics of reductive and re-oxidative half-reactions

Rapid kinetic experiments were performed using the Hi-Tech scientific SF-61 (single mixing controlled by Kinetic studioV3 software, HI-TECH Scientific, UK) stopped-flow instrument under anaerobic conditions in a glovebox (Belle Technologies, UK). Solutions needed for the analysis were prepared in outgassed 0.1 M phosphate buffer pH 7.4, except where oxygen was required for protein re-oxidation. The protein re-oxidation process was initiated by fully reducing 10 μM hFMO1 by 1.2 equivalent of NADPH. Once reduced, the protein solution was subsequently mixed with an oxygen-saturated buffer with/without hypotaurine solution, as substrate. All re-oxidation experiments were carried out at 15 °C. Previously published data have indicated that the C4a-hydroperoxyflavin intermediate absorbance can be monitored between 360 and 380 nm [156]. In this work, the formation of C4a-(hydro)peroxyflavin intermediate was followed at 368 nm as in the case of AncFMO1 [28] and the re-oxidized FAD at 450 nm.

Reductive half-reaction was monitored in the presence of different NADPH or NADH concentrations by mixing 1:1 v/v with protein solution at 15 °C. The rate of the reduction process was estimated by following the absorbance decrease at 450 nm. Both re-oxidation and reduction half-reactions were analyzed by Kinetic Studio Version 5.1.0.6 software and reduction rates with increased ligand concentrations were fitted using non-linear regression analysis using OriginPro 2021. All experiments were carried out in triplicates.

## Enzyme NADPH consumption assay

NADPH/NADH consumption by hFMO1 was monitored by Agilent HP-8453E spectrophotometer at 340 nm. Reaction mixtures typically contained: 0.2 μM hFMO1 in 0.1 M phosphate buffer pH 7.4 with different concentrations of NADPH/NADH ranging from 0 to 500 μM. The reaction was followed for 300 sec at 37 °C. The initial velocity was estimated by following the consumption of NADPH at 340 nm ($\varepsilon_{NADPH/NADH}$ = 6220 $M^{-1}cm^{-1}$). Kinetic parameters $K_M$ and $k_{cat}$ were estimated by fitting the data (five replicates of each data point) with the Michaelis-Menten equation using OriginPro 2021 software. All steady-state reactions were carried out following the initial setup of linearity regarding both time and enzyme concentration.

## Uncoupling reactions

Enzymatic reactions were analyzed for: **a)** the oxidation of NADPH, **b)** the formation of the tamoxifen N-oxide product and **c)** the production of $H_2O_2$. Each reaction was prepared in 200 μL total volume of 0.1 M phosphate buffer pH 7.4 in the presence or absence of 100 μM tamoxifen as substrate, 0.5 μM purified hFMO1 and 0.5 mM NADPH. Reactions were incubated at 37 °C for either 5 or 30 min in the dark. After reaching the required incubation time (5 or 30 min.), the reaction mixture was divided into three aliquots to estimate the oxidized NADPH, tamoxifen N-oxide and $H_2O_2$. All experiments were carried out in triplicates.

The amount of consumed NADPH was monitored spectrophotometrically at 340 nm, using 6220 $M^{-1}cm^{-1}$ as extinction coefficient and a sample/buffer dilution of 1:4. To measure the conversion of tamoxifen to tamoxifen N-oxide by hFMO1, 100 μL of the reaction mixtures were mixed with 50 μL of ice-cold acetonitrile to terminate the reaction, centrifuged at 12,000×g for 5 min and the supernatant was injected into HPLC to separate and quantify the N-oxide product. The quantification of $H_2O_2$ was carried out using the Amplex Red assay kit (Invitrogen)

as previously reported [14] with minor modifications. 50 µL of the reaction mixture was heated to 95 °C for 5 min to terminate the enzymatic reaction. The sample was centrifuged at 12,000×g for 5 min and the supernatant was diluted 5 times in the reaction buffer before performing a 1:2 dilution with 50 µL of AMPLEX RED mix. Samples were incubated for 5 min at 25 °C before analysis. Hydrogen peroxide formation was estimated as a linear function from an absorbance intensity at 570 nm of resorufin formation.

## High-Performance Liquid Chromatography

The separation and quantitation of the enzymatic reaction product were carried out by HPLC using the commercially available standards of both tamoxifen and tamoxifen N-oxide. Analysis was performed with an Agilent 1200 quaternary pump HPLC System equipped with a diode array UV detector (Agilent Technologies, USA) with a Kinetex 5 µm EVO C18 100 Å LC column 250 × 4.6 mm. Tamoxifen and its metabolite were separated by isocratic elution and were detected at a wavelength of 276 nm. The mobile phase consisted of 82% of methanol and 18% of 1% triethylamine, analysis time was 20 min with a flow rate of 1.1 mL/min [16]. The retention time of tamoxifen and its N-oxide product was 6.5 min and 3.5 min, respectively.

## Detection of superoxide by Electron Paramagnetic Resonance (EPR) spectroscopy

Trapping of superoxide using 5-(diethoxyphosphoryl)-5-methyl-1- pyrroline-N-oxide (DEPMPO, Enzo Life Sciences) was performed as previously reported [157] with minor modifications. hFMO1 or hFMO3 (5.3 µM) was incubated with 6.7 mM NADPH in phosphate-buffered saline (100 mM, pH 7.4) in the presence of 50 mM DEPMPO. To initiate the reaction, the enzyme was added. EPR spectra were recorded at room temperature using a Miniscope 100 EPR spectrometer, (Magnettech, Berlin, Germany). Instrument settings: microwave power 7 mW, modulation amplitude 1 G, scan time 80 s, two scans. Each incubation with the spin trap was immediately drawn into 50 µL capillary Ringcaps® (Duran glass, Hirschmann Laborgerate). EPR signal intensities were obtained at 0–20 min recording the spectra every 3 min.

DEPMPO/superoxide adduct had the highest intensity at 6 min. A positive control experiment was carried out with 0.36 mM xanthine and 0.01 U/mL of xanthine oxidase in 50 mM KPi buffer pH 7.4 in the presence of 50 mM DEPMPO.

The computer simulations of the experimental EPR signals were performed using the WinSim 2002 software (NIH, USA).

## 3.3. Catalytic mechanism of the hFMO1 and substrate preferences

The catalytic activity of the FMO1 enzyme and FAD reoxidation cycle was already demonstrated by Poulsen and Ziegler [11] on the base of the pig liver microsomes, Figure 18 is demonstrated a detailed catalytic cycle that is relevant also for the human FMO1.

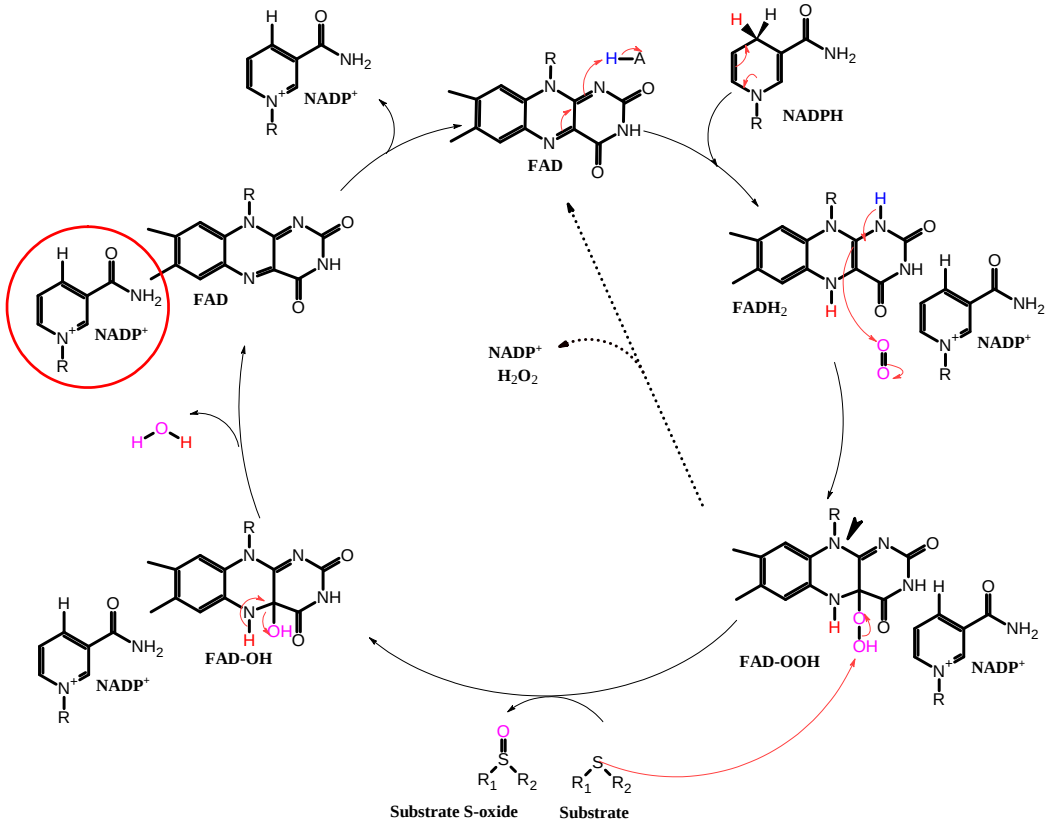


**Figure 18:** The scheme of chemical steps of the FAD cofactor redox process in the hFMO1 catalytic cycle.

In the initial step of the catalytic reaction, the enzyme-bounded oxidized FAD gets reduced by using the stoichiometric amount of the reducing equivalent from the NADPH. When bound to the enzyme the reduced $FADH_2$ prosthetic group is ready to react with the molecular oxygen forming the long-live C4a-hydroperoxyflavin intermediate, stabilized by $NADP^+$ still bound to the active site.

The water formation, from the second oxygen atom, causes the complete breakdown of FADH-OH with the following step of the $NADP^+$ releasing and completing the reoxidizing of the FAD cofactor. Another oxygen atom from the FAD-OH is getting in a couple with two hydrogens to form the molecule of the water that is realized with the following step of the $NADP^+$ releasing and completing the reoxidizing of the FAD cofactor. If during the catalytic reaction, the hyroperoxyflavin intermediate wasn't stabilized strong enough, it may cause the spontaneous "uncoupling" reaction, wasting reducing equivalents and the molecules of the oxygen followed by hydrogen peroxide formation and reoxidation of the FAD cofactor. The catalytic efficiency of the FMOs enzymes depends on the lifetime of the intermediate. The lower the percentage of "losses" of reducing equivalent by the enzyme, the higher catalytic performance it can provide.

## 3.4. Reductive half-reaction

To understand the NADPH/NADH cofactor preference of hFMO1 the kinetics of the reduction half-reaction, Figure 19, was studied in both pre-steady and steady-state. Both measurement modes are necessary for a complete understanding of the reduction process and any limitations if present.

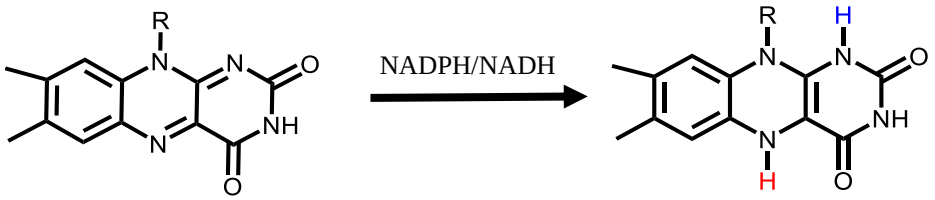


Oxidized form FAD  Reduced form $FADH_2$

**Figure 19:** The scheme of FAD cofactor reduction by NADPH/NADH in the hFMO1 catalytic cycle.

The steady-state kinetics measurements help to estimate the NADPH/NADH specificity of an enzyme by using initial rates of substrate consumption reactions by the enzyme. But to assess the significance of this preference, pre-steady state conditions were used to estimate the reductive efficiency of NADPH and NADH as electron donors of the hFMO1 enzyme. Pre-steady state kinetic helps to measure the reaction intermediates' formation in the initial reaction cycle by monitoring the burst phase of the catalytic reaction directly from the moment of mixing enzyme with the substrate, where no intermediates exist, until their steady-state concentrations are reached.

## 3.4.1. Steady-state kinetic analysis of NADPH/NADH binding

The CD and DSC data did not exclude a possible role of $NAD^+$ in FMO1 catalysis. Therefore, the ability of the enzyme to use either NADH or NADPH as a source of reducing unit was investigated by methimazole oxidation assay. Since pH 7.4 represents a physiological benchmark and for hFMO1 it has been previously reported that both cofactors are equally effective for catalysis at this pH [33], all experiments were conducted at pH 7.4.

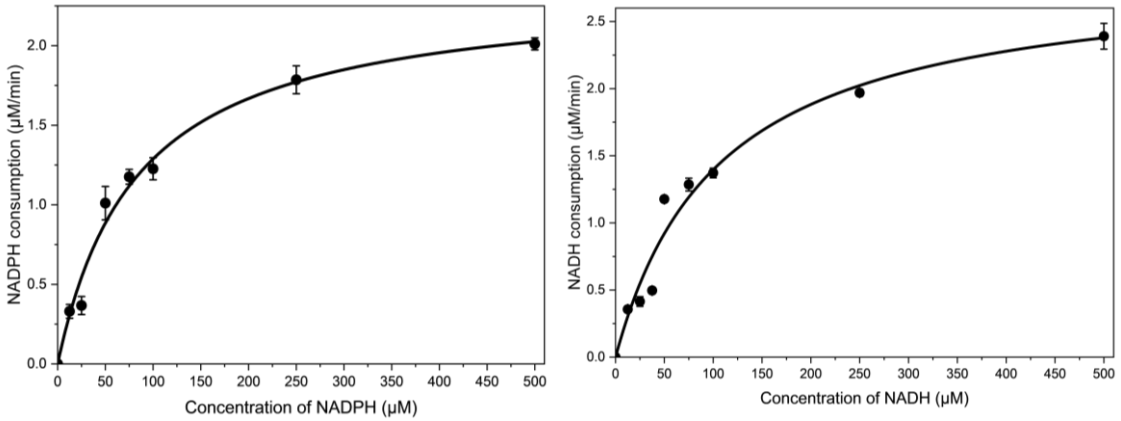


**Figure 20:** Michaelis-Menten plot of the steady-state kinetic parameters of hFMO1 in the presence of **(A)** NADPH and **(B)** NADH. Measurements were carried out in 0.1 M phosphate buffer pH 7.4. Estimated standard errors of five different experiments are represented as error bars.

Steady-state kinetic measurements of hFMO1 were carried out in order to study the NADPH/NADH specificity of this enzyme by following the initial rates of substrate consumption. Steady-state kinetics experiments were performed at a fixed hFMO1 concentration with various NADPH/NADH concentrations. Kinetic parameters $K_M$ and $k_{cat}$ were calculated by fitting the data (initial rates of the NADPH/NADH consumption as a function of the concentration of substrate) with the Michaelis-Menten equation (Figure 20). Similar $v_{max}$ values were calculated under these conditions ($2.36 \pm 0.096$ μM/min for NADPH and $2.88 \pm 0.12$ μM/min for NADH) however, the $K_M$ value determined for NADH was slightly higher than that of NADPH (Table 7), indicating the lower affinity of hFMO1 for NADH. Some differences are observed in the $k_{cat}$ values and also the resulting $k_{cat}/K_M$, taken together suggesting the preference of hFMO1 for NADPH.

**Table 7:** Steady-state kinetic parameters for the hFMO1 at pH 7.4

| Ligand | $K_M$, [μM] | $k_{cat}$, [$s^{-1}$] | $k_{cat}/K_M$, [$s^{-1}/M$] | Ref |
|---|---|---|---|---|
| **NADPH** | 83.46 ± 9.3 | 0.19 ± 0.008 | 2276.54 ± 271.18 | present work |
| **NADH** | 106.65 ± 10.4 | 0.24 ± 0.01 | 2250.35 ± 238.63 | |
| **NADPH** | 55 ± 13 | 0.13 ± 0.01 | 2400 | [28] |
| **NADH** | 91 ± 17 | 0.11 ± 0.009 | 1200 | |

In general, a similar behavior with NADP(H) and NAD(H) in steady-state reactions was not expected. These data are also in line with the previous report on pig FMO1 where it was found that $NADP^+$ converts the enzyme completely into a form that only exhibits a slower reduction rate [144]. Furthermore, NADP was able to stabilize the structure of AncFMO1 and also for this enzyme a higher $K_M$ for NADH is reported [28]. In the case of $NAD^+$ stabilization, no data is available for direct comparison.

## 3.4.2. Pre-steady-state kinetic analysis of NADPH/NADH binding

In order to assess the significance of cofactor preference, pre-steady state conditions were used to estimate the efficiency of NADPH and NADH as electron donors of the hFMO1 enzyme. Pre-steady state kinetic measurements followed the formation of FAD intermediates in the initial reaction cycle and to capture these intermediates stopped-flow experiments were carried out. Reductive half-reaction rates were measured under anaerobic conditions with increasing concentrations of NADH or NADPH. The dissociation constants $K_d$ and reduction rate constants $k_{red}$ were calculated by fitting the reductive half-reaction to the Michaelis-Menten equation following the decrease in absorbance at 450 nm.

Fitting the data resulted in a dissociation constant ($K_d$) of 4.79 ± 0.38 μM and a reduction rate constant ($k_{red}$) of 0.78 ± 0.01 $s^{-1}$. The hyperbolic behavior shown in Figure 21A indicates a single irreversible hydride transfer step with no other spectral changes at higher wavelengths. The same experiments were carried out under the same conditions using NADH as the reductant. Data analysis, in this case, resulted in a $k_{red}$ of 1.20 ± 0.03 $s^{-1}$ and a $K_d$ of 468.65 ± 30.38 μM (Figure 21B).

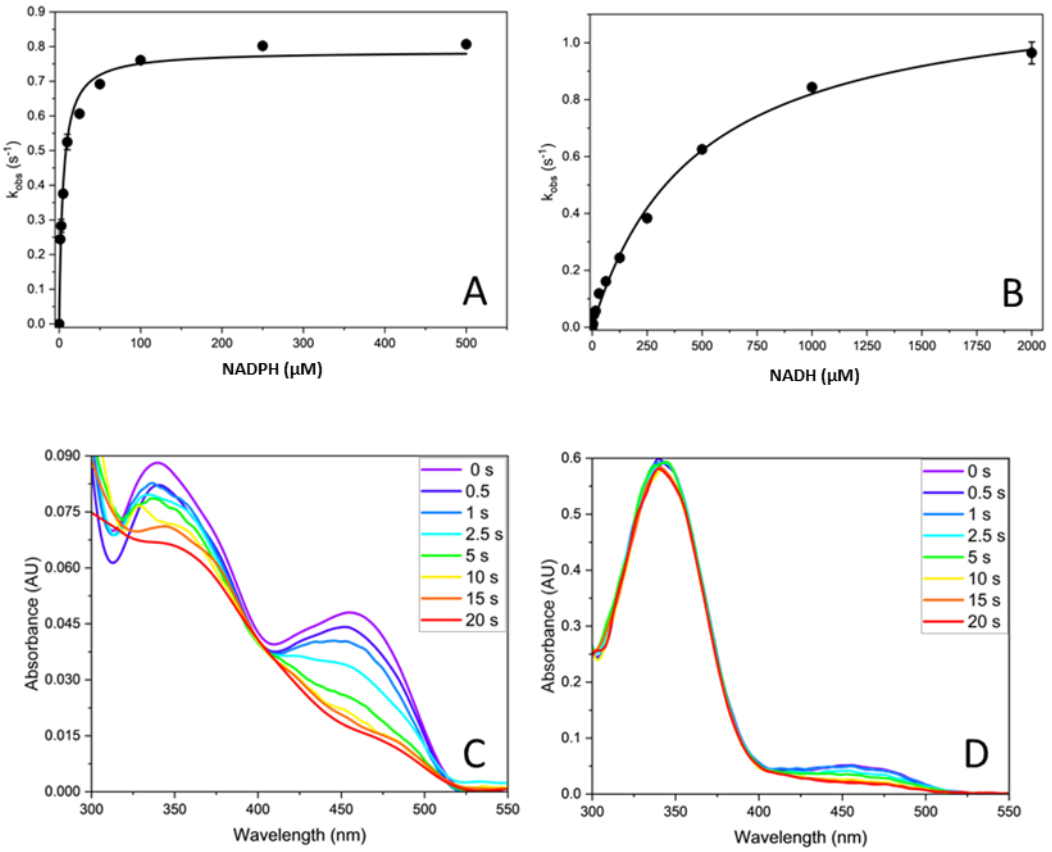


**Figure 21:** Pre-steady-state analysis of the hFMO1 reductive half-reaction. Hyperbolic fitting of the plots for **(A)** NADPH and **(B)** NADH. Reduction spectra of hFMO1 in the presence of an equimolar concentration of NADPH **(C)** and 1:25 of the enzyme to NADH **(D)**. Measurements were carried out in 0.1 M phosphate buffer pH 7.4 at 15 °C. The reduction rates at different concentrations of added ligands were determined by fitting the decreased absorbance at 450 nm as a function of time to a single exponential decay. Final reduction rates with increased ligand concentrations were fitted using non-linear regression analysis. The process of reduction was monitored starting from the mixing of the fully oxidized enzyme with the reducing agent. Estimated standard errors of three different experiments are represented as error bars.

Data from this reductive step indicates that hFMO1 can be reduced much more efficiently by NADPH and the Figure 21C-D demonstrated that the full reduction by NADPH was reached at the equimolar concentration with the enzyme, but in the case, with the NADH the ratio was 1:25. For this reason, experiments on the subsequent oxidation step in the presence of molecular oxygen were carried out only with NADPH.

## 3.5. Oxidative half-reactions

Reduced hFMO1 was rapidly mixed with oxygenated buffer and the formation and decay of the C4a-hydroperoxyflavin intermediate was followed at 368 nm as

shown in Figure 22 [28,126]. Moreover, the effect of the presence of the substrate on the re-oxidation process was investigated in the absence and presence of the substrate hypotaurine. Figure 23A and B show the spectral features of the reduced hFMO1 (black line), the C4a-hydroperoxyflavin intermediate formation (red line) and the re-oxidized species (green line) in the absence and presence of hypotaurine, respectively. It can be observed from the spectra that the C4a-hydroperoxyflavin intermediate builds up rapidly (within 2–3 s) but decays at a slow rate leading to the oxidized FAD.

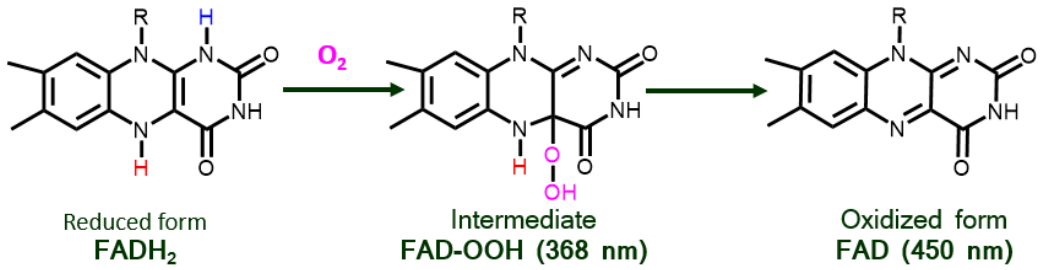


**Figure 22:** The scheme of chemical steps of the $FADH_2$ cofactor re-oxidation process in the hFMO1 catalytic cycle

Kinetic data following the re-oxidation of the flavin to its ground state were collected measuring the absorbance increase at 450 nm (Figure 23C). The kinetic traces demonstrate that the substrate hypotaurine accelerates the re-oxidation process which is completed in less than 200 s (black trace). On the other hand, in the absence of the substrate, even at 1750 s the enzyme is not fully re-oxidized (red trace).

Overall the stopped-flow data indicate that the hFMO1 C4a-hydroperoxyflavin intermediate is very stable and full re-oxidation can only be observed in the presence of the substrate. This is in keeping with previously published data by Beaty and Ballou [143]. In their work the pig FMO1 C(4a)-hydroperoxyflavin spectrum remained stable for at least 30 min (despite shaking of the cuvette), only partial reoxidation could be observed after 1 h 42 min and full re-oxidation was detected only in the presence of substrate [143].

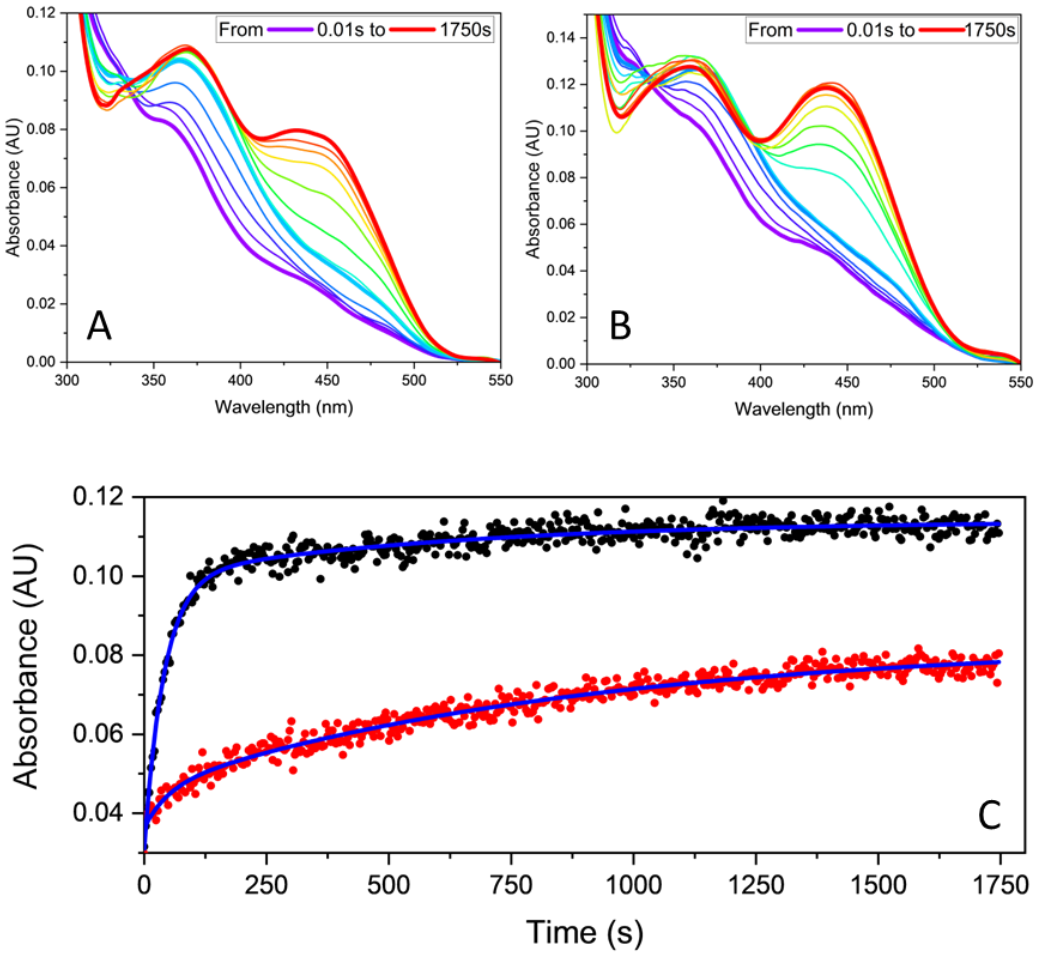


**Figure 23:** Oxidative half-reaction. The re-oxidation spectra of NADPH reduced hFMO1 in the presence of an oxygenated buffer. Selected spectra showing reduced (violet), intermediate (light blue) and re-oxidized flavin (red). **(A)** Traces in the absence and **(B)** in the presence of hypotaurine. **(C)** Comparison of the re-oxidation rates monitored at 450 nm in the absence (red dots) and in the presence (black dots) of hypotaurine. Measurements were carried out in 0.1 M phosphate buffer pH 7.4 at 15 ◦C. The re-oxidation process was monitored starting from the fully reduced protein (10 μM hFMO1 with 1.2 equivalents of NADPH).

Rates for the flavin re-oxidation, intermediate formation and decay all highlight significant differences in the behavior of hFMO1 when compared to previously reported data on hFMO3 [126] and AncFMO3-6 (a soluble synthetic protein based on the ancestral reconstruction of FMO isoforms 3–6) [155] as shown in Table 8. On the other hand, the remarkable stability of the intermediate of hFMO1 (around 30 min at 15 °C) is in line with what was reported for pig liver FMO1 where this was found to last for hours at 4 °C [143].

**Table 8:** Kinetic parameters of hFMO1 re-oxidation half-reactions

| Protein | FAD Intermediate (368 nm) | | Re-oxidation (450 nm) | Reference |
|---|---|---|---|---|
| | $k_{formation}$ [$s^{-1}$] | $k_{ox}$ [$s^{-1}$] | $k_{decay}$ [$s^{-1}$] | |
| **hFMO1 (without substrate)** | 1.383 | $R_1$ = 0.01429<br>$R_2$ = 0.00086 | <0.00001 | present work |
| **hFMO (with hypotaurine)** | 1.768 | $R_1$ = 0.02214<br>$R_2$ = 0.00312 | 0.0001 | present work |
| **hFMO3 (without substrate)** | 1.580 | $R_1$ = 0.790<br>$R_2$ = 0.0009 | 0.001 | [28] |
| **AncFMO3-6** | 3.7 | N/D | 0.01 | [155] |

## 3.6. Uncoupling reaction

Since the stopped-flow data point to a stable FAD intermediate, it was decided to also measure the levels of uncoupling in purified hFMO1 reactions, Figure 24. Previous data using baculovirus expressing hFMO1 have indicated that this enzyme is highly uncoupled producing 40–50% of $H_2O_2$ [146]. The same researchers also found that the addition of substrate did not significantly alter the amount of $H_2O_2$ being formed [146]. No uncoupling data on purified hFMO1 are currently available but purified hFMO3 was found to be 50–70% uncoupled when benzydamine is used as substrate [14].

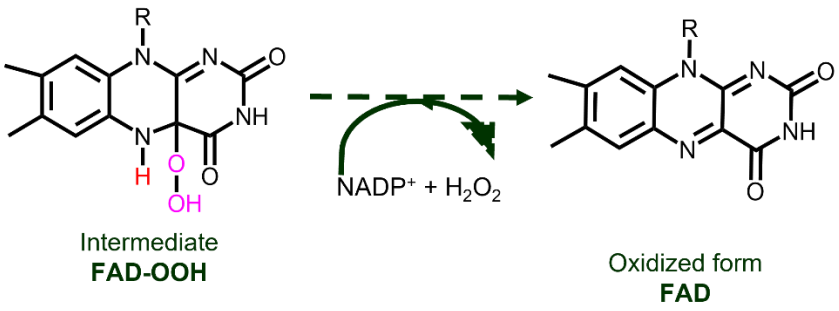


**Figure 24:** FMO "uncoupling" reaction where the hyroperoxyflavin intermediate is reoxidized and $H_2O_2$ produced without any substrate oxidation.

Whereas the high levels of uncoupling seen in hFMO3 match the intrinsic instability of its own intermediate [126], the data on baculovirus expressing hFMO1 are not in line with the remarkable stability of the C4a-hydroperoxyflavin intermediate published for purified pig FMO1 [140]. In addition, the data presented here on the stability of the purified hFMO1 intermediate is also contrary to the baculovirus expressing hFMO1. For this reason, the uncoupling reactions of

purified hFMO1 were investigated by initially measuring $H_2O_2$ production. For the coupled reaction tamoxifen was selected as the substrate because hFMO1 is known to catalyze its conversion to tamoxifen N-oxide and product formation can be quantified easily by HPLC separation, whereas hypotaurine requires a lengthy methodology for its product quantification. To maximize the comparability of the data NADPH oxidation, tamoxifen N-oxidation and hydrogen peroxide were measured from the same reaction mixture. NADPH oxidation was quantified by monitoring the decrease in absorbance at 340 nm, the amount of $H_2O_2$ produced was measured by mixing aliquots of each reaction with the AMPLEX red kit components, whereas the amount of tamoxifen N-oxide was calculated by HPLC analysis. The results obtained are shown in Figure 25.

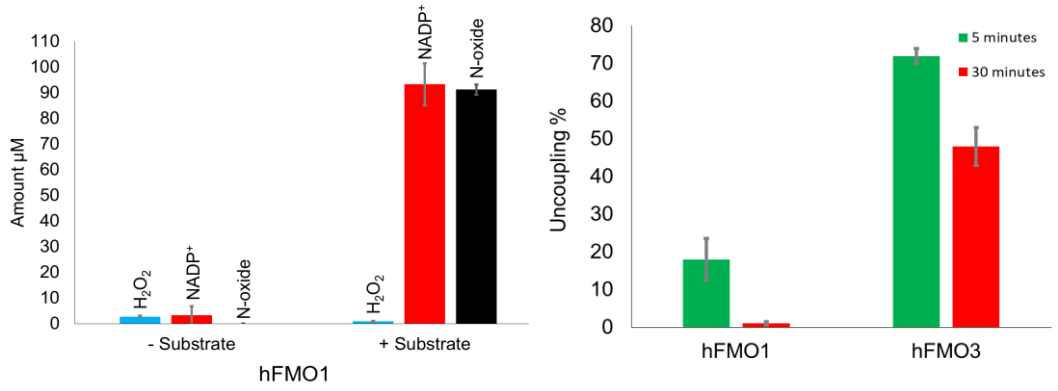


A B

**Figure 25:** Uncoupling measurements of hFMO1: **(A)** $H_2O_2$ (blue), $NADP^+$ (red) and tamoxifen N-oxide formation (black) in the absence or presence of the substrate tamoxifen after 30 min of reaction. **(B)** Comparison of the uncoupling reactions of hFMO1 and hFMO3. % uncoupling calculated as $H_2O_2$/NADPH oxidized by each enzyme in the presence of substrate after 5 or 30 min of reaction. Estimated standard errors of three different experiments are represented as error bars.

In the absence of substrate, 0.5 µM of hFMO1 consumes 3.3 µM of NADPH after 30 min of reaction, whereas the amount of $H_2O_2$ produced is 2.8 µM, respectively. This data indicates that very little NADPH is consumed by hFMO1 in the absence of substrate. On the other hand, in the presence of substrate, 0.5 µM of hFMO1 consumes ~93 µM of NADPH in 30 min of reaction, whereas the amount of $H_2O_2$ produced is ~0.9 µM respectively (Figure 25A). Indeed, NADPH consumption is almost 30 times higher in the presence of substrate indicating a strong coupling effect driven by tamoxifen. Furthermore, when the uncoupling is evaluated as the ratio of $H_2O_2$/NADPH it is as low as 1% (Figure 25B).

Contrary to the published data on the hFMO3 uncoupling, the unproductive shorter cycle leading to $H_2O_2$ leakage is a neglectable phenomenon for hFMO1 because the enzyme is highly coupled and it does not waste the reducing equivalents of NADPH unless a suitable substrate gains access to its active site. These data are fully in line with the stopped-flow data presented earlier with the purified enzyme where the half-life of the C4a-hydroperoxyflavin is found to be reasonably long and strongly influenced by the presence of the substrate. Tamoxifen conversion to tamoxifen N-oxide by hFMO1 results in a low level of uncoupling however we cannot exclude a substrate dependence phenomenon for hFMO1 reactions and further studies should aim at clarifying this point using either the physiological substrate, hypotaurine, or other N- or S-containing molecules.

Previously published data have indicated that hFMO3 forms not only hydrogen peroxide but to a lesser extent also the superoxide radical anion as the result of its uncoupling reactions [14]. In order to prove the different behavior of hFMO1 compared to hFMO3 and confirm the higher overall coupling of hFMO1, EPR spectroscopy experiments were carried out to detect the formation of any superoxide radical anion using the spin trap DEPMPO. The latter compound has a long-lived superoxide radical anion adduct (DEPMPO-OOH) with a half-life of 14.8 min [157,158]. EPR experiments were carried out with both purified hFMO1 and hFMO3 in the presence of large excess of NADPH and DEPMPO. As can be seen in Figure 26A, no EPR signal was observed for the hFMO1 reaction whereas hFMO3 displayed the typical spectrum of DEPMPO-OOH adduct with a maximum signal reached after 6 min of incubation with the spin trap (Figure 26B). As a positive control for visualization of the superoxide DEPMPO adduct, the xanthine/xanthine oxidase system was used since the EPR spectra of their DEPMPO-OOH adduct is already published [157,158] and the results are shown in Figure 26C.

**Table 9:** Coupling constants of the DEPMPO-OOH adduct.

| **Conformer** | **AP** | **AN** | **Ahβ** | **AHγ** |
|---|---|---|---|---|
| ***trans* 1 (94%)** | 48.92 | 12.80 | 10.81 | 0.87 |
| ***trans* 2 (6%)** | 40.27 | 13.57 | 8.22 | 0.81 |

The simulated spectrum of xanthine oxidase was also used for calculating the coupling constants of the DEPMPO-OOH adduct that are summarized in Table 9 and are comparable to previous literature reports [158].

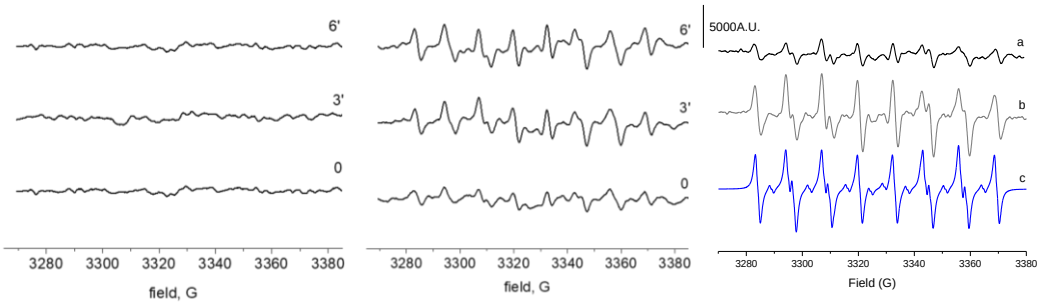


**A** **B** **C**

**Figure 26:** Representative EPR spectra of superoxide radical anion adducts of DEPMPO with either **(A)** hFMO1 or **(B)** hFMO3 reaction taken at three different time points. 50 mM DEPMPO was incubated with 5.3 µM hFMO and 6.6 mM NADPH in 50 mM KPi pH 7.4. **(C)** EPR spectra of DEPMPO-OOH of the reactions of a) hFMO3; b) Xanthine oxidase; c) computer-simulated spectrum of (b).

To summarize, human FMOs have not been studied in depth mainly due to the difficulties in producing the folded and active forms of the different isoforms of the enzyme. In this work, hFMO1 has been successfully purified after heterologous expression in *E. coli* in its folded and active form and this allowed us to follow its catalytic cycle including its reduction and re-oxidation steps. After the initial stopped-flow experiments of Beaty and Ballou more than 40 years ago which led to the identification of the important intermediate in the catalytic cycle of these flavoenzymes, C4a-hydroperoxyflavin [143], this intermediate has been captured for the first time in human FMO1 in the current work using the same methodology. The data demonstrate that human FMO1 differs from human FMO3 because it forms a more stable C4a-hydroperoxy intermediate that constitutes the basis for understanding the catalytic properties of this specific isoform.

Furthermore, since the stability of this intermediate results in a higher coupling of the enzyme reactions this means that, unlike human FMO3, the FMO1 is a more coupled enzyme. This was also proven experimentally by measuring the amounts of ROS produced by this enzyme; hFMO1 is <5% uncoupled compared to 50% hFMO3. Moreover, using EPR spin trapping experiments we further demonstrate that hFMO3 forms also the superoxide anion radical whereas no superoxide-adduct was observed for hFMO1.

Although hFMO1 and its enzymatic reactions have not been as extensively studied as the hFMO3, the kinetic as well as catalytic data presented here, demonstrate the different enzymatic behaviors of these two closely related human enzymes.

# Chapter 4

# Tandem bioelectrocatalysis: hFMO1 and CYP3A4

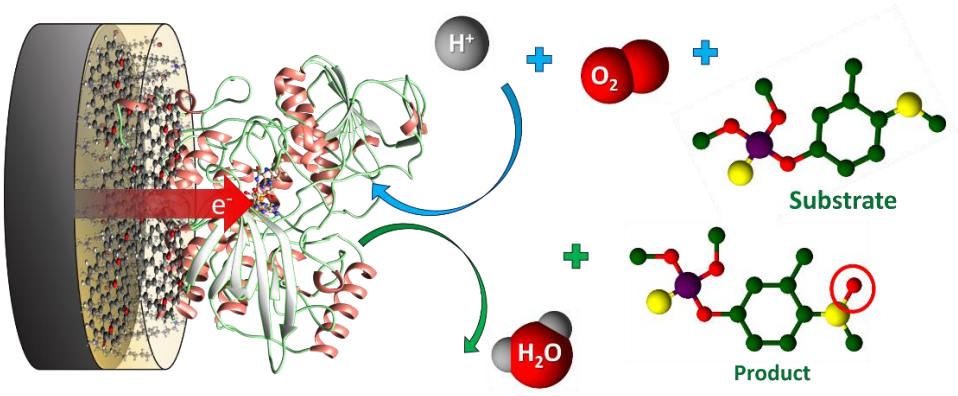


This work has been published:

**Cheropkina H.**, Catucci G., Cesano F., Marucco A., Gilardi G., Sadeghi S. J. (2022) Bioelectrochemical platform with human monooxygenases: FMO1 and CYP3A4 tandem reactions with phorate

DOI: https://doi.org/10.1016/j.bioelechem.2022.108327

# 4.1. Introduction

Pesticides are an integral part of agriculture for the prevention, control and elimination of pests. Yearly, >2.4 billion kilograms of broad-spectrum pesticides are used including mainly organophosphates, carbamates, organochlorines, neonicotinoids and pyrethroids [159]. But the majority of pesticides are hazardous chemicals and increasing the field of their action has led to significant attention to their toxicity and adverse influence on the environment and human health. Chronic exposure to low levels of pesticides can cause mutations [2]. Among the many pesticides, organophosphates and carbamates have also been classified as carcinogens as well as neurotoxic causing neurodegenerative diseases such as Parkinson's [160–162] and Alzheimer's [163–165]. This has led to legislators imposing limits for the maximum residual amounts for individual pesticides of 0.1 µg/L [136].

Exposure to organophosphate and carbamate pesticides can occur in occupational settings but also in general public. In the case of the general public, the main routes of exposure include dermal, inhalation and diet [166]. Once they have entered the human body, pesticides are mainly metabolized by two major classes of Phase I oxidative enzymes: cytochromes P450 and flavin-containing monooxygenases (FMOs) [167]. Cytochrome P450 monooxygenases (CYPs) are a superfamily of haem-containing proteins whereas the FMO family is quite small with only 5 functional members which have a FAD cofactor [6,12,168]. Both families are NADPH dependent but FMOs are capable of accepting electrons directly from NADPH whereas CYPs require a NADPH reductase. Both enzyme families have been extensively studied in relation to the detoxification of pesticides. In the case of organophosphate pesticides, the P450 enzymes have been shown to be involved in oxidative transformations resulting in oxon, sulfoxide and sulfone [169] whereas the FMOs only produce sulfoxides [8]. Previous studies by Furnes and Schlenk have shown that amongst the 5 different FMO isoforms, the extrahepatic FMO1 primarily found in kidneys and intestines, is the most efficient in catalyzing the sulfoxidation of carbamate and organophosphate pesticides [31]. Other in vitro studies of pesticide metabolism mediated by hFMO1 have described the preference of this enzyme for the oxidation of sulfur atoms with a high level of stereoselectivity and catalytic efficiency [31,9,45].

The main method for determination of the activity of these enzymes towards the pesticides has been the in vitro enzymatic assay where the reductant NADPH is added to initiate the reaction. An alternative method can be the use of electrodes

where these enzymes are immobilized and which have successfully been applied to drug metabolism studies [170–172]. In addition, in order to miniaturize the electrode and enhance the sensing characteristics, different nanostructured materials are widely used such as gold nanoparticles, graphene and its derivates. The main advantages of using nanostructured materials in enzyme electrodes is their efficient electrocatalyst properties, high surface area or surface-to-volume ratio and enhancement of electron transfer [93]. One such material is graphene oxide which has occupied a dominant place in the biosensing field due to its efficient electrochemical and catalytical properties [94,95].

In this work, human FMO1 (hFMO1) is initially immobilized on glassy carbon electrodes in the presence of graphene oxide (GO) for investigating the feasibility of following the oxidation of different pesticides by the enzyme. The GO monolayers are functionalized by the cationic surfactant dimethyldidodecylammonium bromide (DDAB) to avoid denaturation of this enzyme [110,111] and surface properties of functionalized GO sheets are investigated by contact angle and atomic force microscopy (AFM). Three well-known substrates of hFMO1, organophosphate pesticides phorate and fenthion as well as the carbamate insecticide, methiocarb, are chosen and voltammetric titrations are carried out for the determination of kinetic parameters. Subsequently and more interestingly, the possibility of mimicking the complexity of the in vivo metabolic reactions of phorate within the human body is investigated in an in vitro tandem bioelectrochemical setup with hFMO1 and CYP3A4 (cytochrome P450 3A4 the most important hepatic P450 in terms of xenobiotic metabolism). The data obtained confirm the possibility of using immobilized hFMO1 and CYP bioelectrodes for the in vitro prediction of the metabolic fate of pesticides.

## 4.2. Material and methods

### Reagents

Riboflavin, FAD, IGEPAL, β-mercaptoethanol, glycerol, PMSF, lysozyme, NADPH, didecyldimethylammonium bromide (DDAB), phorate, phorate S-oxide, phorate sulfone, fenthion, fenthion S-oxide, methiocarb, methiocarb S-oxide, acetonitrile, phosphoric acid, methanol, and salts were all purchased from Sigma-Aldrich. Phorate oxon sulfoxide was purchased from Toronto research chemicals, Canada. GO (4 mg/mL, water dispersion) was purchased from Graphenea (Donostia, Spain). PK-4 Polishing Kit and all supplements for electrochemical measurements were from BASi (USA). All chemicals were of the highest quality

and used without any further purification. All media, solutions, and buffers were prepared with deionized Milli-Q water.

## Purification of human FMO1

Human FMO1 was expressed in *E. coli* JM109 cells in 2 L conical flasks containing 500 mL Terrific Broth in the presence of ampicillin (100 µg/mL) and riboflavin (50 mg/L) as described previously [126]. After expression, the protein was purified from the membrane fractions via DEAE anion-exchange and Ni-chelating Sepharose fast-flow affinity column, following the procedure, described previously [173]. The concentration and yield of obtained FMO1 protein were estimated by UV/Vis spectroscopy considering a 1:1 molar content of FAD. Protein purity was verified by separation and visualization in a 12% SDS polyacrylamide gel stained with Coomassie Blue. The activity of the purified FMO1 was determined by the methimazole assay described by Catucci and co-workers [174].

## In vitro metabolic assay

To estimate kinetic parameters for S-oxygenation of pesticides mediated by hFMO1, reactions were set up in a final volume of 200 µL in 50 mM potassium phosphate buffer pH 8.0 containing 0.5 µM enzyme, 0.5 mM NADPH and different concentrations of pesticide from 0 to 200 µM. The reaction was initiated by adding NADPH and incubated at 37 °C for 30 min. The reactions were terminated by adding 100 µL of ice-cold acetonitrile. After protein precipitation, the mixture was centrifuged at 12000 × *g* for 5 min and the supernatant was analyzed by HPLC to identify the metabolite(s) formed.

## High-Performance Liquid Chromatography

The separation and quantitation of the reaction mixtures were performed by using a calibration curve of analytical standards of substrates (phorate, methiocarb, fenthion) and products (phorate S-oxide, methiocarb S-oxide, fenthion S-oxide). The analysis was performed with an Agilent 1200 quaternary pump HPLC System equipped with a diode array UV detector (Agilent Technologies, USA) with a Kinetex 5 µm EVO C18 100Å column 250 × 4.6 mm. Pesticides and their metabolites were separated by gradient elution consisting of A – acetonitrile and B – 10 mM phosphoric acid as follows: A – 5%, B – 95% (0-2 min); A – 95%, B – 5% (18 min); 20 min: A – 95%, B – 5%; 23 min: A – 5%, B – 95%; 30 min: A – 5%, B – 95%. All metabolites were detected at a wavelength of 210 nm at a flow

rate of 1 mL/min. The retention time of pesticides and their metabolites were: phorate 17.2 min, phorate S-oxide 12.7 min; methiocarb 13.7 and 14.2 min (commercially obtained compound had two peaks), methiocarb S-oxide 8.3 min; fenthion 16.5 min, fenthion S-oxide 12.2 min.

## Preparation of DDAB functionalized graphene oxide (GO-DDAB)

For the preparation of DDAB-GO, 100 mM DDAB water solution with 1 mg/mL of GO dispersion was sonicated for 30 min to obtain a homogeneous dispersion. After this, the mixture was heated at 80 ºC for 1 hour to achieve the ionic functionalization of GO by cationic surfactant DDAB [175]. After cooling down the obtained mixture was used for electrode modification and FMO1 immobilization without any additional washing or preparation steps.

## Contact angle measurement

Contact angle data were obtained using Kruss Easy Drop DSA100 (Hamburg, Germany) and analyzed by the Drop Shape Analysis software. Silicon wafers were cleaned using isopropanol and placed in a sonicator bath for 10 minutes and then rinsed with Milli Q water. Initially, 20 µl of 1 mg/mL GO solution was placed on the wafer and after evaporation, the static contact angle was measured. In the second experiment, 20 µl of a solution DDAB-GO prepared as described above, was placed on the silicon wafer. Also in this case, after the sample had dried the static contact angle was measured with the following parameters: sessile water drop with constant drop volume, volume dispensed 10 µl, needle diameter 1 mm (thin), setting of Young Laplace equation for the data analysis. The data obtained are the mean of three independent experiments in which the value of the angle obtained is the mean of 10 acquisitions.

## Atomic force microscopy

AFM measurements were carried out in the intermittent contact mode using a 225 µm long super-sharp Si cantilever (Nanosensors, SSS-NCL), having a tip radius of approximately 5 nm, which was mounted on a Nanosurf Easyscan2 AFM instrument equipped with a high-resolution scan head (10 x 10 µm). The instrument, shielded in an insulated enclosure, was placed on an antivibration platform. Before analysis, 2 µl of GO sheets dispersed in water (final concentration 1 mg/mL), were dropped on a freshly cleaved mica support. The scan speed was 0.25 Hz with an image resolution of 256 × 256 pixels. Root-mean-square roughness ($R_{rms}$) was

determined by measuring only the top surface of the sheets. Height distribution diagrams and Abbott-Firestone curves were determined on a selected region of the AFM images.

## Electrode preparation

All electrodes, 3.0 mm working glassy carbon electrode (BASi, USA), were mechanically polished with PK-4 polishing kit before each experiment. The working glassy carbon electrodes were subsequently modified with 5 µL of 100 mM DDAB water solution [88] or 5 µL GO-DDAB. This was followed by the addition of 5 µL of purified hFMO1 (50 µM) onto the modified electrode surface and overnight incubation at 4 °C.

## Cyclic Voltammetry and pesticide titration

Electrochemical measurements of immobilized hFMO1 in DDAB and/or GO-DDAB modified electrodes were performed in a three-electrode standard electrochemical cell with C-2 low-volume sample chamber, 0.5 mm platinum coil auxiliary electrode and Ag/AgCl (3 M NaCl) reference electrode. The working electrolyte consisted of 50 mM potassium phosphate buffer pH 8.0 and 0.1 M KCl. Measurements were carried out using an Autolab PGSTAT12 controlled by Nova 2.1 software (Metrohm/Ecochemie, The Netherlands) at room temperature.

Cyclic voltammograms of hFMO1 were performed under anaerobic conditions in a glovebox (Belle Technologies, UK) with a nitrogen atmosphere. Scans were recorded from 0 to -750 mV with different scan rates from 20 to 120 mV/s.

For the titration experiments with different pesticides (increasing concentrations from 0 to 280 µM) the electrochemical response of the immobilized hFMO1 was measured after each addition of the pesticide. The electrochemical cell had a total volume of 500 µl with 50 mM potassium phosphate buffer pH 8.0 and 0.1 M KCl. After each addition the solution within the electrochemical cell was vigorously stirred for a couple of minutes to minimize mass transport effects and the cyclic voltammogram was recorded.

## Tandem chronoamperometry with immobilised hFMO1 and CYP3A4

For the tandem chronoamperometry experiments, CYP3A4 was heterologously expressed in *E. coli* for 48 h and purified using two chromatography steps as described previously [170,176]. The purified enzyme was subsequently immobilized on glassy carbon (GC) electrodes modified with poly (diallyldimethylammonium) (PDDA) polymer in a 1:1 mixture of PDDA: enzyme (25 µM) also described by our group [177].

The tandem chronoamperometry reactions, Figure 27, were carried out in the presence of oxygen with continuous stirring at 200 rpm to prevent the mass transport limitations and saturation of the reaction products near the surface of the working electrode, at the optimal reaction temperature of 37 °C. Cyclic voltammetry was carried out before and after each chronoamperometric experiment to estimate the stability of the bioelectrodes. The chronoamperometry measurements were carried out in 500 µl of 50 mM potassium phosphate buffer pH 8.0 and 0.1 M KCl at a set potential of -650 mV (vs. $Ag/AgCl_2$). Initially, the chronoamperometry was carried out with the immobilized FMO1 on GC-DDAB-GO in the presence of phorate (final concentration of 500 µM) in the 3-electrode electrochemical cell described above. After 30 min of the reaction at 37 ºC, the electrode with immobilized hFMO1 was replaced by a new GC electrode, this time with CYP3A4 immobilized. Before starting the second chronoamperometry experiment, a 100 µl sample of the electrochemical cell solution was taken for HPLC analysis. Again, the chronoamperometry experiment was carried out at the same potential bias for another 30 min at 37 ºC after which time a second sample was taken for HPLC separation and analysis.

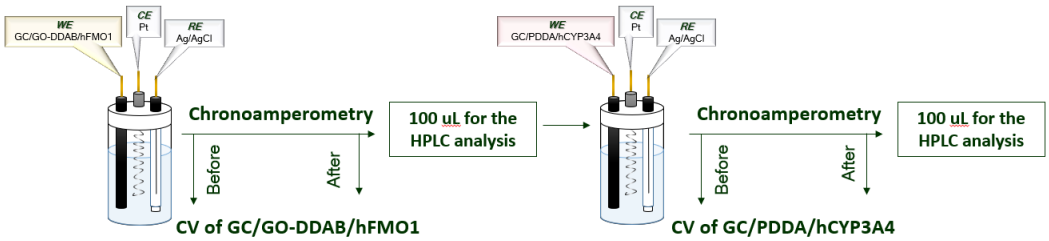


**Figure 27:** The principal scheme of tandem bio electrocatalysis reaction mediated by hFMO1 and CYP3A4

For the HPLC analyses, a 10 mM stock solution of phorate and its metabolites was prepared in the methanol and diluted to 100 µM in 0.1 M phosphate buffer

pH 7.4. Prior to HPLC analysis, the samples were further diluted 2:1 with acetonitrile. The HPLC analysis was performed with an Agilent 1200 quaternary pump HPLC System equipped with a diode array UV detector (Agilent Technologies, USA) with a Kinetex 5 µm EVO C18 100Å LC column 250 × 4.6 mm. Phorate and its metabolites were separated by gradient elution with the required post-analysis washing step. The mobile phase consisted of A – acetonitrile and B – 10 mM Phosphoric acid. Gradient profile was: 0-2 min: A – 5%, B – 95%; 20 min: A – 95%, B – 5%; 23 min: A – 5%, B – 95%; 30 min: A – 5%, B – 95%. All metabolites were detected at a wavelength of 210 nm at a flow rate of 1 mL/min. The retention times were: phorate – 17.2 min, phorate sulfoxide – 12.7 min, phorate sulfone – 14.3 min, phorate oxon sulfoxide – 9 min.

## 4.3. In vitro measurement of kinetic parameters for the conversion of selected pesticides by hFMO1

Human FMO1 was purified through two sequential chromatography steps as outlined in the methods section. It was then characterized by spectroscopy where the characteristic FAD cofactor absorbance maxima at 375 nm and 450 nm were observed. The spectrum was also used for the calculation of the yield of the expressed protein as well as the concentration of the protein for subsequent in vitro experiments.

Subsequently, the in vitro metabolism of carbamate and organophosphate pesticides mediated by hFMO1 was investigated using three compounds namely phorate, fenthion and methiocarb. The chemical structures of these pesticides and their corresponding oxygenated products are shown in Figure 28. Phorate is an organophosphate insecticide widely used in crops such as corn, potato, cotton, wheat and peanuts. Fenthion, another organophosphate insecticide has low solubility in water but is highly soluble in organic solvents. It is used in the post-harvest treatment of fruits and vegetables. It is moderately toxic to humans but highly toxic to birds. Both phorate and fenthion act via cholinesterase inhibition [178,179]. The third pesticide, methiocarb, is a carbamate insecticide. Due to its toxicity (also an acetylcholinesterase inhibitor), methiocarb approval as a plant protection product has been withdrawn by the EU effective 2020 [180].

The kinetic parameters $K_M$ and $V_{max}$, for each of the three pesticides were measured with purified hFMO1 as described in the methods section. For each pesticide, different concentrations were used with of hFMO1 and with the addition of NADPH. Reactions were carried out at 37 ºC for 30 min after which time the

product(s) was separated and analyzed by HPLC. Typical HPLC chromatograms obtained are shown in Figure 29. Phorate and its S-oxide have retention times of 17.2 and 12.7 min, fenthion and its S-oxide 16.5 and 12.2 min and methiocarb and its S-oxide 13.7, 14.2 and 8.3 min, respectively. As can be seen in Figure 29, methiocarb and to a lesser extent phorate and fenthion, were all actually present in two forms in the commercially obtained samples. However, in all cases hFMO1 is highly stereoselective only producing one product consistent with previous reports [45,181,182]. In the specific case of phorate, Hodgson and colleagues have previously shown that hFMO produces predominantly the (+) stereoisomer [181]. In this study, we did not embark on separating the isomers and used the commercially available standards to identify the sulfoxide.

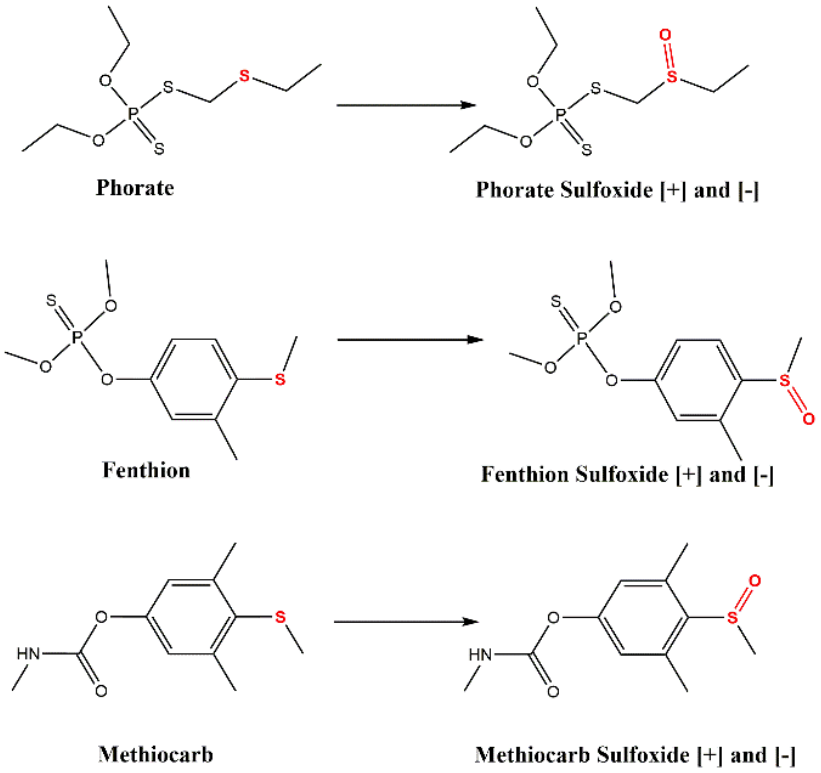


**Figure 28:** The chemical structures of the three investigated pesticides and their conversion to sulfoxides mediated by hFMO1.

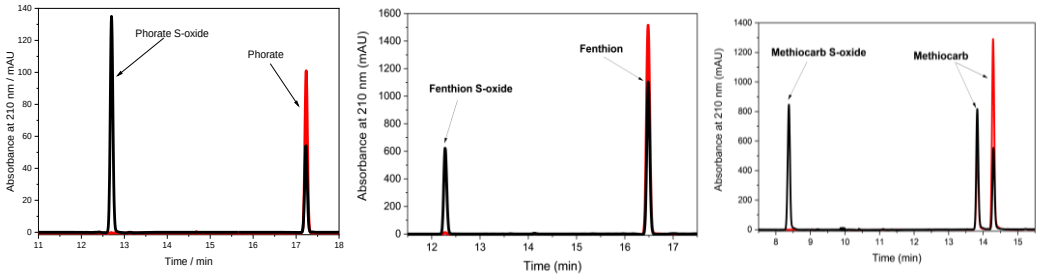


A B C

**Figure 29:** HPLC chromatograms of the separation of the *in vitro* sulfoxidation products obtained from the incubations of the three pesticides with hFMO1 (red line) and the respective control experiments in the absence (black line) of hFMO1. Reactions were carried out in a final volume of 200 µL in 50 mM potassium phosphate buffer pH 8.0 containing 0.5 µM enzyme, 0.5 mM NADPH and 200 µM of phorate **(A)**, fenthion **(B)** and methiocarb **(C)**.

The $K_M$ values calculated for the in vitro conversion of phorate, fenthion and methiocarb to their corresponding oxygenated products by purified hFMO1 were 93 ± 14 µM, 87 ± 36 µM and 98 ± 16 µM, respectively. Different $K_M$ values ranging from 30 to 340 µM have been reported previously [9,31,45] using human liver microsomes and these differences might be attributed to the source of the enzymes as well as the solubility of the pesticides used.

## 4.4. Immobilisation of hFMO1 on glassy carbon electrodes

The in vitro enzymatic assay of hFMO1 with the 3 pesticides was followed by the investigation of the same reactions but with the enzyme this time entrapped/immobilised on glassy carbon electrodes. To this end, the cationic surfactant DDAB, which we have successfully used for another human FMO, hFMO3 [109–111,183], was used with or without the addition of GO. The presence of GO and its interaction with the DDAB was investigated using different methodologies including UV/Vis spectroscopy, contact angle and AFM.

Initially, the functionalization of DDAB by GO was followed by UV/Vis spectroscopy and the data obtained are shown in Figure 30A. As can be seen in the figure, the main GO absorption peaks at 233 nm corresponding to π-π* transition of the C-C aromatic bonds, and 305 nm corresponding to n-π* transition of C=O bonds are totally lost in the GO-DDAB spectrum [184]. Since the GO fingerprints are completely absent in the DDAB-GO spectrum this implies not only that GO is attached to the DDAB but also its surface is entirely covered by DDAB.


A B C

**Figure 30: (A)** UV/Vis absorbance spectra of modified GO by cationic surfactant DDAB. **(B)** Contact angles of water droplets on the surface of GO and **(C)** GO-DDAB deposited films. The red bars demonstrate the changes in the angles measured.

The hydrophilicity of the GO-DDAB was analysed by contact angle measurements and compared to the GO water suspension. This methodology allows for the quantitative measurement based on intermolecular interactions between the surface already functionalized by GO or GO-DDAB and a small drop of water in contact with it. It is mainly used for assessing the wettability of a surface but here it was used to determine any changes regarding the hydrophobicity of the GO-DDAB. The contact angle results are shown in Figure 30B-C. As can be seen in the figure, the GO water suspension as expected is hydrophilic in character and thus results in very low water contact angle i.e. 8.0° ± 0.71. On the other hand, the addition of the DDAB causes an increase in the hydrophobicity of the resulting GO-DDAB layer and therefore water contact angle of 46° ± 0.19 is observed. This value is in line with data published previously [175]. The observed increase in hydrophobicity is advantageous for the immobilisation of hFMO1 since this protein, similar to hFMO3, has a predicted hydrophobic group of amino acids at its C-terminal which anchor it to the ER membrane [30]. The latter being the reason behind purifying this protein from membrane fractions and not the *E. coli* cytosol.

## 4.5. Atomic Force Microscopy (AFM)

The surface properties of GO and of DDAB-grafted GO sheets were investigated by means of AFM. Morphological signals, height profiles along selected lines, and height distributions are shown in Figure 31, respectively. In Figure 31A, a few GO sheets are AFM imaged. From this figure it is clear that the majority of the sheets had lateral sizes in the 0.5-1 μm range, but smaller sheets were also present. The root-mean-square average of the profile height deviations from the mean line value ($R_{rms}$) [185] of the top surface of GO sheets was calculated

to be 249 pm. The height profiles of about 1 and 2 ± 0.1 nm measured along two selected lines (Figure 31B) are typically observed for single-layered (1L) and bilayered (2L) GO sheets, respectively. The height distributions of a region selected in Figure 31A (red histogram in Figure 31C) revealed three peaks with Gaussian profiles with maxima spaced of 0.9 ± 0.05 nm. Such peaks can be safely assigned to the atop height of the mica support, 1L- and 2L-GO sheet thicknesses, respectively. A surface statistical approach was then performed by processing the cumulative distribution function of the surface heights (known as Abbott-Firestone curve or bearing curve) [186].

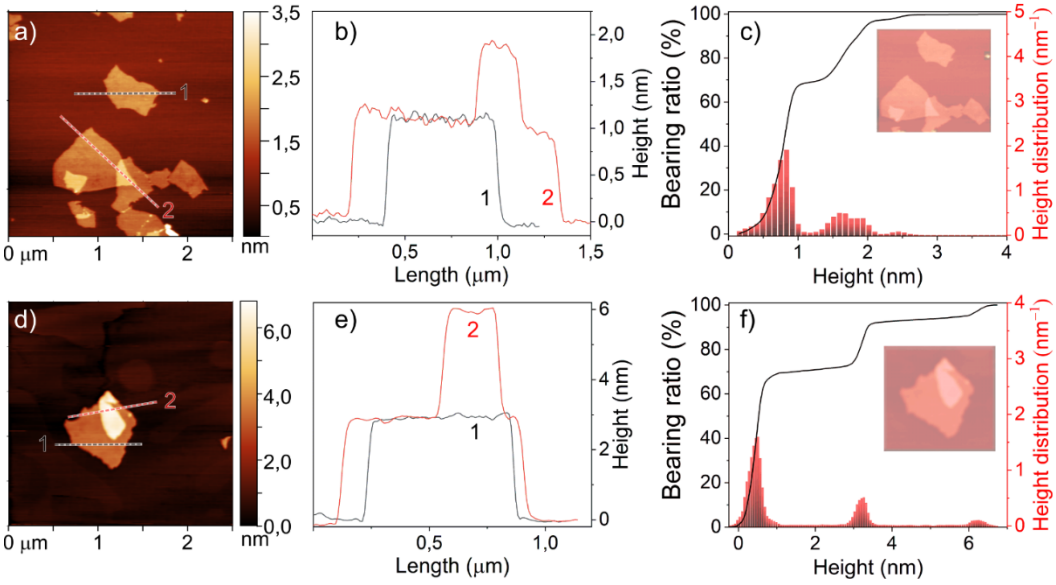


**Figure 31: (A)** AFM image of GO sheets deposited on the mica support, **(B)** related height profiles along two selected lines, **(C)** height distribution (red histogram) and Abbott-Firestone curve (black line) of a selected region in **(A)**; **(D)** AFM image of DDAB- grafted GO sheets deposited on the mica support, **(E)** related height profiles along two selected lines, **(F)** height distribution (red histogram) and Abbott-Firestone curve (black line) of a selected region in **(D)**.

As shown in Figure 31C (black curve), the cumulative curve of heights showed a distinctive profile with three roughly vertical steps in the 0.4-1.0 ± 0.1 nm interval for ~66% of the bearing area, a second increment in the 1.3-2.0 ± 0.1 nm corresponding to the ca. 95% of the surface, and a third and smaller increment of 2.3-2.7 ± 0.1 nm corresponding to ca. 99.8% of the bearing area. In summary, these bearing area values are representative of the predominance of 1L-GO in comparison with 2L-GO sheets, and a quasi-negligible contribution of multi-layered GO sheets can be highlighted (1L-GO > 2L-GO >> multi-layered- GO sheets).

In Figure 31D, two DDAB-functionalized GO sheets are AFM imaged. In this figure the sheets with lateral sizes in the 0.3-0.5 and 1 μm range are shown. Height profiles of about 2.9 and of 6.0 ±0.1 nm was measured along two selected lines shown in Figure 31D. Such heights could correspond to multi-layered GO and/or DDAB fully covering the GO sheets. However, from the comparison between $R_{rms}$ value of GO sheets (GO $R_{rms}$ = 249 pm) with the same value of DDAB-GO sheets (DDAB-GO $R_{rms}$ = 1.26 nm) an increase of the $R_{rms}$ of one order of magnitude is observed. Such increase in $R_{rms}$ could be associated with the DDAB layer forming a rougher surface on the sheets, as also previously reported for Au surfaces modified with benzenethiol derivatives [187]. The height distributions of a region selected in Figure 31D (red histogram in Figure 31E) revealed three peaks with Gaussian profiles with maxima spaced of 2.75 ± 0.1 nm. Such peaks can be safely assigned to the atop heights of the mica support and of DDAB-functionalized-GO sheets of different stacking order, respectively. The Abbott-Firestone curve or is shown in Figure 31F (black curve), the cumulative curve of heights showed a distinctive profile with three vertical steps in the 0.1-0.8 ± 0.1 nm interval with ~67% of the bearing area, a second increment in the 2.9-3.4 ± 0.1 nm corresponding to the ca. 91.5% of the surface, and a third smaller increment of 6.0-6.6 ± 0.1 nm corresponding to ca. 99.5% of the bearing area. In summary, these GO bearing area ranges are representative of a rougher surface after the functionalization with DDAB.

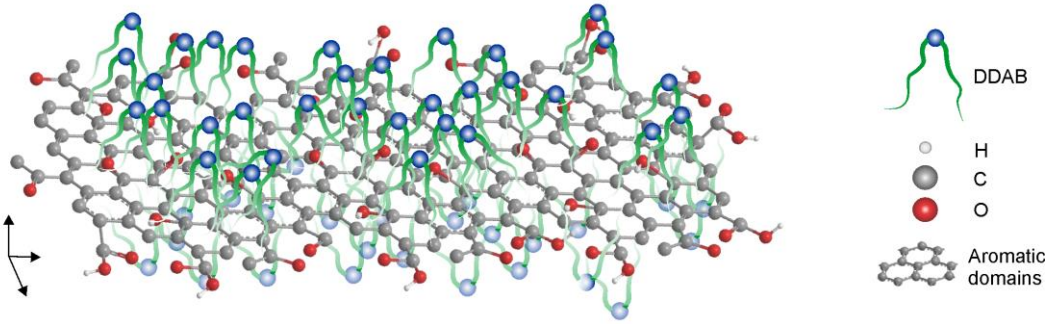


**Figure 32:** The structure model of DDAB-GO

In conclusion, based on UV-Vis spectra, contact angle and AFM measurements, a structure model of DDAB-GO system can be schematized (Figure 32). In this figure, GO with oxygen-containing groups (-COOH, -OH, >C=O) located at the edges and epoxy groups on the basal planes of the GO structural unit is shown, thus behaving as an amphiphilic system with hydrophobic basal planes and hydrophilic edges [188]. The GO amphiphilic nature takes place

at pH =< 7 with -COOH protonated species or pH > 8-9 with the carboxylate anions (–COO-), respectively [189,190]. From this structure model it is clear that, due to the interaction of DDAB with GO sheets on the basal planes with the Br ions far away and the long aliphatic chains facing GO sheets, an effective decoration of the GO sheet is observed. Such DDAB-decorated GO system appears about 3 nm thick in line with the AFM data.

## 4.6. Electrochemical behaviour of immobilized hFMO1

Characterization of redox properties of immobilized hFMO1 on modified GCE was performed by cyclic voltammetry under anaerobic conditions to prevent spontaneous regeneration of enzyme-bound FAD cofactor to its oxidized form. Measurements were performed on both DDAB and GO-DDAB modified electrodes (Figure 33) and the results obtained are summarized in Table 10. As expected in the control experiments, electrodes without immobilized enzyme, no redox peaks were observed .

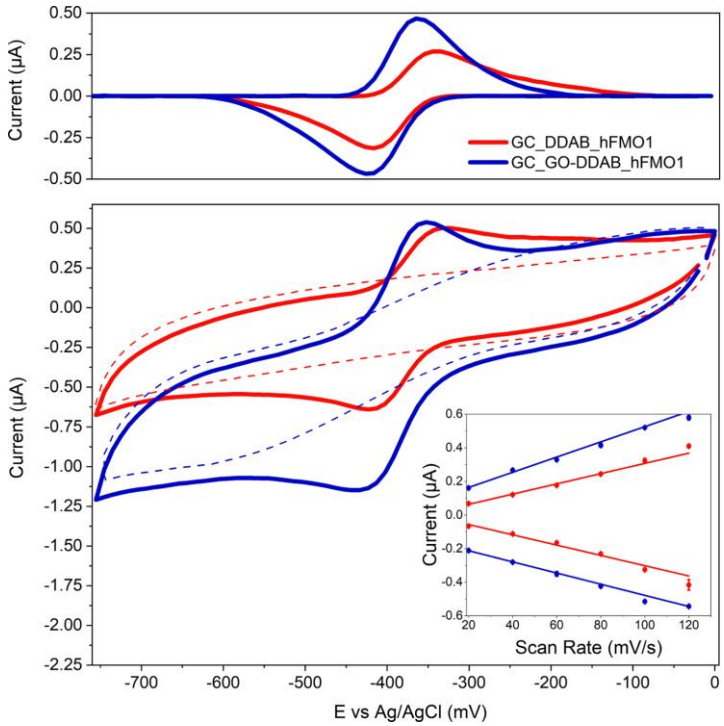


**Figure 33**: Cyclic voltammograms of hFMO1 immobilized on GC electrodes modified by DDAB in the presence (blue line) and absence (red line) of GO at scan rate of 100 mV/sec. The corresponding control cyclic voltammograms of GC electrodes modified with DDAB (dashed red) and DDAB-GO (dashed blue) are also shown. Bottom panel are original cyclic voltammogram with the linear dependence of current versus scan rate shown in the insert. Cyclic voltammograms in the top panel are baseline corrected.

**Table 10:** Redox properties of immobilized hFMO1 on modified electrodes #.

| **Electrode** | **$E_{Ox}$ (mV)** | **$E_{Red}$ (mV)** | **$\Delta E$ (mV)** | **$E_{1/2}$ (mV)** |
|---|---|---|---|---|
| GC-DDAB-hFMO1 | -346 ± 6 | -412 ± 2 | 66 ± 7 | -379 ± 3 |
| GC-GO-DDAB-hFMO1 | -364 ± 2 | -425 ± 1 | 61 ± 2 | -395 ± 2 |

# Data obtained from cyclic voltammograms of hFMO1 under anaerobic conditions in a glovebox at room temperature. Scans were recorded from 0 to - 750 mV with different scan rates from 20 to 120 mV/s in 50 mM phosphate buffer pH 8.0 and 0.1 M KCl.

Electrochemical reduction and oxidation process of immobilized hFMO1 demonstrated a reversible behaviour in both presence and absence of GO. The linear dependence of increasing current as a function of scan rate (up to 120 mV/s) shown in Figure 33 inset, is indicative of a thin-film confined electroactive species that are not under diffusion control as stated by Laviron's theory [191]. Midpoint potentials of the immobilised hFMO1 were -379 ± 3 and -395 ± 2 mV in the absence and presence of GO, respectively. Similar midpoint potentials were observed with hFMO3 immobilised on GC electrodes modified with DDAB [110]. Since the presence of GO resulted in higher observed currents, the number of electroactive species in the absence and presence of the GO were determined using the Laviron equation [191] by integration of the reduction peaks of the cyclic voltammograms. The surface coverage on GC-DDAB and GC-DDAB-GO were calculated to be 7.0 $\times 10^{12}$ and 1.3 $\times 10^{13}$ molecules/cm$^2$, respectively.

## 4.7. Voltammetric titration of pesticides

The efficiency of modified GC/GO-DDAB/hFMO1 in the conversion of the three pesticides was investigated and the kinetic parameters determined. The electrode response was recorded in the presence of increasing pesticide concentration. Control measurements were carried out in the absence of immobilized protein (data not shown). The proportional increase of cathodic peak current simultaneously with pesticides concentration corresponds to enzyme catalytic activity of substrate oxygenation by using molecular oxygen dissolved in buffer, reducing equivalent and electrons from the electrode.

Human FMO1 immobilised on electrode and the resulting response to titration with increasing concentrations of each of the three pesticides, methiocarb, fenthion and phorate was followed by cyclic voltammetry. The obtained increases in the cathodic peak current upon addition of the pesticides was subsequently plotted against the known concentration of each pesticide in order to calculate the relevant kinetic parameters of hFMO1 modified electrodes by fitting the data to the Michaelis-Menten equation (Figure 34). The calculated $K_M$ values for fenthion,

methiocarb and phorate were 29.5 ± 5.1 µM, 38.4 ± 7.5 µM, 29.6 ± 4.1 µM, respectively.

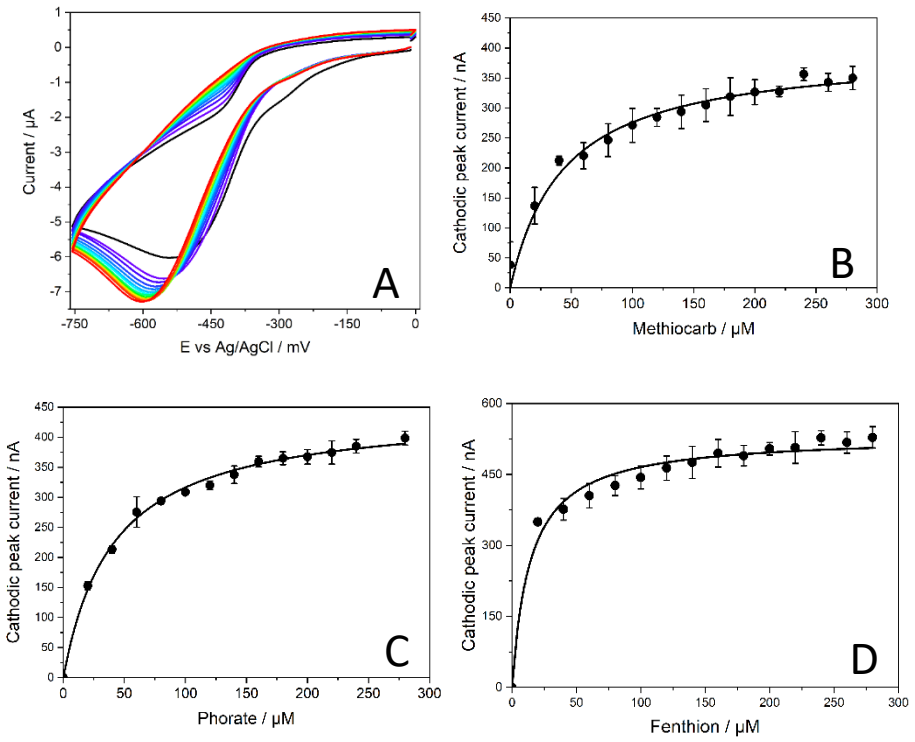


**Figure 7:** Typical cyclic voltammograms of hFMO1 immobilised on glassy carbon electrode modified with GO-DDAB titration with increasing pesticide concentrations from 0 µM (black line) to 280 µM (red line) in the presence of oxygen **(A)**. Normalized catalytic current values as a function of the concentration of the pesticide added: methiocarb **(B)**, phorate **(C)** and fenthion **(D)** fitted to the Michaelis-Menten equation. Estimated standard errors of three different electrode measurements are represented as error bars.

Kinetic values obtained for the conversion of the pesticides by the immobilized hFMO1 were compared to the *in vitro* data from the present work as well as previously published data [9,31,45,181,182]. In general, the $K_M$ values are within the same order of magnitude although for fenthion the values show larger variations. More studies need to be carried out to clarify the reasons behind these differences but one parameter could be the source and preparation of the enzyme as well as the assay conditions.

## 4.8. Bioelectrochemical tandem reactions of hFMO1 and Cytochrome P450 3A4 with phorate

Previously, Levi and Hodgson [181] have shown the conversion of phorate to different oxidation products with FMO and cytochrome P450s, a summary of which is shown in Figure 35. According to the latter researchers [181] hFMO1 is able to convert phorate (1) exclusively to phorate sulfoxide (2), whereas cytochrome P450 can potentially transform it to other additional oxidation products including phoratoxon sulfone (3) (via the intermediate phorate sulfone) and phoratoxon sulfoxide (6) (Figure 35).

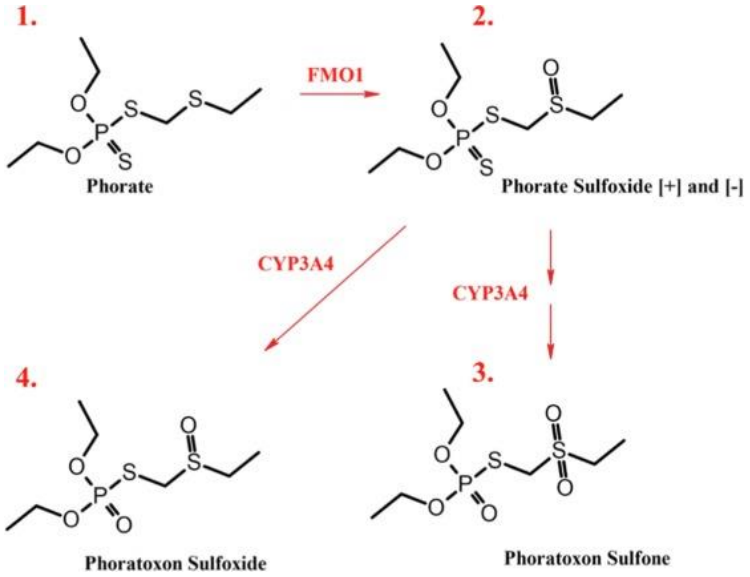


**Figure 35:** Scheme of FMO and CYP reactions involved in phorate oxidation **[181]**.

Therefore, we investigated the possibility of performing an electrochemically-driven tandem reaction exploiting two immobilized enzymes on different electrodes working on a single reaction mixture. Initially, phorate was added to hFMO1 immobilized on DDAB-GO glassy carbon electrode and chronoamperometry was carried out for 30 min by applying a potential bias of -650 mV in the presence of oxygen. An aliquot of the reaction was then withdrawn from the mixture and HPLC separation revealed the expected phorate sulfoxide product (2) as shown in Figure 36. The same reaction mixture was then further subjected to electrocatalysis using a cytochrome P450, human hepatic CYP3A4 immobilized on glassy carbon electrode modified with PDDA (refer to methods section for details). CYP3A4 has been previously shown to carry out the different oxidation steps of phorate metabolism [45] although the main cytochrome P450 indicated in phorate

transformation is 2C9 [45]. The reaction with immobilised CYP3A4 was carried out for a further 30 min as before. The HPLC separation in this case shows that the addition of this second step leads to the formation of two extra products: phoratoxon sulfone (3) and phoratoxon sulfoxide (4). Phoratoxon sulfone was not available as a pure standard therefore we inferred its presence from a previously published HPLC separation containing the same analytes [181]. As expected the amount of phorate sulfoxide (2) in the tandem reaction is increased due to the fact that CYP3A4 can also perform the same S-oxygenation reaction carried out by FMO1 but at a lower rate [45] (Figure 36). Nevertheless, CYP3A4 does not seem to form phorate sulfone or phoratoxon that could be postulated as intermediate products on the route leading to phoratoxon sulfone (3) and phoratoxon sulfoxide (4), respectively as shown in Figure 37B. For this reason, a reaction with only CYP3A4 using phorate as substrate was also carried out (Figure 37A). In this case, phorate sulfoxide (2) and phoratoxon sulfone (3) were detected confirming that only the tandem reaction leads to the formation of phoratoxon sulfoxide (4) and that no observable intermediate product is formed in the CYP3A4 mediated transformation.

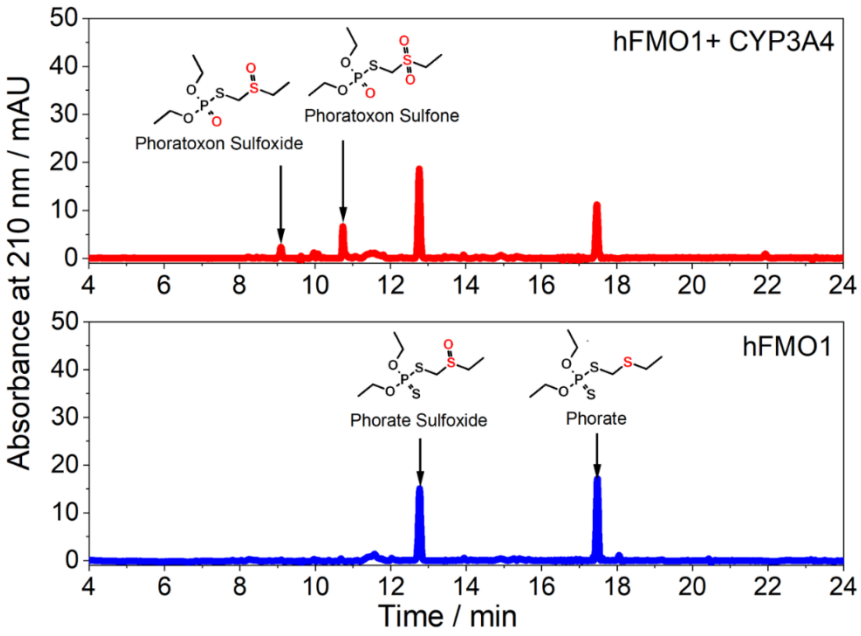


**Figure 36:** HPLC separations of the products of electrochemically driven reactions of hFMO1 (bottom, blue trace) and hFMO1 in tandem with CYP3A4 (top, red trace) with organophosphate pesticide phorate. Each sample contained 500 µM of phorate in 0.1 M phosphate buffer pH 7.4 with 0.1 M KCl as supporting electrolyte. The two enzymes were immobilized on glassy carbon electrodes as described within the text. Retention times are: phorate 17.2 min, phorate sulfoxide 12.7 min, phoratoxon sulfone 10.8 min and phoratoxon sulfoxide 9.0 min.

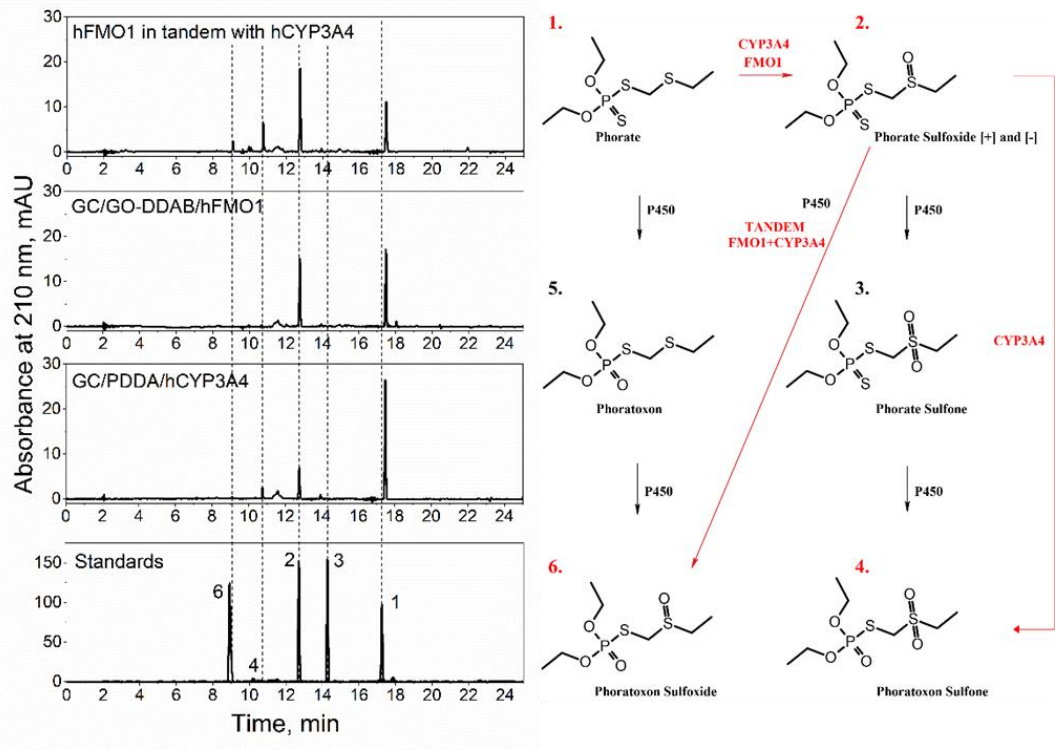


**Figure 37:** Phorate tandem reactions. **(A)** HPLC separations of electrochemically driven reactions and standards. Each sample contained 500 µM of phorate as a substrate in 0.1 M phosphate buffer pH 7.4 with 0.1 M KCl as supporting electrolyte. **(B)** Scheme of the reactions involved in phorate metabolism. Black arrows indicate postulated reactions from previously reported CYP activity **[181]**. Red arrows indicate reactions that were observed in this work and that are catalyzed by FMO1 or CYP3A4 including the tandem reaction.

Xenobiotic metabolism is a complex process involving different enzymes often acting in sequence. It would be particularly interesting to have an in vitro platform able to mimic this complex process. As a step in this direction the data presented in this paper demonstrates the feasibility of using bioelectrodes with separately immobilised hFMO1 and CYP3A4, successfully carrying out their tandem reactions in the conversion of phorate, an organophosphate pesticide. These bioelectrochemical conversions not only lead to the single phorate sulfoxide product of hFMO1 but also the phoratoxon sulfoxide, the tandem enzymatic product of FMO1 followed by CYP3A4. These preliminary data are encouraging and lead the way to construct microfluidic systems which go beyond the single enzyme cell [192], by using several enzymes immobilised in a sequential format representing the detoxification pathways of xenobiotics within the human body.

# Chapter 5

# Green production of indigo and indirubin by an engineered Baeyer–Villiger monooxygenase (and hFMO1)

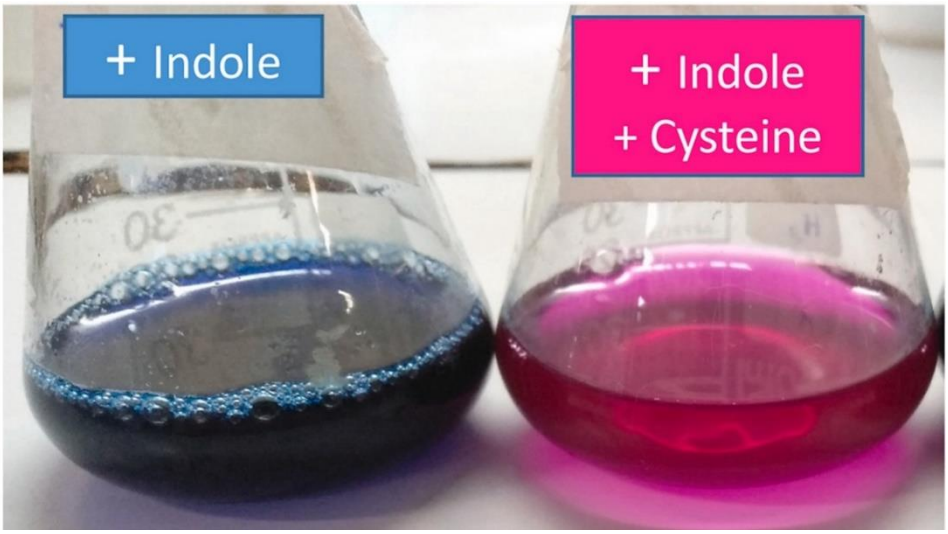


This work has been published:

Catucci G., Turella S., **Cheropkina H.**, De Angelis M., Gilardi G., Sadeghi S. J. (2022) Green production of indigo and indirubin by an engineered Baeyer–Villiger monooxygenase

DOI: https://doi.org/10.1016/j.bcab.2022.102458

# 5.1. Introduction

Indigoids are a large class of molecules with a wide range of applications in different industries including textiles [193–195]. The industrial use of indigoids as dyes is well known and previously described in literature [196,197]. These molecules derive from the indole scaffold, which consists of a benzene ring fused to a pyrrole ring. Indigo is a blue-colored molecule that gives the name to this class of dyes and is one of the oldest and most widely used dyes by mankind [198]. Indigo blue has been historically extracted from Indigofera tinctoria that can be exploited for the production of indigo due to the presence of indican (indolyl-β-d-glucopyranoside), an l-tryptophan derivate and indigotin (chemical responsible for blue color of indigo) through saccharification and oxidation reactions [194,199,200]. In 1897 BASF established an industrial process to produce indigo from aniline, which is still to date the basis for the process used for the production of indigo [194]. Nevertheless, this process involves harsh and environmentally harmful reaction conditions such as 200 °C and the use of NaOH [198].

Indigo is employed as a dye for cotton fibers and since this molecule is insoluble in water, in order to be used, it must be first converted to its water-soluble form, leuco-indigo, via sodium dithionite ($Na_2S_2O_4$) reduction and spontaneous re-oxidation for the formation of the dimer [201]. Several different strategies have been developed to overcome the use of strong reducing agents which can be a source of pollution downstream of these staining processes [196,202]. In line with new environmental regulations and green policies, the interest to produce indigo by enzymatic reactions and bio-based processes is growing, also considering the fact that the by-products of the chemical industrial process are toxic compounds. To this end, the use of microorganisms to produce indigoids from low-cost carbon sources is currently being explored as an environmentally friendly alternative route. These microorganisms can be exploited due to the presence of specific enzymes involved in the synthesis of indigoids such as: naphthalene dioxygenase [203–211], flavin-containing monooxygenase (FMO) [212–216], and cytochrome P450 [217–220]. These enzymes catalyze the hydroxylation of the indole molecule leading to the production of intermediates which upon dimerizing, result in the formation of indigo or its derivatives.

Another derivative of indole is indirubin which is a purplish-red bisindole alkaloid and is the major active component of Traditional Chinese Medicine herbal formulas (Dang Gui Long Hui Wan and Qing-Dai) that contain *Isatis tinctoria* L and *Indigofera tinctoria* L [221]. For some years now, indirubin and its analogues

have been shown to exhibit different biological properties including anticancer [221] as well as anti-inflammatory [222]. In the specific case of cancer, indirubins have been shown to inhibit DNA synthesis, protein kinases as well as cyclin-dependent kinases thus acting as promising candidates to prevent tumor cell growth so much so that indirubin-based small molecules in cancer treatment have become a highly researched area [223].

As mentioned above, in order to overcome the drawbacks of chemical synthesis of these indigoids, in this work we have employed a Baeyer-Villiger monooxygenase from Acinetobacter Radioresistens S13 (Ar-BVMO) for the enzymatic conversion of indole into indigo or indirubin in transformed *E. coli* cells. To achieve this goal the Ar-BVMO protein was expressed and purified [224,225] and its stability and activity compared to an active site mutant, R292A, that has been previously partially characterized in our laboratory [226]. Both wild type and mutant enzymes were evaluated for their stability as biocatalysts by differential scanning calorimetry (DSC). The activity of the purified enzymes towards indole as a possible substrate was determined. Since only the R292A mutant demonstrated a significant activity with indole, all subsequent studies were performed with this mutant. Given the high cost of the NADPH cofactor, the optimization of the reaction conditions for the production of the two indigoids was performed in an *E. coli* whole-cell system overexpressing the Ar-BVMO mutant with a NADPH-regeneration system. Moreover, in previous studies flavin-containing monooxygenases have been mainly used for indigo production but we aimed at using this biocatalyst for indirubin production exploring the cysteine "switch" described by Han and colleagues [227].

The second aim of the current study was to investigate the role of hFMO1 in the oxidation of indole. In the human body, it is known that the indole can be metabolized by hP450 enzymes [228] and cause the formation of the indoxyl sulfate, uremic endotheliotoxin that plays a significant role in the progression of chronic kidney disease and cardiovascular diseases [229,230]. The impact of the activity/inactivity of hFMO1 on the formation of indoxyl sulfate has not been demonstrated yet. Previously was only shown that the indole able to modulate the FMO3 expression [23] and cause an inhibition effect on the enzyme [231,232]. But as was already shown in previous chapters the behavior of hFMO1 and hFMO3 are different and the real role of the renal representative of the class is not totally studied nowadays.

## 5.2. Materials and methods

### Reagents

Acetonitrile, ampicillin, cysteine, dimethyl sulfoxide (DMSO), 5,5′-dithiobis-(2-nitrobenzoic acid) (DTNB), dithiothreitol (DTT), IGEPAL, indirubin, indole, isopropyl-beta-d-thiogalactopyranoside (IPTG), lysozyme from chicken egg white, β-mercaptoethanol, methanol, β-nicotinamide adenine dinucleotide reduced form (NADH), β-nicotinamide adenine dinucleotide 2′-phosphate reduced form (NADPH), β-nicotinamide adenine dinucleotide phosphate ($NADP^+$), phosphoric acid, protease inhibitor phenylmethylsylfonyl fluoride (PMSF), riboflavin, trisodium citrate were purchased from Sigma Aldrich (Italy). Glycerol, imidazole, indigo, tryptone and yeast extract were purchased from Thermo Fisher Scientific (Italy). All other reagents and buffer components were of the highest grade commercially available.

### Expression, and purification of wild type and mutant BVMO

The expression of both proteins was performed according to the previously published methodology [224] with minor modifications. Expression was carried out for 20 h at 24 °C and 180 rpm in presence of riboflavin. At the end of the expression, cells were harvested by centrifugation at 4000 rpm at 4 °C for 20 min and washed with 50 mM KPi buffer pH 7.4. Resuspended cells were sonicated for 12 min with 30 s of sonication and 1 min of pause between each sonication. After sonication, 1% v/v of IGEPAL was added and the solution was left to stir for another 30 min at 4 °C. The solution was subsequently ultracentrifuged at 42,000 rpm at 4 °C for 30 min with Beckman Optima L-90K Ultracentrifuge. The pellet was discarded and the supernatant was loaded onto the 5 mL HisTrap™ Fast Flow column. Bound protein was eluted by addition of 500 mM imidazole. Eluted fractions containing the typical flavin absorbance at 450 nm were pooled, concentrated and buffer exchanged using Millipore Amicon 30,000 MWCO. Purified proteins were stored at −80 °C.

### Screening for indigo production and calculation of steady state parameters

The screening assay for indigo production was performed by monitoring the increase in absorbance at 620 nm. Reaction conditions were: 8.6 μM Ar-BVMO, 800 μM NADPH in 50 mM Tris HCl pH 8.5, at 30 °C for 240 s.

The steady state kinetic parameters for indole were determined spectrophotometrically by monitoring the NADPH consumption rates (AU/s) at 340 nm using 0–20 mM indole. The samples were evaluated in a total volume of 0.5 mL containing 1 μM enzyme and 160 μM of NADPH. Reactions were followed for 200 s at 30 °C in 50 mM Tris HCl, pH 8.5.

## Thermal stability measured by DSC analysis

For DSC analysis a Microcal VP-Capillary system from Marlvern analytical was used with the method previously described [126]. The samples were placed in a 200 μL sample cell against a 200 μL reference cell that was filled with buffer: 50 mM KPi pH 7.4. Equilibration was allowed for 10 min at 25 °C before increasing the temperature to 90 °C at a scan rate of 90 °C/h. Cells were equilibrated with buffer for 10 cycles before starting each experiment to allow optimal thermal history.

## Evaluation of optimum pH and cysteine concentration for indigoids production

To evaluate the optimal pH and cysteine concentration for indigo or indirubin production, reactions were set up in a microtiter plate (NUNC96-well).

- *For Ar-BVMO:*

0.1 M Tris-HCl (pH range 7.0 – 9.0) with 0.5 μM Ar-BVMO R292A, 5 mM NADPH, 5 mM indole, and 0 – 20 mM l-cysteine.

- *For hFMO1:*

0.1 M Tris/HCl buffer (pH: 7, 7.4, 8, 8.2, 8.5, 8.8, 9) or 0.1 KPi buffer (pH: 5.8, 6, 6.2, 6.4, 6.6, 6.8, 7.0, 7.2, 7.4, 7.6, 7.8, 8), with 0.5 μM hFMO1, 0.5 mM of NADPH/NADH, 1 mM of indole and l-cysteine (0, 0.5, 1, 2.5, 5, 10, 25 mM).

The reactions were carried out in a total volume of 200 μL for 48 h at 25 °C and 200 rpm. Reactions were dried in the oven at 55 °C and after evaporation the remaining indigo or indirubin powder was resuspended in DMSO. The absorbance of indigo was monitored at 620 nm, whereas the absorbance of indirubin was monitored at 540 nm [227] using SPECTROstar Nano (BMG LABTECH).

## Detection of 3-hydroxindole intermediate by fluorescence spectroscopy

3-hydroxindole is produced as an intermediate in the conversion of indole by Ar-BVMO biocatalyst. This hydroxylated compound can be detected by fluorescence: excitation at 365 nm with the resulting fluorescence emission at 470 nm [227], using LS-55 Fluorescence Spectrometer (PerkinElmerR). The reaction mixtures prepared in 0.1 M Tris-HCl pH 8.0 in a final volume of 150 µL contained the following: 0.5 µM BVMO mutant, 0.1 mM NADPH, 12.5 mM indole with 10 mM cysteine. Control experiments were carried out in the absence of any cysteine supplementation.

## *E. coli* whole-cell reactions and quantification of indigo and indirubin

Pellets of *E. coli* BL21 cells transformed with the expression vector pT7-BVMO [224,233], or JM109 with the pJL2-hFMO1 vector, with an optical density of 10, were resuspended in 0.1 M Tris-HCl buffer pH 8.5. Reactions in a total volume of 1 mL were carried out for 72 h at 25 °C and 37 °C (only for hFMO1) and 200 rpm. As NADPH cofactor regeneration system $NADP^+$ (0.3 mM final concentration), trisodium citrate (50 mM final concentration) and $MgCl_2$ (10 mM final concentration) were used [234]. Citrate in combination with $MgCl_2$ has been previously shown to sustain the activity of monooxygenases both FMO as well as cytochrome P450 enzymes [235,236]. To investigate the influence of cofactor on the indole conversion by hFMO1the whole cell reaction was carried out also in the presence or absence of 0.3 mM NADPH/NADH and 0.125 – 12.5 mM of l-cysteine.

To initiate the reactions, 5 mM (for Ar-BVMO) and 0.25 – 25 mM (for hFMO1) indole as substrate was added. Samples were withdrawn from the reaction mixture at 15, 24, 48 and 72 h in triplicates and analyzed.

- *For Ar-BVMO:*

At each of these time points, the withdrawn samples were centrifuged at 10,000 g for 10 min, the resulting supernatants were discarded, and the remaining pellets resuspended in 500 µL of pure DMSO to extract the indigoids within the cells. Pellets resuspended in DMSO were sonicated for 10 min in a water bath, then placed for 10 min at 55 °C and centrifuged again 10 min at 10,000 g. If any colored powders were still visible within the cell pellets, the procedure was repeated until

complete extraction was achieved. Upon complete extraction 400 µL were taken and stored at −20 °C.

- *For hFMO1:*

At each of these time points, the withdrawn samples were centrifuged at 10,000 g for 10 min, the resulting supernatants were discarded. The products of the reactions due to their low solubility in water-based environment were extracted before quantification by UV/Vis. The extraction was done by using the three-phase liquid extraction briefly:

1. The chloroform : methanol solution (CM solution) for the extraction was prepared in the ratio 2 : 1 respectively.
2. To 1 mL of reaction mixture the 1.5 mL of CM solution was added.
3. To improve phase separation between the water and organic phases 100 µL of 5 M NaCl was added.
4. Obtained mixture was vortexed 1 min and centrifuged at 10000 × *g* for 1 min to reach total separation of the phases.
5. The chloroform phase contained products of the reaction, coloured solution, was isolated and the chloroform evaporated. After isolation the solutions were protected from the exposure to light due to indigo sensitivity.
6. After the chloroform evaporation the obtained powder was dissolved in 100 µL of DMSO.
7. The samples were stored at -20 °C protected from the light.

The concentration of indigo and indirubin within the extracted samples were measured using the peak absorbance at 620 nm and 540 nm, respectively [227].

## HPLC analysis of indigo and indirubin produced by purified enzyme or *E. coli* whole-cells

Calibration curves were prepared for both indigo and indirubin by dissolving the purchased commercial standards in pure DMSO at different concentrations: 0 µM, 10 µM, 20 µM, 30 µM, 40 µM, 50 µM, 60 µM, 70 µM, 80 µM, 90 µM, 100 µM. The samples were analyzed using Agilent 1200 Series Gradient HPLC System with a 4.6 × 250 mm Kinetex® 5 µm EVO C18 100 Å column. The mobile phase was run at a flow rate of 1 mL/min and was composed of acetonitrile (solvent A), methanol (solvent B) and 1% $H_3PO_4$ (solvent C). The following gradient was applied: 0–5 min, 20% A and 80% C, 5–6 min, 40% A, 20% B and 40% C; 6–15

min, 60% A, 20% B and 20% C; 15–16 min, 20% A and 80% C; 15–20 min, 20% A and 80% C.

The same protocol was used for analysis of reactions both with whole-cell and pure protein that were stored at -20 ℃. Initially, the samples were thawed at room temperature and heated at 95 ℃ for 5 min. Subsequently, the samples were centrifuged at 10,000 g for 10 min and the clarified supernatant was used for HPLC analyses. Indigo and indirubin were quantified using the absorbance at 620 nm and 540 nm, respectively [227].

## TLC analysis of indigoids produced by *E. coli* whole-cells

Silica gel TLC was used to analyze the indigoids produced from the *E. coli* whole-cell reactions. The samples were evaporated to concentrate the indigoids and then repeatedly spotted on the TLC. The mixture of acetone and chloroform (50:50) was used as the mobile phase. The solution was poured into the chamber followed by 10 min of equilibration. The TLC plate was loaded and removed when the mobile phase almost reached the end of the plate.

## In silico molecular docking studies

Ligand and protein structures were prepared using the YASARA structure package [237]. YASARA, version 21.12.19, has all the functions embedded useful to predict and validate macromolecular structures, including ligand docking and highly accurate force fields with knowledge-based potentials. AMBER 03 force field was employed throughout all simulations. The 3D homology models of wild type and mutant Ar-BVMO were built by YASARA software [237] using the cyclohexanone monooxygenase crystal structure (PDB ID:5M0Z) as the template structure [238]. 999 runs of docking on WT and R292A Ar-BVMO were carried out according to a previously published methodology [126,239] with minor modifications using the Autodock program embedded in YASARA. During the docking experiment, indole is originally outside the simulation cell and is placed inside the cell by exploiting the Autodock Lamarckian Genetic algorithm, yielding different binding modes classified by the binding energy outputs. YASARA classifies the results of the docking ordering the protein-ligand complexes on the basis of the binding energy (where positive energies indicate stronger binding and negative energies equate to no binding). After docking the results are sorted by binding energy and 3 different poses displaying positive binding energies were

obtained for WT and R292A. Best binding modes for each protein with the indole ligand were visualized by UCSF CHIMERA [240].

## 5.3. Steady-state kinetics of indole conversion by purified Ar-BVMO

The reason behind exploration of Ar-BVMO as a biocatalyst in the conversion of indole arose from the simple observation that Ar-BVMO R292A mutant expressed in *E. coli* cells resulted in a dark blue pellet after centrifugation, whereas the wild type enzyme did not accumulate any colored pigments. As the blue color is not typical of *E. coli* cells we investigated the reason for this unusual observation. Previous publications have reported the ability of certain microorganisms to convert tryptophan into indole using tryptophanases. Indole can then be further oxidized by a monooxygenase capable of oxidizing C2 or C3 of indole leading to the production of indigo or indirubin [214,241–243]. Several monooxygenases are able to activate indole, but only one study has carried out a more in-depth characterization of a BVMO enzyme performing this reaction [244].

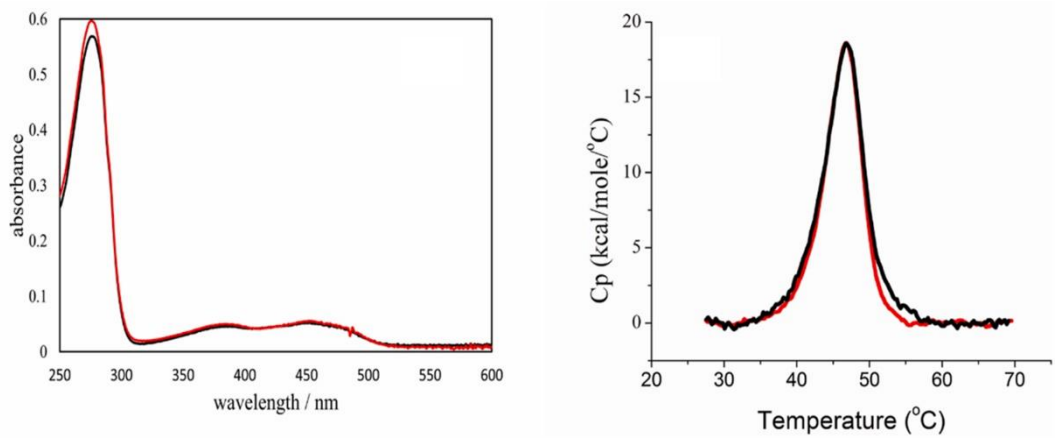


**Figure 38:** Stability and activity of Ar-BVMO. **(A)** Absorbance spectra of purified wild type (black) and mutant Ar-BVMO (red). **(B)** DSC thermograms of wild type (black) and mutant Ar-BVMO (red) at a scan rate of 90 °C/h. (For interpretation of the references to color in this figure legend, the reader is referred to the Web version of this article.)

As a first step to provide experimental evidence that the bacterial Ar-BVMO is involved in the production of indigo, wild type and mutant proteins were expressed in *E. coli* and purified by affinity chromatography due to the presence of a histidine tag at their C-terminal as reported previously [226]. Both proteins were purified as

holoproteins as demonstrated by the typical FAD spectra with absorbance maxima at 375 and 450 nm (Figure 38A).

Differential scanning calorimetry (DSC) was performed to check the stability of the two purified proteins. The results shown in Figure 38B reveal that both proteins exhibit comparable thermal stability as demonstrated by overlapping DSC thermograms with a $T_m$ of 47 °C with almost identical cooperative denaturation behavior indicating that the enzymes are stable and well-folded. These data are in line with previously obtained preliminary melting temperatures obtained by UV/Vis spectroscopy [226].

Once the stability of the purified proteins was established, we investigated their ability to convert indole into indigo by monitoring the production of indigo in an initial screening assay. Only R292A Ar-BVMO was able to convert indole into indigo as demonstrated by the development of a blue color at 620 nm in the kinetic traces (Figure 39A) that was absent for the WT. Therefore, the kinetic parameters were only measured for the mutant enzyme via NADPH consumption in a 200 s timeframe using increasing concentrations of indole as shown in Figure 39B. The calculated kinetic parameters, $K_m$ and $k_{cat}$, for the R292A Ar-BVMO were found to be 1.75 ± 0.24 mM and 0.12 ± 0.01 $sec^{-1}$, respectively.

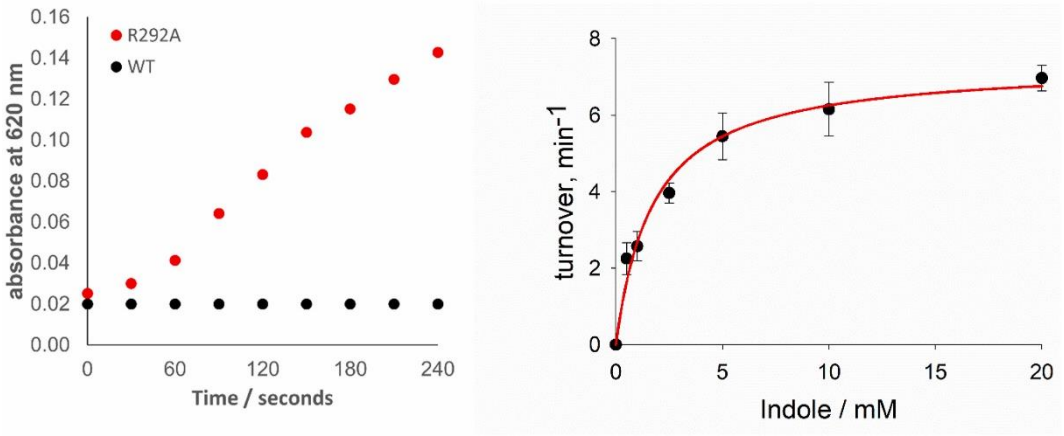


**Figure 39: (A)** Screening assay for indigo production monitoring the increase in absorbance at 620 nm for 240 s. Reaction conditions: 8.6 µM Ar-BVMO, 800 µM NADPH in 50 mM Tris HCl pH 8.5 at 30 °C for 240 s. **(B)** Michaelis-Menten curve for the conversion of indole into indigo by R292A Ar-BVMO. Reaction conditions: 1 µM R292A Ar-BVMO, 160 µM NADPH in 50 mM Tris HCl pH 8.5 at 30 °C for 200 s. Plots are the average of 3 different replicates. Data are mean ± SD of at least 3 replicates. R2 > 0.98.

The above activity measurements confirm that substrate recognition is linked to R292A mutation justifying the accumulation of the dark blue pigment during protein expression in *E. coli*.

## 5.4. The "switch" between indigo and indirubin production

Indole conversion into indigo or indirubin involves both an enzymatic step as well as a chemical one, as shown in Figure 40. Both steps are dependent on various parameters including pH, temperature and ionic strength. Although the optimum temperature used for this enzyme is 37 °C [226], the reaction temperature was lowered to 25 °C to extend the half-life of this biocatalyst and maintain its activity for a longer period of time. The temperature also affects the chemical dimerization reaction, but is not a limiting factor in the quantification of the indigo produced because samples are always evaporated at 55 °C to obtain the indigo powder and achieve the complete dimerization of the enzymatic product.

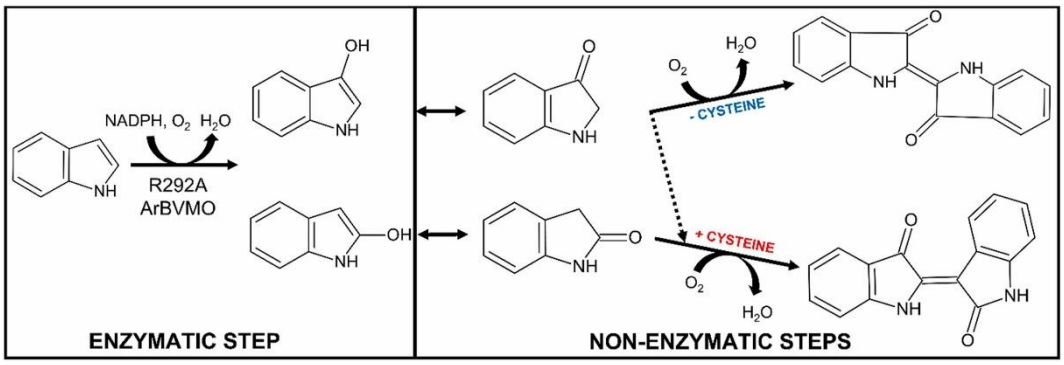


**Figure 40:** A simplified scheme of the reaction steps from indole to indigo or indirubin involving the biocatalyst Ar-BVMO.

In order to find the optimal conditions for the production of indigo and indirubin a high throughput colorimetric assay was performed to determine the best reaction conditions regarding pH and cysteine concentration (only in the case of indirubin). Han and colleagues [227] have previously shown high product selectivity toward indirubin in *E. coli* expressing a bacterial flavin-containing monooxygenase with the addition of cysteine. In this context, cysteine seems to act as a "switch" diverting all indole to the indirubin production pathway [245].

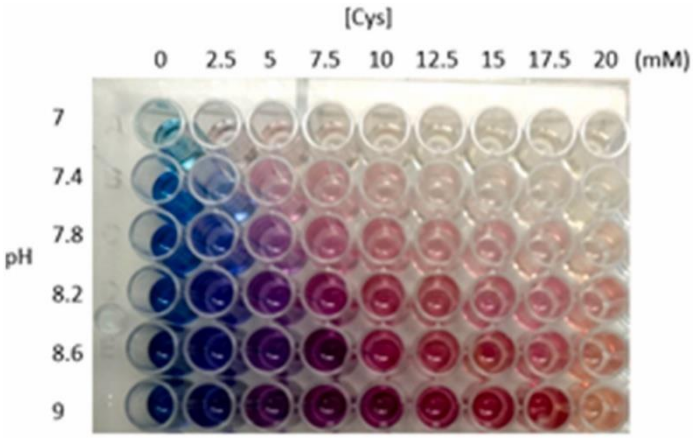


**Figure 41:** The switch between indigo and indirubin production by Ar-BVMO mutant. Microtiter plate showing the effect of various pH and cysteine concentrations (0–20 mM) on the conversion of indole into indigo and indirubin by the mutant enzyme. Reaction conditions: 0.5 μM Ar-BVMO R292A, 5 mM NADPH, 5 mM indole, pH range 7–9, and 0–20 mM cysteine in 100 mM Tris- HCl. The reactions were carried out in a total volume of 200 μL for 48 h at 25 °C and 200 rpm.

As shown in Figure 41, production of indigoids from the oxidation of 5 mM indole by the mutant Ar-BVMO at 25 °C is higher and more selective at pH>8.0. In addition, in the specific case of indirubin the supplementation with 5–10 mM cysteine resulted in the higher yields.

## 5.5. Cysteine “switch” operates via 3-hydroxyindole intermediate

As mentioned above, the Ar-BVMO mutant produces 3-hydroxyindole from indole that upon dimerization is converted to indigo. Although Han and colleagues [227] had demonstrated that the supplementation of cysteine shifts this reaction to indirubin production, the detailed mechanism of this switch was only recently elucidated by Kim's group [245]. The latter group demonstrated that the first step of this switch is based on the reaction of cysteine with 3-hydroxyindole leading to the formation of 2-cysteinylindoleninone, thereby inhibiting the dimerization of 3-hydroxyindole and the production of indigo [245]. This first step therefore results in the accumulation of 3-hydroxyindole, a fluorescent compound that can be monitored by spectroscopy. In order to investigate whether the same reaction pathway is also taking place in the case of mutant Ar-BVMO, reactions were set up with the maximum amount of cysteine (10 mM) added to the enzymatic indole conversion reaction. The data obtained are reported in Figure 42 and demonstrate that as expected, cysteine facilitates the accumulation of the fluorescent 3-

hydroxyindole intermediate (red trace), avoiding its depletion due to dimerization and therefore indigo formation (no added cysteine-black trace).

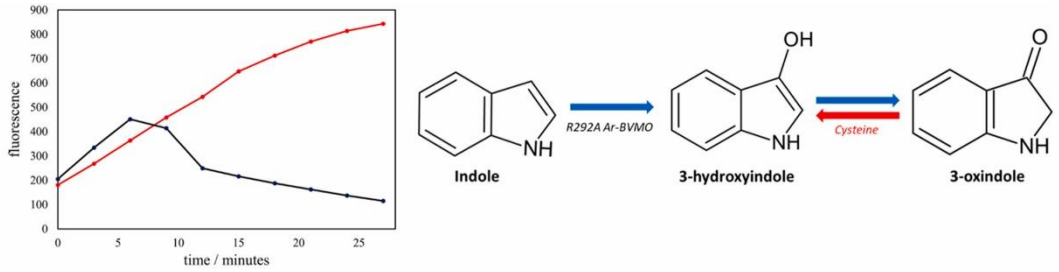


**Figure 42:** Role of cysteine "switch" from indigo to indirubin in the conversion of indole. Left graph: Detection of 3-hydroxindole by exciting the sample at 365 nm in kinetics mode for 25 min and recording the emission at 470 nm. The black data points show the kinetics of the reaction performed in the absence of cysteine, whereas the red data points are the same reaction in the presence of cysteine. Right scheme: indole is rapidly converted to 3-hydroxyindole by R292A Ar-BVMO and consequently to 3-oxindole under oxidative conditions. The addition of cysteine results in the accumulation of the 3-hydroxyindole intermediate.

## 5.6. Production of indigo and indirubin in *E. coli* whole-cells

In order to enhance the yields of the indigoids produced by Ar-BVMO mutant, the logical step of moving from the use of purified enzyme to *E. coli* whole-cells was taken. The use of live bacterial cells as production systems has many advantages in biotechnology from the point of view of system stability, cost-effectiveness and overall yield. Therefore, indigoid production was investigated with *E. coli* whole-cell system harboring the expression vector for Ar-BVMO R292A [224] and addition of indole as substrate. As a preliminary qualitative test, different culture media (LB: Luria-Bertani, TB: terrific broth, and M9 minimal medium) were investigated with the resulting percentage of indole conversion calculated. As shown in Figure 43, TB was found to be the best culture medium for the production of both indigoids using *E. coli* whole-cells. In order to be more cost effective and bypass the addition of NADPH, an NADPH regeneration system consisting of $NADP^+$, citrate and $MgCl_2$ was utilized as it has been shown previously to result in a sustained activity of monooxygenases [235,236].

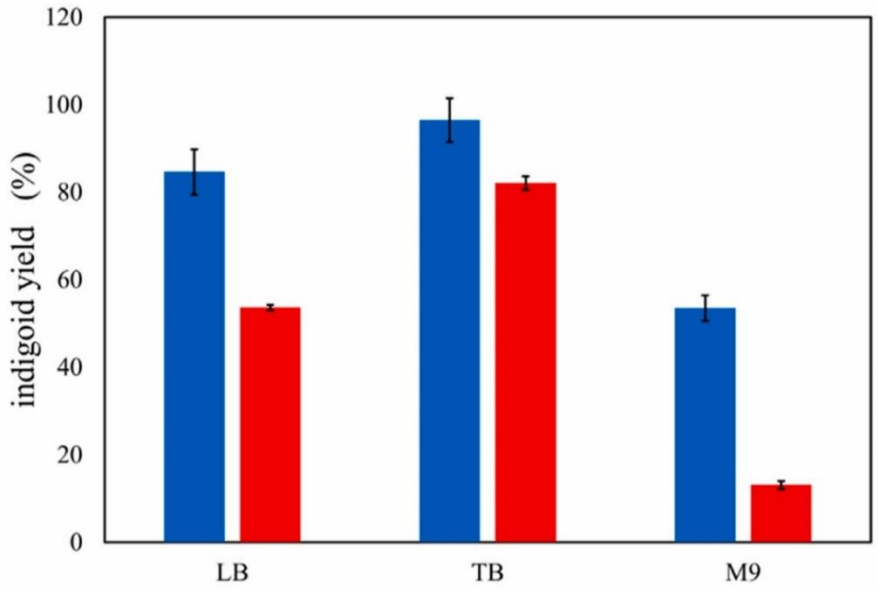


**Figure 43:** Indigoid production in different culture Media. *E. coli* whole-cell indigoids productivity in different media (LB, TB and M9) after 72 h. Blue and red bars indicate the production of indigo and indirubin, respectively. Experiments were performed three times and the error bars represent the standard deviation obtained from the three replicates.

Addition of this regeneration system dramatically increased the yields by 7- and 5-folds for indigo and indirubin, respectively (Figure 44A and B). Under these optimized conditions, it is also interesting to note that indirubin reaches its maximum yield within 24 h whereas indigo production requires >72 h (Figure 44A and B)

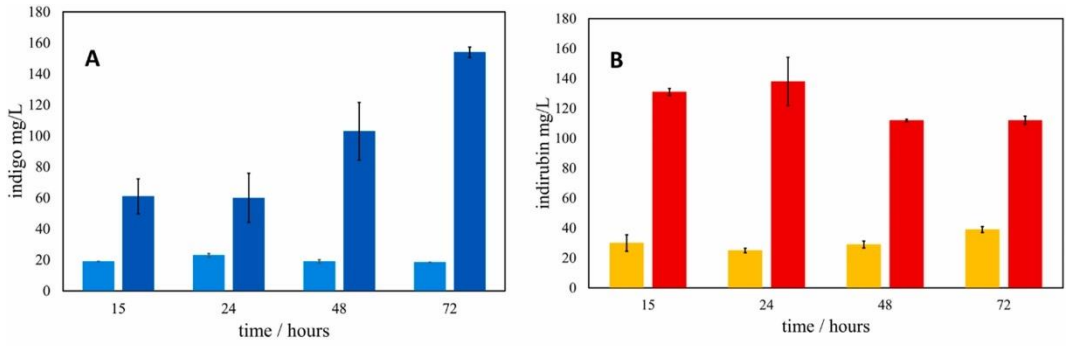


**Figure 44:** Whole-cell R292A Ar-BVMO mediated conversion of indole into indigo and indirubin. **(A)** Whole-cell time dependent conversion of indole to indigo in presence (blue) and absence (light blue) of a NADPH regeneration system. **(B)** Whole-cell time dependent conversion of indole to indirubin in presence (red) and absence (orange) of a NADPH regeneration system. Experiments were performed three times and the error bars represent the standard deviation obtained from the three replicates.

The indigo and indirubin produced using the *E. coli* whole-cell system were analyzed by both TLC and HPLC. The results obtained from the TLC separation are shown in Figure 45A. As can been seen in the latter figure, the commercial standard of indigo is not entirely pure with the presence of a contaminant. A similar result is obtained using Ar-BVMO mutant as the biocatalyst for indigo production. On the other hand, the same Ar-BVMO produces a high purity indirubin with little or no contamination of indigo.

Further investigation of the enzymatically produced indigoids was performed by HPLC analysis and the results are shown in Figure 45B–C. As can be seen in Figure 45, the peaks corresponding to indigo (retention time of 11.1 min) and indirubin (retention time of 11.6) produced by the *E. coli* whole-cell system increase over time. The retention times observed are the same as those of the commercial standards (Figure 45 insets).

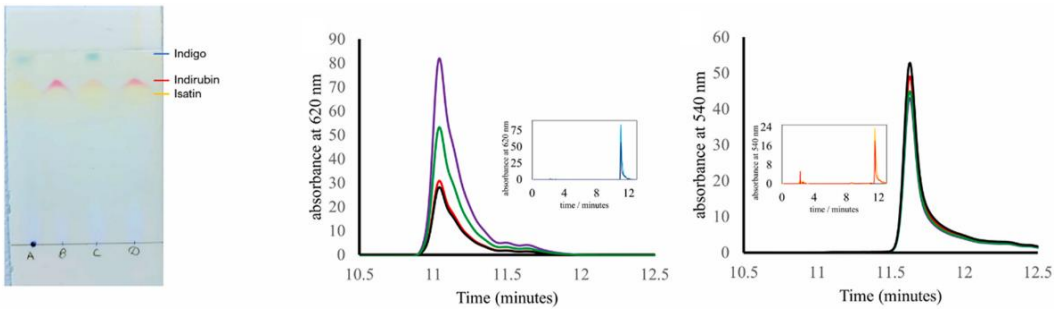


**Figure 45:** TLC and HPLC analysis of indigoids produced in *E. coli* whole-cells. **(A)** indigo standard (Lane A), indirubin standard (Lane B), whole-cell produced indigo (Lane C) and whole-cell produced indirubin (Lane D). Isatin, yellow band, is an intermediate present in all lanes. **(B)** Time-dependent production of indigo up to 72 h. Inset: the overlay of chromatograms of indigo commercial standard (light blue) and whole-cell produced indigo (dark blue) with the same retention time of 11.1 min. **(C)** Time-dependent production of indirubin up to 72 h. Inset: the overlay of chromatograms of indirubin commercial standard (orange) and whole-cell produced indirubin (red) with the same retention time of 11.6 min. For timepoints of both indigo and indirubin: 15 h (red), 24 h (black), 48 h (green) and, 72 h violet.

Previous research carried out on flavin-containing monooxygenases (FMOs) has highlighted the ability of this class of enzymes to act as biocatalysts in the oxidation of indole and its conversion to either indigo or indirubin [201]. These biocatalysts are responsible for the first step of the indole biotransformation i.e. formation of intermediate(s), 2- or 3- hydroxyindole, which depending on the presence of cysteine, a key reactant, can switch to the production of indirubin

[227,245]. The overall mechanism only partially relies on the enzyme activity because the dimerization process is strictly dependent on oxygen availability and can be accelerated by increasing the temperature. Having said that, the initial step is the enzymatic one and, in this context, FMOs, both as purified enzymes and in whole-cell preparations, have been studied for many years whereas very little is known about BVMOs that belong to the same class of FMOs [174,246]. To date, the only BVMO studied in depth for its ability to produce indigo starting from indole, is phenylacetone monooxygenase (PAMO) from *Thermobifida fusca* [244]. Similar to Ar-BVMO, the wild type PAMO does not act as a biocatalyst in indole conversion rather a mutant, M446G, was found to be active in this transformation [244]. BVMOs catalyze Baeyer-Villiger as well as heteroatom oxidations (nitrogen and sulfur containing compounds) but are not able to perform hydroxylations and are very poor epoxidation catalysts. For mutant PAMO, an alternative mechanism going through an initial N-oxidation step with subsequent internal molecular rearrangement was proposed, also in line with observations made with some other FMOs [244]. It is worth noting that in the case of a bacterial FMO, Kang's group [247] using crystal structures as well as biochemical assays, have described overlapping binding sites for $NADP^+$ and indole leading to a direct C-3 indole oxygenation reaction mechanism involving a ping-pong-like interaction of NADPH and indole. This type of C-3 oxygenation has not yet been demonstrated for any BVMO.

In the specific case of Ar-BVMO mutant, we have demonstrated that this biocatalyst leads to the accumulation of 3-hydroxyindole as the reaction intermediate, and that this molecule dimerizes to yield indigo unless cysteine is present, which in turn favors the formation of indirubin as the alternative product. It is clear that Ar-BVMO promotes the accumulation of 3-hydroxyindole however it is not clear whether this intermediate is obtained through a direct hydroxylation reaction (not typical of BVMOs) or the result of a rearrangement of the N-oxide as proposed for PAMO [244]. In order to answer this question, *in silico* molecular docking experiments using a 3D homology model of both wild type and R292A Ar-BVMO with indole were carried out. The docking results are shown in Figure 46 and demonstrate that the mutation of the arginine into an alanine, with a much shorter side chain, creates a large cavity in the active site for the binding of the indole substrate (Figure 46A, B).

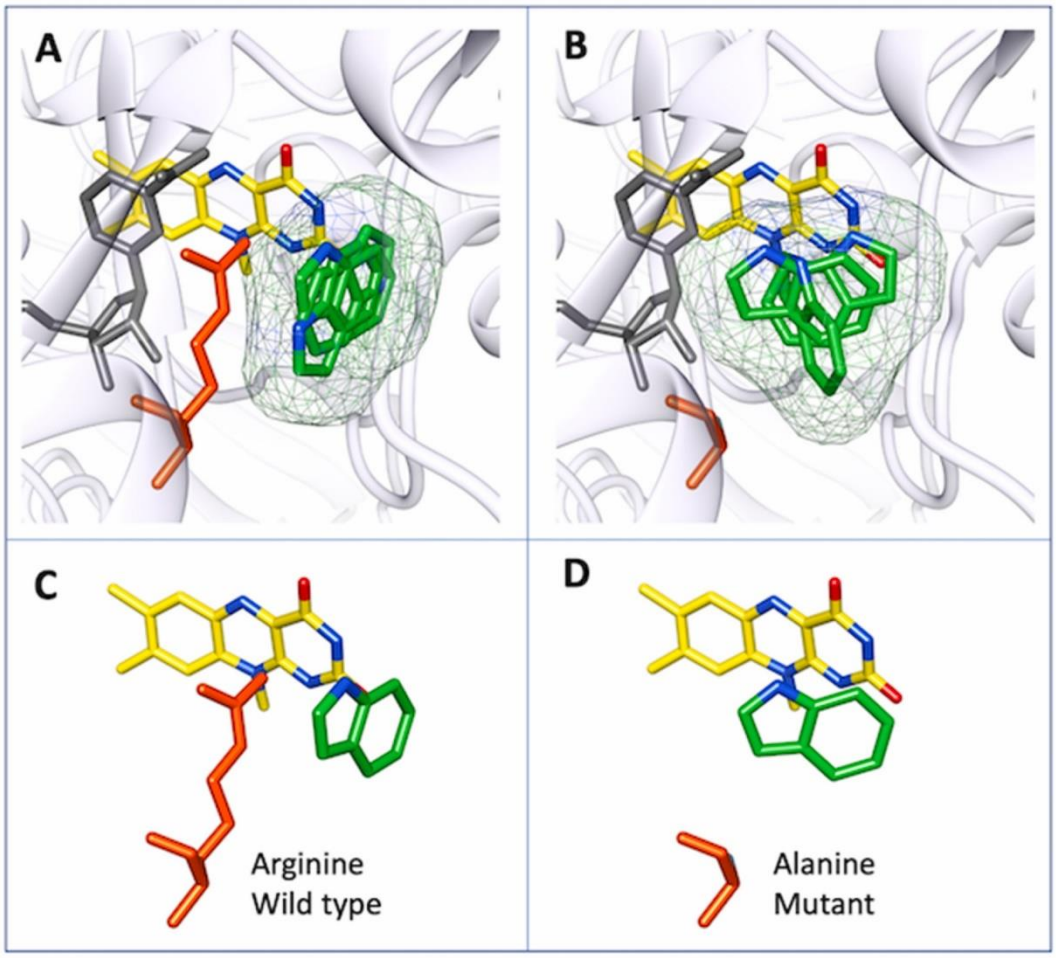


**Figure 8:** In silico molecular docking of indole with Ar-BVMO. **(A)** Wild type Ar-BVMO in complex with indole showing that arginine 292 hampers the N-oxidation of the substrate. Three different binding modes (poses) overlapped (see Table 1 for details), **(B)** R292A Ar-BVMO in complex with indole showing that the mutation allows the N-oxidation of the substrate by allowing different favored binding modes. The best 3 poses are overlapped (see Table 1 for details), **(C)** The most favored orientation of indole with the FAD isoalloxazine (pose 1) of wild type shows indole at a longer distance from the site of N-oxygenation whereas in the mutant **(D)**, the indole is closer in a productive pose. Indole is colored in green, FAD in yellow and $NADP^+$ in grey. The nitrogen atoms of FAD are shown in blue with oxygens in red. The molecular surfaces of the different indole poses are shown as a grey mesh. The figures were generated using the UCSF Chimera program [240].

The docking studies allowed for an indication on the putative positioning of indole in the active site of both proteins. Interestingly, indole can only interact in a single productive orientation within the active site of the wild type Ar-BVMO due to steric hindrance (Figure 45A, Table 11), whereas the mutant allows multiple poses due to the extra cavity (Figure 46B, Table 11). Consequently, in the best 3 protein-ligand binding modes this leads to a more productive binding of indole with shorter distances to the C4a-atom in the mutant Ar-BVMO (Table 11). In addition,

the most favored pose for R292A (pose 1) also shows the secondary amine located in a suitable position for N-oxidation rather than C2 or C3 hydroxylation (Figure 46D). These data are in support of the hypothesis that was originally proposed for PAMO [244], i.e. rearrangement of the N-oxide product and the absence of a direct hydroxylation reaction. Moreover, we have previously shown that the R292A mutation abolishes the ability of Ar-BVMO to perform BV oxidations [226], so the mutation that is detrimental for its original BV reaction can result in a gain of function against a set of N- and possibly S-containing substrates where internal rearrangement of the product structures are allowed.

**Table 11:** Molecular docking of indole with Ar-BVMO.

| Ar-BVMO | Pose | Binding Energy kcal/mol | Distance from flavin C4a to N atom of indole (Å) |
|---|---|---|---|
| Wild type | **1** | **4.56** | **6.2** |
| | **2** | **4.53** | **7.1** |
| | **3** | **4.25** | **8.1** |
| R292A | **1** | **5.25** | **5.2** |
| | **2** | **5.07** | **5.4** |
| | **3** | **5.02** | **5.3** |

Previous studies with FMOs have been mainly aimed at production of indigo but in this work, we have demonstrated the possibility of producing even higher amounts of indirubin using a mutant of Ar-BVMO as a biocatalyst. As shown in Table 12, Ar-BVMO mutant can produce up to 138 mg/L of indirubin starting from indole, second only to the *E. coli* system described by Kim's group [227]. However, our system has two advantages over the latter reported system; the shorter time-period of production (24 versus 48 h), and the use of indole (~1 euro/g) instead of the more expensive tryptophan (~6 euro/g) as the starting material.

Finally, although indirubin is known as a dye, in recent years indirubin-derived molecules have been exploited to a greater extent as possible drugs in the treatment of several different pathologies including cancer [223,248]. Moreover, while indigo is a relatively cheap molecule, indirubin is actually quite expensive. A standard of indirubin for research purposes can cost in excess of 15,000 euro per gram, therefore alternative methods for the production of this compound can be highly desirable.

**Table 12:** Production of indirubin by flavin-containing monooxygenases.

| **Method** | ***E. coli* Host** | **Biocatalyst** | **Substrate** | **Indirubin** | **Reference** |
|---|---|---|---|---|---|
| **1 mL Whole-cell reaction – 24 h** | BL21 | BVMO R292A from *Acinetobacter radioresistens* | 5 mM indole 5 mM Cys | 0.138 g/L | This work |
| **Whole-cell reaction** | BL21 | FMO from *Methylophaga aminisulfidivorans* | 1 mM indole 5 mM Cys | 0.031 g/L | [245] |
| **Flask fermentation – 48 h** | Top10 | FMO from *Corinobacterium glutamicum* | 12 mM Trp | 0.103 g/L | [214] |
| **3000L batch fermentation – 24 h** | DH5α | FMO from *Methylophaga aminisulfidivorans MPT* | 10 mM Trp | 0.005 g/L | [241] |
| **10L batch fermentation – 48 h** | pBlue 1.7 | FMO from *Methylophaga aminisulfidivorans MPT* | 10 mM Trp 3 mM Cys | 0.223 g/L | [227] |

In conclusion, the bacterial whole-cell system of Ar-BVMO not only constitutes a promising starting point for the scale up of high purity indirubin production but is also a green and environmentally sustainable alternative process compared to solely chemical processes.

## 5.7. In vitro indigo/indirubin production mediated by purified hFMO1

Similar experiments to those reported above for BVMO were carried out with hFMO1. As mentioned in Chapter 2, during the expression of hFMO1 in *E. coli*, a light blue colour was observed in the *E. coli* pelleted cells. In order to investigate the nature of this blue colour and after the experiments with BVMO, it was decided to carryour similar experiments with hFMO1.

Initially, both hFMO1 and hFMO3 were screened for their possible indigo production with indole as a substrate and the results are shown in Figure 47A. As can be seen in the figure, hFMO3 is incapable of converting indole whereas hFMO1 showed activity with this substrate and therefore was investigated further.

The formation of the indoxyl sulfate in the human body, as was described by Banoglu's group [228] and demonstrated in Figure 47B, starts with the intestinal bacterial microflora producing indole from tryptophan. Subsequently, the hepatic

P450s (CYP2A6 and CYP2E1) carryout the hydroxylation of the 3rd C-atom of the indole's pyrrole ring forming 3-hydroxyindole (Indoxyl) which after conjugation by sulfotransferases (SULT) is transformed to the final product, 3-sulfonoxyindole (indoxyl sulfate also named as indican). To investigate if the hFMO1 can be involved in the indoxyl sulfate formation it is therefore important to define which product, 3-hydroxyindole or 2-hydroxyindole, will be formed by the enzyme.

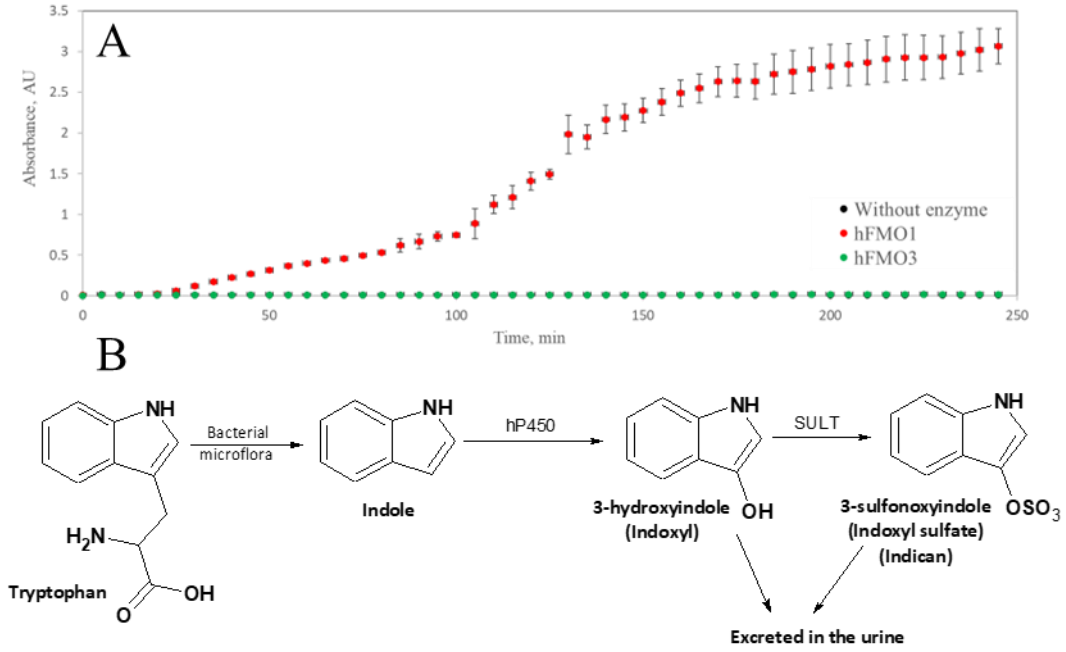


**Figure 47: (A)** Screening for indigo production by monitoring the increase in absorbance at 620 nm for 240 s. Reaction conditions: 5 µM hFMO1/hFMO3, 0.5 mM NADPH, 1 mM indole in 0.1 mM KPi pH 7.4 at 37 °C for 240 s. Estimated standard errors of three different experiments are represented as error bars. **(B)** Metabolic pathway of the indoxyl sulfate formation in vivo [228].

Before setting up any large-scale reactions, the optimal conditions for indigo/indirubin production by hFMO1 enzyme were investigated including cofactor preference, NADH (Figure 48) or NADPH (Figure 49), different pH values and cysteine concentrations. An interesting observation was made that if NADH was used as the reducing agent, the product formed was strictly selective and only indigo could be produced without any traces of indirubin. A linear dependence of the indigo production on pH was observed with pH 7.0 resulting in the highest indigo formed. The presence of cysteine dramatically decreased product formation and in higher concentrations than 2.5 mM no more indigo was detected. Therefore, for hFMO1 the optimal conditions for indigo production were found to be pH 7 without the addition of cysteine.

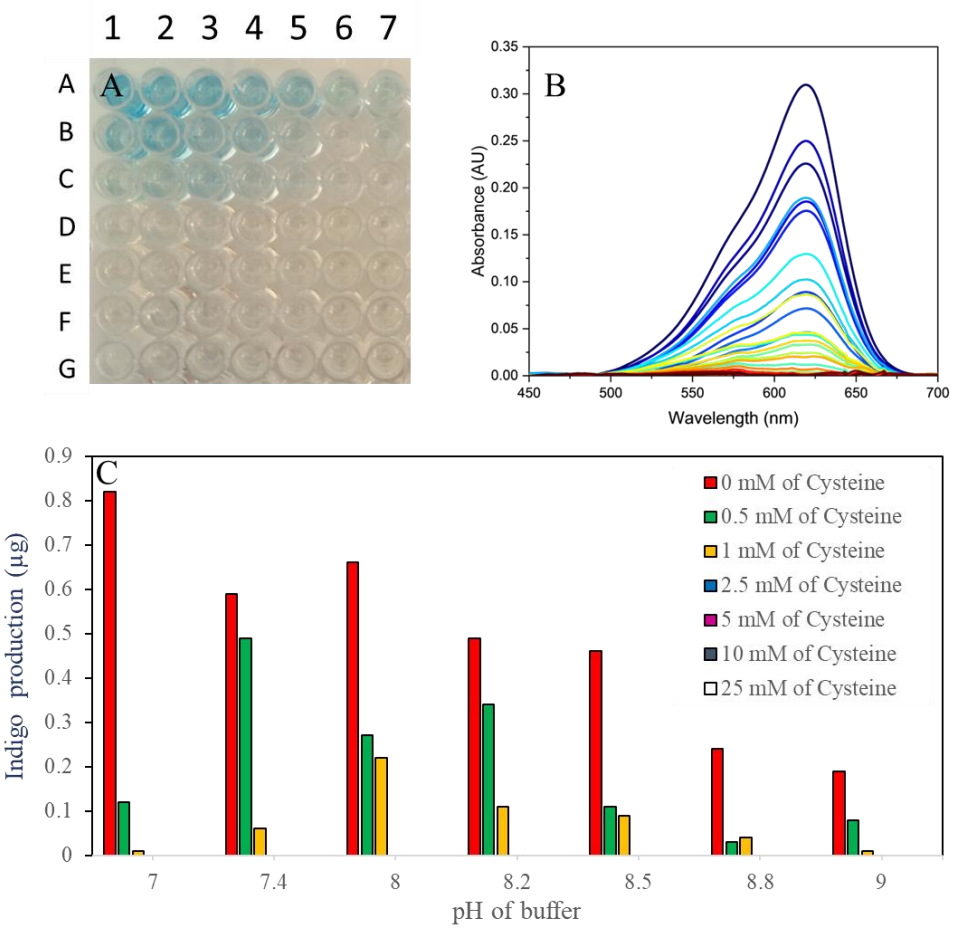


**Figure 48:** In vitro reaction of indole with hFMO1 in the presence of NADH. **(A)** Microtiter plate showing the effect of various pH and cysteine concentrations on the conversion of indole by the enzyme. **(B)** Absorption spectra of the products of the reaction, only indigo with no indirubin detected. **(C)** Quantitative demonstration of the effect of the reaction mixture content on the catalytic reaction. Conditions: 0.5 µM hFMO1, 0.5 mM NADPH, 1 mM indole, pH range 7–9, and 0–25 mM cysteine in 100 mM Tris- HCl. The reactions were carried out in a total volume of 200 µL for 48 h at 25 °C and 200 rpm.

The reaction in the presence of NADPH as a reducing agent again demonstrates a completely different behavior which proves the difference in the interaction between hFMO1 and cofactors already observed in Chapter 2. Unexpectedly, the presence of NADPH resulted in the formation of indirubin not observed with NADH.

The optimal conditions for indigo production were at pH 7.4 without cysteine but in this case, traces of indigo were also detected with 2.5 mM cysteine. The optimal conditions for indirubin production were pH 8.5 in the presence of 1 mM cysteine.

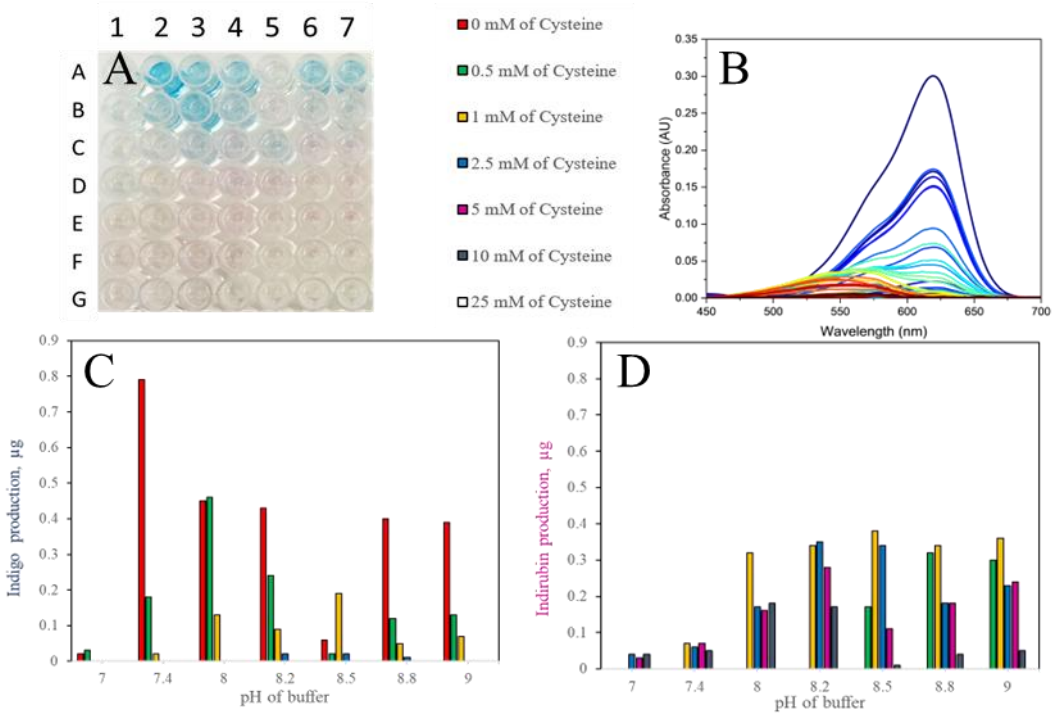


**Figure 49:** In vitro reaction of hFMO1 with indole in the presence of NADPH. **(A)** Microtiter plate showing the effect of various pH and cysteine concentrations on the conversion of indole by the enzyme. **(B)** Absorption spectra of the products of the reaction, both products were detected. Quantitative demonstration of the effect of the reaction mixture content on the **(C)** indigo and **(D)** indirubin production by hFMO1. Conditions: 0.5 µM hFMO1, 0.5 mM NADPH, 1 mM indole, pH range 7–9, and 0–25 mM cysteine in 100 mM Tris- HCl. The reactions were carried out in a total volume of 200 µL for 48 h at 25 °C and 200 rpm.

To investigate the pH-dependence of the indigo production at lower pH values the reaction was carried out without cysteine at the full range of KPi buffer with the addition of NADPH/NADH cofactor. The results are shown in Figure 50. As can be see in the figure, around neutrality the production of both indigoids are the lowest observed. This observation requires further investigation to understand its origin. However, in order to move forward the optimal pH value for indigo production was 8.0 in the presence of NADPH and 6.8 for NADH in the KPi buffer.

The next measurements were carried out to investigate the effect of various concentrations of cysteine and indole on the indigoids formed. done with the estimated optimal pH of KPi buffer in the presence of cysteine and various concentrations of indole. The results are shown in Figure 51.

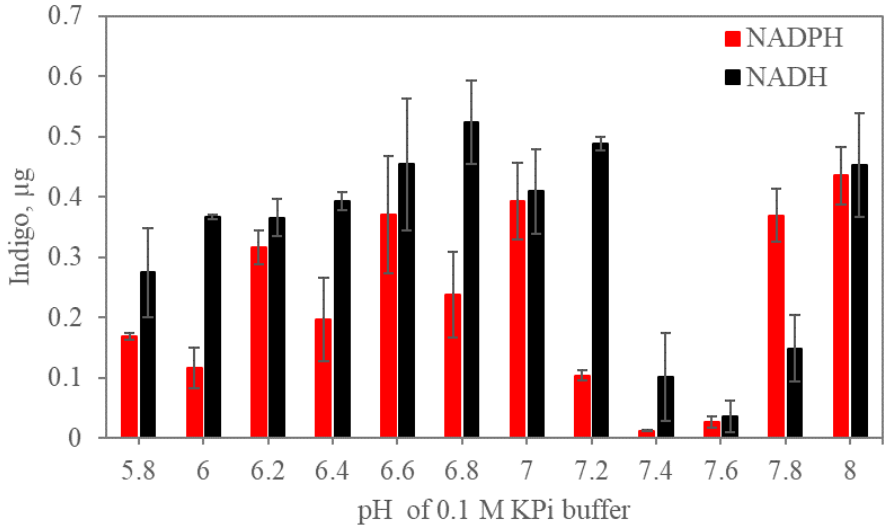


**Figure 50:** In vitro reaction of hFMO1 in the presence of NADPH/NADH at various pH values. Conditions: 0.5 µM hFMO1, 0.5 mM NADPH/NADH, 1 mM indole, pH range 5.8–8.0 in 100 mM KPi buffer. The reactions were carried out in a total volume of 200 µL for 48 h at 25 °C and 200 rpm. Estimated standard errors of three different experiments are represented as error bars.

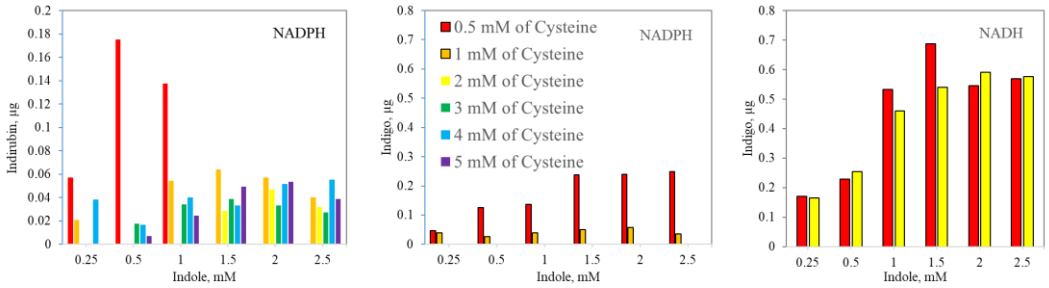


A B C

**Figure 51:** In vitro reaction of hFMO1 in the presence of various indole and cysteine concentrations. **(A)** Production of indirubin in the presence of NADPH **(B)** Production of indigo in the presence of NADPH **(C)** Production of indigo in the presence of NADH. Conditions: 0.5 µM hFMO1, 0.5 mM NADPH/NADH, 0.25-2.5 mM indole and 0.5–5 mM cysteine in 100 mM KPi buffer (pH: 6.8 for NADH and 8.0 for NADPH). The reactions were carried out in a total volume of 200 µL for 24 h at 25 °C and 200 rpm.

In the presence of NADH, as also mentioned earlier, only indigo was produced, Figure 51C. This observation might mean that the enzymatic reaction is strictly selective and forms just 3-hydroxyindole, whereas in the case of NADPH the oxygenation reaction is less selective and together with 3-hydroxyindole, the 2-

hydroxyindole is also formed. The addition of cysteine moves the reaction balance to indirubin production (as also observed in reactions with BVMO) but in this case only when NADPH is used as the reducing agent.

Reactions were also carried out in Tris-HCl buffer and the results are shown in Figure 52. Using this buffer higher amounts of indirubin are produced. Increasing the cysteine concentration pushes the reaction towards indirubin production as was expected. Furthermore, in order to move the balance completely to indirubin, it was found that a concentration ratio of no less the 2:1 cysteine:indole is required.

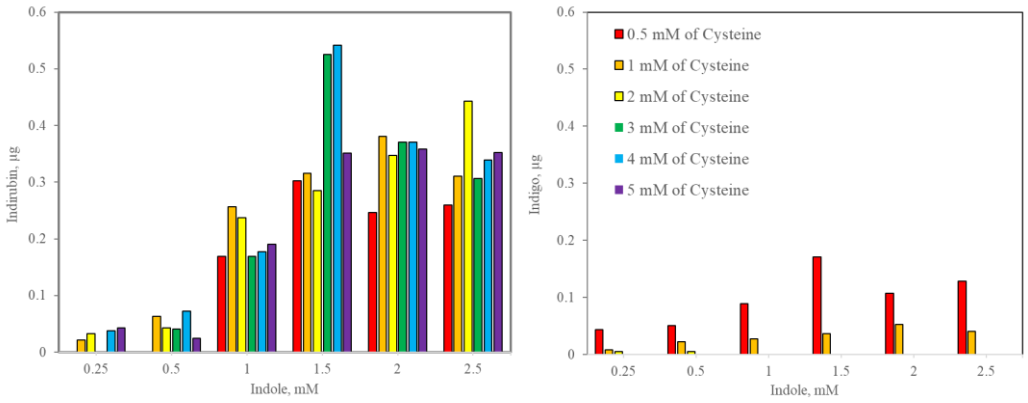


A B

**Figure 52:** In vitro production of indirubin **(A)** and indigo **(B)** by hFMO1 in the presence of various indole and cysteine concentrations. Conditions: 0.5 µM hFMO1, 0.5 mM NADPH, 0.25-2.5 mM indole and 0.5–5 mM cysteine in 100 mM Tris-HCl buffer pH 8.5. The reactions were carried out in a total volume of 200 µL for 24 h at 25 °C and 200 rpm.

## 5.8. Production of indigoids by *E. coli* whole-cells expressing hFMO1

In order to increase the yields of indigoids produced by hFMO1, it was decided to also test the same reactions in *E. coli* whole-cells expressing hFMO1. If successful, this system could not only be used for indigoids' production but can also serve as a marker of active enzyme expressed in *E. coli* cells (without the need for further purification and activity assay since the *E. coli* pelleted cells would display a blue colour). This type of in situ colourimetric activity assay is currently unavailable for any hFMO.

The first reaction for indirubin production was carried out at different time points, in the presence and/or absence of cysteine and with or without an $NADP^+$ regeneration system. However, since the hFMO1 expression is optimal after 24 h, it was decided to keep this time point for measurements of the effect of other contributing factors such as the concentration of cysteine. Moreover, the quantity of product at 24 h was also found to be sufficient for spectroscopic detection.

The next parameter to be investigated in the production of indirubin was the concentration of cysteine which as mentioned earlier for the BVMO reactions, is required to move the equilibrium away from indigo and towards indirubin. For this reason, different concentrations of indole and cysteine were tested. From the obtained results, the optimal ratio between the concentration of cysteine to that of indole was found to be 1:2. In addition, although the expression of hFMO1 requires temperatures lower than 37 ºC, the amount of indirubin produced was higher at 37 ºC degrees rather than 25 ºC (Figure 53).

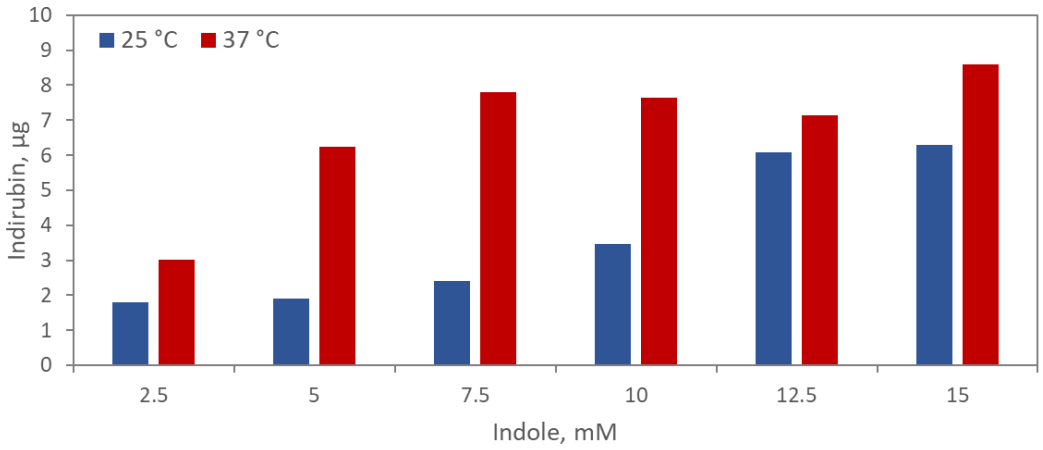


**Figure 53:** Effect of temperature on the whole-cell indirubin production. Blue and red bars indicate the production of indirubin at 25 and 37 °C, respectively. Reaction mixture contained recombinant *E. coli* JM109 cells in the presence of 0.3 mM $NADP^+$, 50 mM trisodium citrate,10 mM $MgCl_2$, cysteine to indole ratio of 1:2.

In the next set of experiments the influence of cofactors on the indole conversion in the whole-cell reaction was investigated in the presence or absence of added cofactors (NADPH/NADH), as well as a NADPH regeneration system. The presence of cysteine within the whole-cell set up and its influence on the indigo/indirubin production was also studied. The results obtained are shown in Figure 54.

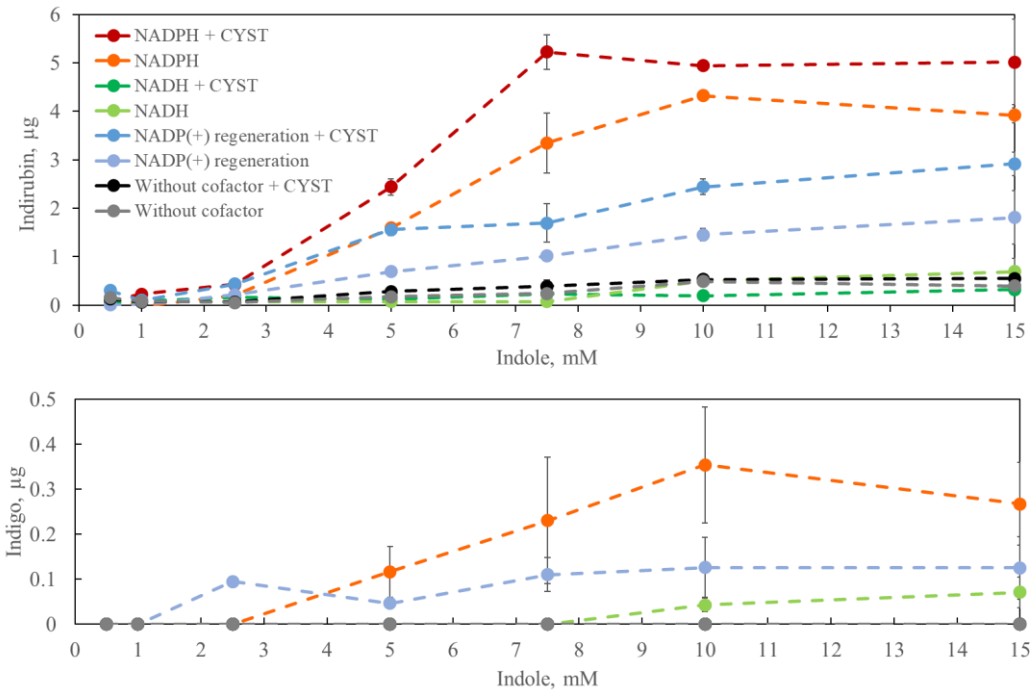


**Figure 54:** Whole-cell hFMO1 mediated conversion of indole into indigo and indirubin. Reactions were carried out in a final volume of 1 mL in 0.1 M Tris-HCl buffer pH 8.5 containing recombinant *E. coli* JM109 ($OD_{600}$ = 10), 0.3 mM NADPH/NADH/$NADP^+$, 50 mM trisodium citrate, 10 mM $MgCl_2$, cysteine to indole ratio of 1:2. Measurements were carried out at 37 °C, 200 rpm for 24 hours. Estimated standard errors of three different experiments are represented as error bars.

The presence of NADPH or $NADP^+$ significantly increased the conversion of indole however, in the case of the whole-cell experiments NADH does not play a significant role in indigo production contrary to what was observed in the *in vitro* reactions. As expected in the presence of cysteine, the production of indirubin was increased by nearly 1.5 times as shown in Figure 54. Under the investigated conditions, the amount of indigo produced was always lower than that of indirubin.

In summary, hFMO1 reaction with indole requires a more in depth investigation first to decipher the mechanism by which NADPH and NADH result in different amounts of product being formed and secondly to further optimise the conditions in order to produce larger quantities of the indigoids. Moreover, the mechanism by which hFMO1 is capable of carbon hydroxylation is still unknown and a perspective topic for further investigation in order to also understand its natural role in the human renal system. Finally, in view of the obtained results it is plausible that hFMO1 can play an important role in indoxyl sulfate formation.

# General conclusions and future perspectives

Human FMO1 is an important drug metabolising enzyme involved in the NADPH/NADH-dependent monooxygenation of soft nucleophilic N- and S-heteroatom containing xenobiotics. This enzyme has also recently been implicated in the production of taurine in humans. In general, hFMO1 structure and reaction kinetics have not been fully studied mainly due to the many difficulties associated with its *in vitro* expression and purification. In this work, some of these obstacles were confronted and the full-length recombinant enzyme was successfully expressed in *E. coli JM109* and purified. Having access to mg quantities of the purified hFMO1 allowed for a more indepth *in vitro* characterization of this enzyme through different spectroscopical methodologies.

One of the most important findings of this work was the demonstration of the differences in the C4a-hydroperoxyflavin stabilization in comparison with the other representative members of the FMO family. These experiments were carried out using stopped-flow spectrophotometry. This important catalytic cycle intermediate was shown to be more stable in hFMO1 as compared to hFMO3. The observed stability has direct consequences for the reactivity of this enzyme with different substrates.

Another important factor in the activity of hFMO1 as compared to other members of the FMO family is its reduction by both NADPH and NADH cofactors. Again, in other members of the family, NADPH is the only cofactor capable of reducing the FAD-bound cofactor. For future studies, it is important to understand how exactly these cofactors bind to the active site of the enzyme and which structural changes they can induce after binding. It will be useful to perform these studies with indole as the substrate because, as was demonstrated in this work, indole conversion mediated by hFMO1 is not only effected by pH, but also by the cofactor.

As a biotechnological approach for the use of this human enzyme, it was interfaced with electrodes. The initial results demonstrated the successful immobilization of hFMO1 on the nanostructured electrode and paved the way for

its application. The *in vitro* bioelectrochemical platform was subsequently used for mimicking the fate of phorate pesticide within our bodies, going through a sequential metabolism based on the tandem reactions of hFMO1 and CYP3A4. However, in order to increase the stability and performance of the system it would be advantageous to covalently immobilize the hFMO1 on gold electrodes. This can be done through direct linkage between the electrode and a unique surface exposed cysteine residue of the enzyme. For this reason, site-directed mutagenesis can be performed where the already existing exposed cysteine residues are substituted with serine residues with only one exposed cysteine remaining. Cys 116 was identified as a good candidate for the direct covalent linkage because it has a high surface exposure and is located at the opposite side of the access channel to the catalytic site. This will result in the remaining three cysteine residues to be mutated to serines: Cys111, Cys 423 and Cys 425. Moreover, the *in vitro* bioelectrochemical platform with the immobilized hFMO1 can be coupled to a microfluidics system which can ultimately act as a liver chip mimicking the metabolic pathway of various drugs and xenobiotics.

In terms of the native role of hFMO1 within humans, an important point that must be investigated is whether its polymorphic variants are also capable of oxidizing indole or C-hetero atoms in general. In a similar fashion, the polymorphic variants should be investigated to understand whether they can be reduced by NADH and catalyze the conversion of hypotaurine to taurine as demonstrated for the wild type enzyme. Finally, it would be advantageous to understand whether hFMO1 can be involved in the indoxyl sulfate production in humans, as this would help understand one of the possible reasons behind the progression of chronic kidney and cardiovascular diseases.

# References


[1] B. Testa, W. Soine, Principles of Drug Metabolism, in: Burger's Medicinal Chemistry and Drug Discovery, John Wiley & Sons, Ltd, 2003: pp. 431–498. https://doi.org/10.1002/0471266949.bmc033.

[2] N.T. Issa, H. Wathieu, A. Ojo, S.W. Byers, S. Dakshanamurthy, Drug Metabolism in Preclinical Drug Development: A Survey of the Discovery Process, Toxicology, and Computational Tools, CDM. 18 (2017). https://doi.org/10.2174/1389200218666170316093301.

[3] A.D. Patterson, F.J. Gonzalez, J.R. Idle, Xenobiotic metabolism: a view through the metabolometer, Chem Res Toxicol. 23 (2010) 851–860. https://doi.org/10.1021/tx100020p.

[4] S.A. Sheweita, Drug-metabolizing enzymes: mechanisms and functions, Curr Drug Metab. 1 (2000) 107–132. https://doi.org/10.2174/1389200003339117.

[5] M. Öeren, P.J. Walton, P.A. Hunt, D.J. Ponting, M.D. Segall, Predicting reactivity to drug metabolism: beyond P450s—modelling FMOs and UGTs, J Comput Aided Mol Des. 35 (2021) 541–555. https://doi.org/10.1007/s10822-020-00321-1.

[6] J.R. Cashman, Structural and Catalytic Properties of the Mammalian Flavin-Containing Monooxygenase, Chem. Res. Toxicol. 8 (1995) 165–181. https://doi.org/10.1021/tx00044a001.

[7] J.R. Cashman, Human Flavin-Containing Monooxygenase Substrate Specificity and Role in Drug Metabolism, Current Drug Metabolism. 1 (2000) 181–191. https://doi.org/10.2174/1389200003339135.

[8] N.P. Hajjar, E. Hodgson, Flavin adenine dinucleotide--dependent monooxygenase: its role in the sulfoxidation of pesticides in mammals, Science. 209 (1980) 1134–1136. https://doi.org/10.1126/science.7403873.

[9] B. Furnes, D. Schlenk, Evaluation of Xenobiotic N- and S-Oxidation by Variant Flavin-Containing Monooxygenase 1 (FMO1) Enzymes, Toxicological Sciences. 78 (2004) 196–203. https://doi.org/10.1093/toxsci/kfh079.

[10] D.M. Ziegler, Recent Studies on the Structure and Function of Multisubstrate Flavin-Containing Monooxygenases, Annual Review of Pharmacology and Toxicology. 33 (1993) 179–199. https://doi.org/10.1146/annurev.pa.33.040193.001143.

[11] L.L. Poulsen, D.M. Ziegler, Multisubstrate flavin-containing monooxygenases: applications of mechanism to specificity, Chemico-Biological Interactions. 96 (1995) 57–73. https://doi.org/10.1016/0009-2797(94)03583-T.

[12] D.M. Ziegler, AN OVERVIEW OF THE MECHANISM, SUBSTRATE SPECIFICITIES, AND STRUCTURE OF FMOs, Drug Metabolism Reviews. 34 (2002) 503–511. https://doi.org/10.1081/DMR-120005650.

[13] I.R. Phillips, E.A. Shephard, Endogenous Roles of Mammalian Flavin-Containing Monooxygenases, Catalysts. 9 (2019) 1001. https://doi.org/10.3390/catal9121001.

[14] G. Catucci, C. Gao, G. Rampolla, G. Gilardi, S.J. Sadeghi, Uncoupled human flavin-containing monooxygenase 3 releases superoxide radical in addition to hydrogen peroxide, Free Radic Biol Med. 145 (2019) 250–255. https://doi.org/10.1016/j.freeradbiomed.2019.09.038.

[15] M. Shimizu, N. Hirose, M. Kato, H. Sango, Y. Uenuma, M. Makiguchi, E. Hishinuma, S. Saito, M. Hiratsuka, H. Yamazaki, Further survey of genetic variants of flavin-containing monooxygenase 3 (FMO3) in Japanese subjects found in an updated database of genome resources and identified by phenotyping for trimethylaminuria, Drug Metabolism and Pharmacokinetics. 46 (2022) 100465. https://doi.org/10.1016/j.dmpk.2022.100465.

[16] S. Bortolussi, G. Catucci, G. Gilardi, S.J. Sadeghi, N- and S-oxygenation activity of truncated human flavin-containing monooxygenase 3 and its common polymorphic variants, Archives of Biochemistry and Biophysics. 697 (2021) 108663. https://doi.org/10.1016/j.abb.2020.108663.

[17] I.R. Phillips, E.A. Shephard, Drug metabolism by flavin-containing monooxygenases of human and mouse, Expert Opinion on Drug Metabolism & Toxicology. 13 (2017) 167–181. https://doi.org/10.1080/17425255.2017.1239718.

[18] F. Fiorentini, M. Geier, C. Binda, M. Winkler, K. Faber, M. Hall, A. Mattevi, Biocatalytic Characterization of Human FMO5: Unearthing Baeyer–Villiger Reactions in Humans, ACS Chem. Biol. 11 (2016) 1039–1048. https://doi.org/10.1021/acschembio.5b01016.

[19] F. Fiorentini, E. Romero, M.W. Fraaije, K. Faber, M. Hall, A. Mattevi, Baeyer–Villiger Monooxygenase FMO5 as Entry Point in Drug Metabolism, ACS Chem. Biol. 12 (2017) 2379–2387. https://doi.org/10.1021/acschembio.7b00470.

[20] D.M. Ziegler, L.L. Poulsen, E.M. McKee, Interaction of Primary Amines with a Mixed-Function Amine Oxidase Isolated from Pig Liver Microsomes, Xenobiotica. 1 (1971) 523–531. https://doi.org/10.3109/00498257109041521.

[21] C. Dolphin, E.A. Shephard, S. Povey, C.N. Palmer, D.M. Ziegler, R. Ayesh, R.L. Smith, I.R. Phillips, Cloning, primary sequence, and chromosomal mapping of a human flavin-containing monooxygenase (FMO1), Journal of Biological Chemistry. 266 (1991) 12379–12385. https://doi.org/10.1016/S0021-9258(18)98908-8.

[22] I.R. Phillips, C.T. Dolphin, P. Clair, M.R. Hadley, A.J. Hutt, R.R. McCombie, R.L. Smith, E.A. Shephard, The molecular biology of the flavin-containing monooxygenases of man, Chem Biol Interact. 96 (1995) 17–32. https://doi.org/10.1016/0009-2797(94)03580-2.

[23] S.B. Koukouritaki, P. Simpson, C.K. Yeung, A.E. Rettie, R.N. Hines, Human Hepatic Flavin-Containing Monooxygenases 1 (FMO1) and 3 (FMO3) Developmental Expression, Pediatr Res. 51 (2002) 236–243. https://doi.org/10.1203/00006450-200202000-00018.

[24] S.K. Krueger, D.E. Williams, Mammalian flavin-containing monooxygenases: structure/function, genetic polymorphisms and role in drug metabolism, Pharmacology & Therapeutics. 106 (2005) 357–387. https://doi.org/10.1016/j.pharmthera.2005.01.001.

[25] J.R. Cashman, The implications of polymorphisms in mammalian flavin-containing monooxygenases in drug discovery and development, Drug Discovery Today. 9 (2004) 574–581. https://doi.org/10.1016/S1359-6446(04)03136-8.

[26] B. Furnes, D. Schlenk, Evaluation of xenobiotic N- and S-oxidation by variant flavin-containing monooxygenase 1 (FMO1) enzymes, Toxicol Sci. 78 (2004) 196–203. https://doi.org/10.1093/toxsci/kfh079.

[27] S.B. Koukouritaki, R.N. Hines, Flavin-containing monooxygenase genetic polymorphism: impact on chemical metabolism and drug development, Pharmacogenomics. 6 (2005) 807–822. https://doi.org/10.2217/14622416.6.8.807.

[28] G. Bailleul, C.R. Nicoll, M.L. Mascotti, A. Mattevi, M.W. Fraaije, Ancestral reconstruction of mammalian FMO1 enables structural determination, revealing unique features that explain its catalytic properties, Journal of Biological Chemistry. 296 (2021) 100221. https://doi.org/10.1074/jbc.RA120.016297.

[29] O. Dym, D. Eisenberg, Sequence-structure analysis of FAD-containing proteins, Protein Science. 10 (2001) 1712–1728. https://doi.org/10.1110/ps.12801.

[30] G. Catucci, G. Gilardi, L. Jeuken, S.J. Sadeghi, In vitro drug metabolism by C-terminally truncated human flavin-containing monooxygenase 3, Biochemical Pharmacology. 83 (2012) 551–558. https://doi.org/10.1016/j.bcp.2011.11.029.

[31] B. Furnes, D. Schlenk, Extrahepatic Metabolism of Carbamate and Organophosphate Thioether Compounds by the Flavin-Containing Monooxygenase and Cytochrome P450 Systems, Drug Metab Dispos. 33 (2005) 214–218. https://doi.org/10.1124/dmd.104.000984.

[32] X. Hai, E. Adams, J. Hoogmartens, A. Van Schepdael, Enantioselective in-line and off-line CE methods for the kinetic study on cimetidine and its chiral metabolites with reference to flavin-containing monooxygenase genetic isoforms, ELECTROPHORESIS. 30 (2009) 1248–1257. https://doi.org/10.1002/elps.200800604.

[33] S. Veeravalli, I.R. Phillips, R.T. Freire, D. Varshavi, J.R. Everett, E.A. Shephard, Flavin-Containing Monooxygenase 1 Catalyzes the Production of Taurine from Hypotaurine, Drug Metab Dispos. 48 (2020) 378–385. https://doi.org/10.1124/dmd.119.089995.

[34] H. Eng, R. Sharma, A. Wolford, L. Di, R.B. Ruggeri, L. Buckbinder, E.L. Conn, D.K. Dalvie, A.S. Kalgutkar, Species Differences in the Oxidative Desulfurization of a Thiouracil-Based Irreversible Myeloperoxidase Inactivator by Flavin-Containing Monooxygenase Enzymes, Drug Metab Dispos. 44 (2016) 1262–1269. https://doi.org/10.1124/dmd.116.070185.

[35] J.P. Driscoll, I. Aliagas, J.J. Harris, J.S. Halladay, S. Khatib-Shahidi, A. Deese, N. Segraves, S.C. Khojasteh-Bakht, Formation of a Quinoneimine Intermediate of 4-Fluoro-N-methylaniline by FMO1: Carbon Oxidation Plus Defluorination, Chem. Res. Toxicol. 23 (2010) 861–863. https://doi.org/10.1021/tx1000688.

[36] D. Schlenk, J.R. Cashman, C. Yeung, X. Zhang, A.E. Rettie, Role of human flavin-containing monooxygenases in the sulfoxidation of [14C]aldicarb, Pesticide Biochemistry and Physiology. 73 (2002) 67–73. https://doi.org/10.1016/S0048-3575(02)00013-5.

[37] S. Giri, K.W. Krausz, J.R. Idle, F.J. Gonzalez, The metabolomics of (±)-arecoline 1-oxide in the mouse and its formation by human flavin-containing monooxygenases, Biochemical Pharmacology. 73 (2007) 561–573. https://doi.org/10.1016/j.bcp.2006.10.017.

[38] D.H. Lang, A.E. Rettie, In vitro evaluation of potential in vivo probes for human flavin-containing monooxygenase (FMO): metabolism of benzydamine and caffeine by FMO and P450 isoforms, British Journal of Clinical Pharmacology. 50 (2000) 311–314. https://doi.org/10.1046/j.1365-2125.2000.00265.x.

[39] M. Yamazaki, M. Shimizu, Y. Uno, H. Yamazaki, Drug oxygenation activities mediated by liver microsomal flavin-containing monooxygenases 1 and 3 in humans, monkeys, rats, and minipigs, Biochemical Pharmacology. 90 (2014) 159–165. https://doi.org/10.1016/j.bcp.2014.04.019.

[40] T. Taniguchi-Takizawa, M. Shimizu, T. Kume, H. Yamazaki, Benzydamine N-oxygenation as an index for flavin-containing monooxygenase activity and benzydamine N-demethylation by cytochrome P450 enzymes in liver microsomes from rats, dogs, monkeys, and humans, Drug Metabolism and Pharmacokinetics. 30 (2015) 64–69. https://doi.org/10.1016/j.dmpk.2014.09.006.

[41] R. Indra, K. Vavrová, P. Pompach, Z. Heger, P. Hodek, Identification of Enzymes Oxidizing the Tyrosine Kinase Inhibitor Cabozantinib: Cabozantinib Is Predominantly Oxidized by CYP3A4 and Its Oxidation Is Stimulated by cyt b5 Activity, Biomedicines. 8 (2020) 547. https://doi.org/10.3390/biomedicines8120547.

[42] T. Schulz-Utermoehl, M. Spear, C.R.J. Pollard, C. Pattison, H. Rollison, S. Sarda, M. Ward, N. Bushby, A. Jordan, M. Harrison, In Vitro Hepatic Metabolism of Cediranib, a Potent Vascular Endothelial Growth Factor Tyrosine Kinase Inhibitor: Interspecies Comparison and Human Enzymology, Drug Metab Dispos. 38 (2010) 1688–1697. https://doi.org/10.1124/dmd.110.033159.

[43] T. Shiraga, K. Yajima, T. Teragaki, K. Suzuki, T. Hashimoto, T. Iwatsubo, A. Miyashita, T. Usui, Identification of Enzymes Responsible for the *N*-Oxidation of Darexaban Glucuronide, the Pharmacologically Active Metabolite of Darexaban, and the Glucuronidation of Darexaban *N*-Oxides in Human Liver Microsomes, Biological and Pharmaceutical Bulletin. 35 (2012) 413–421. https://doi.org/10.1248/bpb.35.413.

[44] É. Szökő, T. Tábi, T. Borbás, B. Dalmadi, K. Tihanyi, K. Magyar, Assessment of the N-oxidation of deprenyl, methamphetamine, and amphetamine enantiomers by chiral capillary electrophoresis: An in vitro metabolism study, ELECTROPHORESIS. 25 (2004) 2866–2875. https://doi.org/10.1002/elps.200406023.

[45] K.A. Usmani, E.D. Karoly, E. Hodgson, R.L. Rose, In Vitro Sulfoxidation of Thioether Compounds by Human Cytochrome P450 and Flavin-Containing Monooxygenase Isoforms with Particular Reference to the Cyp2c Subfamily, Drug Metab Dispos. 32 (2004) 333–339. https://doi.org/10.1124/dmd.32.3.333.

[46] L. Qian, P.R. Ortiz de Montellano, Oxidative Activation of Thiacetazone by the Mycobacterium tuberculosis Flavin Monooxygenase EtaA and Human FMO1 and FMO3, Chem. Res. Toxicol. 19 (2006) 443–449. https://doi.org/10.1021/tx050328b.

[47] M.C. Henderson, L.K. Siddens, J.T. Morré, S.K. Krueger, D.E. Williams, Metabolism of the anti-tuberculosis drug ethionamide by mouse and human FMO1, FMO2 and FMO3 and mouse and human lung microsomes, Toxicology and Applied Pharmacology. 233 (2008) 420–427. https://doi.org/10.1016/j.taap.2008.09.017.

[48] A.A. Francois, C.R. Nishida, P.R.O. de Montellano, I.R. Phillips, E.A. Shephard, Human Flavin-Containing Monooxygenase 2.1 Catalyzes Oxygenation of the Antitubercular Drugs Thiacetazone and Ethionamide, Drug Metab Dispos. 37 (2009) 178–186. https://doi.org/10.1124/dmd.108.024158.

[49] J. Joo, Z. Wu, B. Lee, J.C. Shon, T. Lee, I.-K. Lee, T. Sim, K.-H. Kim, N.D. Kim, S.H. Kim, K.-H. Liu, In vitro metabolism of an estrogen-related receptor γ modulator, GSK5182, by human liver microsomes and recombinant cytochrome P450s, Biopharmaceutics & Drug Disposition. 36 (2015) 163–173. https://doi.org/10.1002/bdd.1929.

[50] R.J. Rodriguez, C.L. Miranda, Isoform Specificity of N-Deacetyl Ketoconazole by Human and Rabbit Flavin-Containing Monooxygenases, Drug Metab Dispos. 28 (2000) 1083–1086.

[51] T. Fukami, A. Iida, K. Konishi, M. Nakajima, Human arylacetamide deacetylase hydrolyzes ketoconazole to trigger hepatocellular toxicity, Biochemical Pharmacology. 116 (2016) 153–161. https://doi.org/10.1016/j.bcp.2016.07.007.

[52] K.A. Usmani, W.G. Chen, A.J.M. Sadeque, Identification of Human Cytochrome P450 and Flavin-Containing Monooxygenase Enzymes Involved in the Metabolism of Lorcaserin, a Novel Selective Human 5-Hydroxytryptamine 2C Agonist, Drug Metab Dispos. 40 (2012) 761–771. https://doi.org/10.1124/dmd.111.043414.

[53] Y.-M. Kim, Estimation of Human Flavin-containing Monooxygenases Activity(FMO1) in the Baculovirus Expression Vector System by using S-oxidation of Methimazole, Journal of Food Hygiene and Safety. 14 (1999) 415–421.

[54] B.V. Karanam, C.J. Welch, V.G. Reddy, J. Chilenski, M. Biba, S. Vincent, Species Differential Stereoselective Oxidation of a Methylsulfide Metabolite of Mk-0767 [(±)-5-[(2,4-

Dioxothiazolidin-5-Yl)methyl]-2-Methoxy-N-[[(4-Trifluoromethyl)phenyl]methyl]benzamide], a Peroxisome Proliferator-Activated Receptor Dual Agonist, Drug Metab Dispos. 32 (2004) 1061–1068. https://doi.org/10.1124/dmd.104.000224.

[55] C.L. Shaffer, M. Gunduz, R.J. Scialis, A.F. Fang, Metabolism and Disposition of a Selective α7 Nicotinic Acetylcholine Receptor Agonist in Humans, Drug Metab Dispos. 35 (2007) 1188–1195. https://doi.org/10.1124/dmd.106.014449.

[56] S.K. Lee, M.J. Kang, C. Jin, M.K. In, D.-H. Kim, H.H. Yoo, Flavin-containing monooxygenase 1-catalysed N,N-dimethylamphetamine N-oxidation, Xenobiotica. 39 (2009) 680–686. https://doi.org/10.1080/00498250902998699.

[57] J. Yu, D.G. Brown, D. Burdette, In Vitro Metabolism Studies of Nomifensine Monooxygenation Pathways: Metabolite Identification, Reaction Phenotyping, and Bioactivation Mechanism, Drug Metab Dispos. 38 (2010) 1767–1778. https://doi.org/10.1124/dmd.110.033910.

[58] R.C.A. Onderwater, A.E. Rettie, J.N.M. Commandeur, N.P.E. Vermeulen, Bioactivation of N-substituted N′-(4-imidazole-ethyl)thioureas by human FMO1 and FMO3, Xenobiotica. 36 (2006) 645–657. https://doi.org/10.1080/00498250500354329.

[59] J. Kajita, K. Inano, E. Fuse, T. Kuwabara, H. Kobayashi, Effects of Olopatadine, a New Antiallergic Agent, on Human Liver Microsomal Cytochrome P450 Activities, Drug Metab Dispos. 30 (2002) 1504–1511. https://doi.org/10.1124/dmd.30.12.1504.

[60] F. Li, A.D. Patterson, K.W. Krausz, B. Dick, F.J. Frey, F.J. Gonzalez, J.R. Idle, Metabolomics reveals the metabolic map of procainamide in humans and mice, Biochemical Pharmacology. 83 (2012) 1435–1444. https://doi.org/10.1016/j.bcp.2012.02.013.

[61] M. Miura, T. Ohkubo, In vitro metabolism of quazepam in human liver and intestine and assessment of drug interactions, Xenobiotica. 34 (2004) 1001–1011. https://doi.org/10.1080/02772240400015214.

[62] R.J. Krause, L.H. Lash, A.A. Elfarra, Human Kidney Flavin-Containing Monooxygenases and Their Potential Roles in Cysteine S-Conjugate Metabolism and Nephrotoxicity, J Pharmacol Exp Ther. 304 (2003) 185–191. https://doi.org/10.1124/jpet.102.042911.

[63] X. Hai, T. Nauwelaers, R. Busson, E. Adams, J. Hoogmartens, A. Van Schepdael, A rapid and sensitive CE method with field-enhanced sample injection and in-capillary derivatization for selenomethionine metabolism catalyzed by flavin-containing monooxygenases, ELECTROPHORESIS. 31 (2010) 3352–3361. https://doi.org/10.1002/elps.201000248.

[64] R.J. Krause, S.C. Glocke, A.R. Sicuri, S.L. Ripp, A.A. Elfarra, Oxidative Metabolism of Seleno-l-methionine to l-Methionine Selenoxide by Flavin-Containing Monooxygenases, Chem. Res. Toxicol. 19 (2006) 1643–1649. https://doi.org/10.1021/tx0601915.

[65] M.G. Pike, D.C. Mays, D.W. Macomber, J.J. Lipsky, Metabolism of a Disulfiram Metabolite, S-MethylN,N-Diethyldithiocarbamate, by Flavin Monooxygenase in Human Renal Microsomes, Drug Metab Dispos. 29 (2001) 127–132.

[66] T. Washio, H. Arisawa, K. Kohsaka, H. Yasuda, Identification of Human Drug-Metabolizing Enzymes Involved in the Metabolism of SNI-2011, Biological and Pharmaceutical Bulletin. 24 (2001) 1263–1266. https://doi.org/10.1248/bpb.24.1263.

[67] D. Yeniceli, X. Deng, E. Adams, D. Dogrukol-Ak, A.V. Schepdael, Development of a CD-MEKC method for investigating the metabolism of tamoxifen by flavin-containing monooxygenases and the inhibitory effects of methimazole, nicotine and DMXAA, ELECTROPHORESIS. 34 (2013) 463–470. https://doi.org/10.1002/elps.201200356.

[68] S.K. Krueger, J.E. VanDyke, D.E. Williams, R.N. Hines, The Role of Flavin-Containing Monooxygenase (FMO) in the Metabolism of Tamoxifen and Other Tertiary Amines, Drug Metabolism Reviews. 38 (2006) 139–147. https://doi.org/10.1080/03602530600569919.

[69] P. Parte, D. Kupfer, Oxidation of tamoxifen by human flavin-containing monooxygenase (FMO) 1 and FMO3 to tamoxifen-N-oxide and its novel reduction back to tamoxifen by human cytochromes P450 and hemoglobin, Drug Metab Dispos. 33 (2005) 1446–1452. https://doi.org/10.1124/dmd.104.000802.

[70] M. Attar, D. Dong, K.-H.J. Ling, D.D.-S. Tang-Liu, Cytochrome P450 2C8 and Flavin-containing Monooxygenases are Involved in the Metabolism of Tazarotenic Acid in Humans, Drug Metab Dispos. 31 (2003) 476–481. https://doi.org/10.1124/dmd.31.4.476.

[71] A. Kousba, R. Soll, S. Yee, M. Martin, Cyclic Conversion of the Novel Src Kinase Inhibitor [7-(2,6-Dichloro-phenyl)-5-methyl-benzo[1,2,4]triazin-3-yl]-[4-(2-pyrrolidin-1-yl-ethoxy)-phenyl]-amine (TG100435) and Its N-Oxide Metabolite by Flavin-Containing Monoxygenases and Cytochrome P450 Reductase, Drug Metab Dispos. 35 (2007) 2242–2251. https://doi.org/10.1124/dmd.107.017384.

[72] M.C. Henderson, L.K. Siddens, S.K. Krueger, J.F. Stevens, K. Kedzie, W.K. Fang, T. Heidelbaugh, P. Nguyen, K. Chow, M. Garst, D. Gil, D.E. Williams, Flavin-containing monooxygenase S-oxygenation of a series of thioureas and thiones, Toxicology and Applied Pharmacology. 278 (2014) 91–99. https://doi.org/10.1016/j.taap.2014.04.002.

[73] R. Indra, P. Pompach, V. Martínek, P. Takácsová, K. Vavrová, Z. Heger, V. Adam, T. Eckschlager, K. Kopečková, V.M. Arlt, M. Stiborová, Identification of Human Enzymes Oxidizing the Anti-Thyroid-Cancer Drug Vandetanib and Explanation of the High Efficiency of Cytochrome P450 3A4 in its Oxidation, International Journal of Molecular Sciences. 20 (2019) 3392. https://doi.org/10.3390/ijms20143392.

[74] R. Indra, P. Pompach, K. Vavrová, K. Jáklová, Z. Heger, V. Adam, T. Eckschlager, K. Kopečková, V.M. Arlt, M. Stiborová, Cytochrome P450 and flavin-containing monooxygenase enzymes are responsible for differential oxidation of the anti-thyroid-cancer drug vandetanib by human and rat hepatic microsomal systems, Environmental Toxicology and Pharmacology. 74 (2020) 103310. https://doi.org/10.1016/j.etap.2019.103310.

[75] S.B. Yanni, P.P. Annaert, P. Augustijns, A. Bridges, Y. Gao, D.K. Benjamin, D.R. Thakker, Role of Flavin-Containing Monooxygenase in Oxidative Metabolism of Voriconazole by Human Liver Microsomes, Drug Metab Dispos. 36 (2008) 1119–1125. https://doi.org/10.1124/dmd.107.019646.

[76] B.J. Ring, S.A. Wrighton, S.L.K. Aldridge, K. Hansen, B. Haehner, L.A. Shipley, Flavin-Containing Monooxygenase-MediatedN-Oxidation of the M1-Muscarinic Agonist Xanomeline, Drug Metab Dispos. 27 (1999) 1099–1103.

[77] R. Langreth, M. Waldholz, New Era of Personalized Medicine: Targeting Drugs For Each Unique Genetic Profile, The Oncologist. 4 (1999) 426–427. https://doi.org/10.1634/theoncologist.4-5-426.

[78] I.S. Chan, G.S. Ginsburg, Personalized Medicine: Progress and Promise, Annual Review of Genomics and Human Genetics. 12 (2011) 217–244. https://doi.org/10.1146/annurev-genom-082410-101446.

[79] N.O. Peneş, B. Weber, S.D. Păun, Role of genetic polymorphism in nutritional supplementation therapy in personalized medicine, Rom J Morphol Embryol. 58 (2017) 53–58.

[80] A. Stenzinger, A. Edsjö, C. Ploeger, M. Friedman, S. Fröhling, V. Wirta, T. Seufferlein, J. Botling, J. Duyster, M. Akhras, R. Thimme, T. Fioretos, M. Bitzer, L. Cavelier, P. Schirmacher, N. Malek, R. Rosenquist, A. Lindstrand, A. Wedell, D. Gisselsson, E. Melén, G. Helenius, H.

Ehrencrona, L. Engstrand, L. Palmqvist, L.-Å. Levin, L. Lovmar, M. Landström, M. Hallbeck, M. Wadelius, P. Sikora, A.J. Beer, A.L. Illert, J. Budczies, K. Nikolaou, O. Kohlbacher, P. Horak, P. Kuhn, C. Schroeder, M. Boerries, S. Lassmann, V.I. Gaidzik, Trailblazing precision medicine in Europe: A joint view by Genomic Medicine Sweden and the Centers for Personalized Medicine, ZPM, in Germany, Seminars in Cancer Biology. 84 (2022) 242–254. https://doi.org/10.1016/j.semcancer.2021.05.026.

[81] D.E. Pritchard, F. Moeckel, M.S. Villa, L.T. Housman, C.A. McCarty, H.L. McLeod, Strategies for integrating personalized medicine into healthcare practice, Personalized Medicine. 14 (2017) 141–152. https://doi.org/10.2217/pme-2016-0064.

[82] P.H. Özdinler, Expanded access: opening doors to personalized medicine for rare disease patients and patients with neurodegenerative diseases, The FEBS Journal. 288 (2021) 1457–1461. https://doi.org/10.1111/febs.15529.

[83] J.L. Mega, M.S. Sabatine, E.M. Antman, Population and Personalized Medicine in the Modern Era, JAMA. 312 (2014) 1969–1970. https://doi.org/10.1001/jama.2014.15224.

[84] R.T. Williams, Hepatic metabolism of drugs., Gut. 13 (1972) 579–585.

[85] B.S.P. P.B. Danielson, The Cytochrome P450 Superfamily: Biochemistry, Evolution and Drug Metabolism in Humans, Current Drug Metabolism. 3 (2005) 561–597. https://doi.org/10.2174/1389200023337054.

[86] U.M. Zanger, M. Schwab, Cytochrome P450 enzymes in drug metabolism: Regulation of gene expression, enzyme activities, and impact of genetic variation, Pharmacology & Therapeutics. 138 (2013) 103–141. https://doi.org/10.1016/j.pharmthera.2012.12.007.

[87] D.M. Ziegler, Flavin-containing monooxygenases: Catalytic mechanism and substrate specificities, Drug Metabolism Reviews. 19 (1988) 1–32. https://doi.org/10.3109/03602538809049617.

[88] S.J. Sadeghi, R. Meirinhos, G. Catucci, V.R. Dodhia, G. Di Nardo, G. Gilardi, Direct electrochemistry of drug metabolizing human flavin-containing monooxygenase: Electrochemical turnover of benzydamine and tamoxifen, Journal of the American Chemical Society. 132 (2010) 458–459. https://doi.org/10.1021/ja909261p.

[89] C. Baj-Rossi, G.D. Micheli, S. Carrara, Electrochemical Detection of Anti-Breast-Cancer Agents in Human Serum by Cytochrome P450-Coated Carbon Nanotubes, Sensors. 12 (2012) 6520–6537. https://doi.org/10.3390/s120506520.

[90] R.F.I. Ajay, S. Tshoko, Y. Mgwili, S. Nqunqa, T. Mulaudzi, N. Mayedwa, E. Iwuoha, Green method synthesised graphene-silver electrochemical nanobiosensors for ethambutol and pyrazinamide, Processes. 8 (2020). https://doi.org/10.3390/pr8070879.

[91] C. Franke, R.F. Ajayi, O. Uhuo, K. Januarie, E. Iwuoha, Metallodendrimer-sensitised cytochrome P450 3A4 electrochemical biosensor for TB drugs, Electroanalysis. (2020) 1–12. https://doi.org/10.1002/elan.202060384.

[92] I. Willner, E. Katz, Integration of layered redox proteins and conductive supports for bioelectronic applications, Angewandte Chemie - International Edition. 39 (2000) 1180–1218. https://doi.org/10.1002/(sici)1521-3773(20000403)39:7<1180::aid-anie1180>3.0.co;2-e.

[93] R.C. Alkire, P.N. Bartlett, J. Lipkowski, Nanopatterned and Nanoparticle-Modified Electrodes, John Wiley & Sons, 2017.

[94] M. Pumera, Graphene in biosensing, Materials Today. 14 (2011) 308–315. https://doi.org/10.1016/S1369-7021(11)70160-2.

[95] M. Pumera, Electrochemistry of graphene, graphene oxide and other graphenoids: Review, Electrochemistry Communications. 36 (2013) 14–18. https://doi.org/10.1016/j.elecom.2013.08.028.

[96] J. Wang, Electrochemical biosensing based on noble metal nanoparticles, Microchimica Acta. 177 (2012) 245–270. https://doi.org/10.1007/s00604-011-0758-1.

[97] S. Carrara, C. Baj-Rossi, C. Boero, G. De Micheli, Do Carbon Nanotubes contribute to Electrochemical Biosensing?, Electrochimica Acta. 128 (2014) 102–112. https://doi.org/10.1016/j.electacta.2013.12.123.

[98] A.M. Md Jani, D. Losic, N.H. Voelcker, Nanoporous anodic aluminium oxide: Advances in surface engineering and emerging applications, Progress in Materials Science. 58 (2013) 636–704. https://doi.org/10.1016/j.pmatsci.2013.01.002.

[99] J. Lu, H. Li, D. Cui, Y. Zhang, S. Liu, Enhanced enzymatic reactivity for electrochemically driven drug metabolism by confining cytochrome P450 enzyme in TiO2 nanotube arrays, Analytical Chemistry. 86 (2014) 8003–8009. https://doi.org/10.1021/ac502234x.

[100] J. Vacek, M. Zatloukalova, D. Novak, Electrochemistry of membrane proteins and protein–lipid assemblies, Current Opinion in Electrochemistry. 12 (2018) 73–80. https://doi.org/10.1016/j.coelec.2018.04.012.

[101] K. Mitsubayashi, Y. Hashimoto, Bioelectronic nose for methyl mercaptan vapor using xenobiotic metabolizing enzyme: Flavin-containing monooxygenase, in: Sensors and Actuators, B: Chemical, Elsevier, 2002: pp. 35–40. https://doi.org/10.1016/S0925-4005(01)01025-5.

[102] K. Mitsubayashi, Y. Kubotera, K. Yano, Y. Hashimoto, T. Kon, S. Nakakura, Y. Nishi, H. Endo, Trimethylamine biosensor with flavin-containing monooxygenase type 3 (FMO3) for fish-freshness analysis, in: Sensors and Actuators, B: Chemical, Elsevier, 2004: pp. 463–467. https://doi.org/10.1016/j.snb.2004.05.006.

[103] H. Saito, Y. Kaneko, Y. Hashimoto, T. Shirai, H. Kudo, K. Otsuka, K. Mitsubayashi, Ammonia bio-sniffer with flavin-containing monooxygenase, Sensors and Actuators B: Chemical. 123 (2007) 877–881. https://doi.org/10.1016/j.snb.2006.10.045.

[104] H. Saito, T. Shirai, H. Kudo, K. Mitsubayashi, Electrochemical sensor with flavin-containing monooxygenase for triethylamine solution, in: Analytical and Bioanalytical Chemistry, Springer, 2008: pp. 1263–1268. https://doi.org/10.1007/s00216-007-1806-x.

[105] C. Fillit, N. Jaffrezic-Renault, F. Bessueille, D. Leonard, K. Mitsubayashi, J. Tardy, Development of a microconductometric biosniffer for detection of trimethylamine, Materials Science and Engineering: C. 28 (2008) 781–786. https://doi.org/10.1016/j.msec.2007.10.020.

[106] S. Castrignanò, S.J. Sadeghi, G. Gilardi, Electro-catalysis by immobilised human flavin-containing monooxygenase isoform 3 (hFMO3), Anal Bioanal Chem. 398 (2010) 1403–1409. https://doi.org/10.1007/s00216-010-4014-z.

[107] S. Bourigua, S. El Ichi, H. Korri-Youssoufi, A. Maaref, S. Dzyadevych, N. Jaffrezic Renault, Electrochemical sensing of trimethylamine based on polypyrrole–flavin-containing monooxygenase (FMO3) and ferrocene as redox probe for evaluation of fish freshness, Biosensors and Bioelectronics. 28 (2011) 105–111. https://doi.org/10.1016/j.bios.2011.07.005.

[108] M. Ikegami, Y. Mie, Y. Hirano, Y. Komatsu, Direct electrochemistry of microsomal human flavin-containing monooxygenases 1 and 3 on naphthalenethiol thin films, ECS Electrochemistry Letters. 2 (2013) 2013–2015. https://doi.org/10.1149/2.003312eel.

[109] S. Castrignanò, S.J. Sadeghi, G. Gilardi, Entrapment of human flavin-containing monooxygenase 3 in the presence of gold nanoparticles: TEM, FTIR and electrocatalysis,

Biochimica et Biophysica Acta (BBA) - General Subjects. 1820 (2012) 2072–2078. https://doi.org/10.1016/j.bbagen.2012.09.017.

[110] S. Castrignanò, G. Gilardi, S.J. Sadeghi, Human flavin-containing monooxygenase 3 on graphene oxide for drug metabolism screening, Analytical Chemistry. 87 (2015) 2974–2980. https://doi.org/10.1021/ac504535y.

[111] S. Castrignanò, S. Bortolussi, G. Catucci, O. Gholami, F. Valetti, G. Gilardi, S.J. Sadeghi, Bioelectrochemical profiling of two common polymorphic variants of human FMO3 in presence of graphene oxide, Electrochimica Acta. 228 (2017) 611–618. https://doi.org/10.1016/j.electacta.2017.01.131.

[112] S. Miller, R. Hille, B. Palfey, FLAVINS and FLAVOPROTEINS 2011, Lulu.com, 2013.

[113] X. Xu, G. Bai, L. Song, Q. Zheng, Y. Yao, S. Liu, C. Yao, Fast steroid hormone metabolism assays with electrochemical liver microsomal bioreactor based on polydopamine encapsulated gold-graphene nanocomposite, Electrochimica Acta. 258 (2017) 1365–1374. https://doi.org/10.1016/j.electacta.2017.11.195.

[114] R. Nerimetla, G. Premaratne, H. Liu, S. Krishnan, Improved electrocatalytic metabolite production and drug biosensing by human liver microsomes immobilized on amine-functionalized magnetic nanoparticles, Electrochimica Acta. 280 (2018) 101–107. https://doi.org/10.1016/j.electacta.2018.05.085.

[115] E.A. Shephard, C.T. Dolphin, M.F. Fox, S. Povey, R. Smith, I.R. Phillips, Localization of Genes Encoding Three Distinct Flavin-Containing Monooxygenases to Human Chromosome 1q, Genomics. 16 (1993) 85–89. https://doi.org/10.1006/geno.1993.1144.

[116] C.K. Yeung, D.H. Lang, K.E. Thummel, A.E. Rettie, Immunoquantitation of FMO1 in Human Liver, Kidney, and Intestine, Drug Metab Dispos. 28 (2000) 1107–1111.

[117] Y.M. Kim, D.M. Ziegler, Size Limits of Thiocarbamides Accepted as Substrates by Human Flavin-Containing Monooxygenase 1, Drug Metab Dispos. 28 (2000) 1003–1006.

[118] J. Dong, T.D. Porter, Coexpression of Mammalian Cytochrome P450 and Reductase inEscherichia coli, Archives of Biochemistry and Biophysics. 327 (1996) 254–259. https://doi.org/10.1006/abbi.1996.0118.

[119] P.J. Sabourin, B.P. Smyser, E. Hodgson, Purification of the flavin-containing monooxygenase from mouse and pig liver microsomes, Int J Biochem. 16 (1984) 713–720. https://doi.org/10.1016/0020-711x(84)90180-0.

[120] A. Micsonai, F. Wien, L. Kernya, Y.-H. Lee, Y. Goto, M. Réfrégiers, J. Kardos, Accurate secondary structure prediction and fold recognition for circular dichroism spectroscopy, PNAS. 112 (2015) E3095–E3103. https://doi.org/10.1073/pnas.1500851112.

[121] G. Catucci, D. Aramini, S.J. Sadeghi, G. Gilardi, Ligand stabilization and effect on unfolding by polymorphism in human flavin-containing monooxygenase 3, International Journal of Biological Macromolecules. 162 (2020) 1484–1493. https://doi.org/10.1016/j.ijbiomac.2020.08.032.

[122] S.G. Ramalli, A.J. Miles, R.W. Janes, B.A. Wallace, The PCDDB (Protein Circular Dichroism Data Bank): A Bioinformatics Resource for Protein Characterisations and Methods Development, Journal of Molecular Biology. 434 (2022) 167441. https://doi.org/10.1016/j.jmb.2022.167441.

[123] L. Mavridis, R.W. Janes, PDB2CD: a web-based application for the generation of circular dichroism spectra from protein atomic coordinates, Bioinformatics. 33 (2017) 56–63. https://doi.org/10.1093/bioinformatics/btw554.

[124] A. Micsonai, É. Bulyáki, J. Kardos, BeStSel: From Secondary Structure Analysis to Protein Fold Prediction by Circular Dichroism Spectroscopy, in: Y.W. Chen, C.-P.B. Yiu (Eds.), Structural Genomics: General Applications, Springer US, New York, NY, 2021: pp. 175–189. https://doi.org/10.1007/978-1-0716-0892-0_11.

[125] A. Micsonai, F. Wien, É. Bulyáki, J. Kun, É. Moussong, Y.-H. Lee, Y. Goto, M. Réfrégiers, J. Kardos, BeStSel: a web server for accurate protein secondary structure prediction and fold recognition from the circular dichroism spectra, Nucleic Acids Res. 46 (2018) W315–W322. https://doi.org/10.1093/nar/gky497.

[126] C. Gao, G. Catucci, S. Castrignanò, G. Gilardi, S.J. Sadeghi, Inactivation mechanism of N61S mutant of human FMO3 towards trimethylamine, Scientific Reports. 7 (2017) 14668. https://doi.org/10.1038/s41598-017-15224-9.

[127] C. Orengo, A. Michie, S. Jones, D. Jones, M. Swindells, J. Thornton, CATH – a hierarchic classification of protein domain structures, Structure. 5 (1997) 1093–1109. https://doi.org/10.1016/S0969-2126(97)00260-8.

[128] M. Krzek, M. Fraaije, Review on human FMO3: topology and recombinant production in Escherichia coli, in: 2017: pp. 77–104.

[129] A. Alfieri, E. Malito, R. Orru, M.W. Fraaije, A. Mattevi, Revealing the moonlighting role of NADP in the structure of a flavin-containing monooxygenase, PNAS. 105 (2008) 6572–6577. https://doi.org/10.1073/pnas.0800859105.

[130] G. Catucci, I. Polignano, D. Cusumano, C. Medana, G. Gilardi, S.J. Sadeghi, Identification of human flavin-containing monooxygenase 3 substrates by a colorimetric screening assay, Analytical Biochemistry. 522 (2017) 46–52. https://doi.org/10.1016/j.ab.2017.01.024.

[131] G. Catucci, G. Gilardi, S.J. Sadeghi, Production of drug metabolites by human FMO3 in Escherichia coli, Microbial Cell Factories. 19 (2020) 74. https://doi.org/10.1186/s12934-020-01332-1.

[132] L. Wang, L.J. Christopher, D. Cui, W. Li, R. Iyer, W.G. Humphreys, D. Zhang, Identification of the Human Enzymes Involved in the Oxidative Metabolism of Dasatinib: An Effective Approach for Determining Metabolite Formation Kinetics, Drug Metab Dispos. 36 (2008) 1828–1839. https://doi.org/10.1124/dmd.107.020255.

[133] A.V. Kamath, J. Wang, F.Y. Lee, P.H. Marathe, Preclinical pharmacokinetics and in vitro metabolism of dasatinib (BMS-354825): a potent oral multi-targeted kinase inhibitor against SRC and BCR-ABL, Cancer Chemother Pharmacol. 61 (2008) 365–376. https://doi.org/10.1007/s00280-007-0478-8.

[134] A. Weil, P. Martin, R. Smith, S. Oliver, P. Langmuir, J. Read, K.-H. Molz, Pharmacokinetics of Vandetanib in Subjects with Renal or Hepatic Impairment, Clin Pharmacokinet. 49 (2010) 607–618. https://doi.org/10.2165/11534330-000000000-00000.

[135] P. Martin, S. Oliver, S.-J. Kennedy, E. Partridge, M. Hutchison, D. Clarke, P. Giles, Pharmacokinetics of Vandetanib: Three Phase I Studies in Healthy Subjects, Clinical Therapeutics. 34 (2012) 221–237. https://doi.org/10.1016/j.clinthera.2011.11.011.

[136] A. Dixit, T.E. Roche, Spectrophotometric assay of the flavin-containing monooxygenase and changes in its activity in female mouse liver with nutritional and diurnal conditions, Archives of Biochemistry and Biophysics. 233 (1984) 50–63. https://doi.org/10.1016/0003-9861(84)90600-3.

[137] P.R. Ortiz de Montellano, ed., Cytochrome P450, Springer US, Boston, MA, 2005. https://doi.org/10.1007/b139087.

[138] J.R. Cashman, J. Zhang, Human Flavin-Containing Monooxygenases, Annual Review of Pharmacology and Toxicology. 46 (2006) 65–100. https://doi.org/10.1146/annurev.pharmtox.46.120604.141043.

[139] J. Rittle, M.T. Green, Cytochrome P450 Compound I: Capture, Characterization, and C-H Bond Activation Kinetics, Science. 330 (2010) 933–937. https://doi.org/10.1126/science.1193478.

[140] S. Nagano, J.R. Cupp-Vickery, T.L. Poulos, Crystal Structures of the Ferrous Dioxygen Complex of Wild-type Cytochrome P450eryF and Its Mutants, A245S and A245T: INVESTIGATION OF THE PROTON TRANSFER SYSTEM IN P450eryF *, Journal of Biological Chemistry. 280 (2005) 22102–22107. https://doi.org/10.1074/jbc.M501732200.

[141] I. Schlichting, J. Berendzen, K. Chu, A.M. Stock, S.A. Maves, D.E. Benson, R.M. Sweet, D. Ringe, G.A. Petsko, S.G. Sligar, The Catalytic Pathway of Cytochrome P450cam at Atomic Resolution, Science. 287 (2000) 1615–1622. https://doi.org/10.1126/science.287.5458.1615.

[142] R. Orru, D.E.T. Pazmiño, M.W. Fraaije, A. Mattevi, Joint Functions of Protein Residues and NADP(H) in Oxygen Activation by Flavin-containing Monooxygenase *, Journal of Biological Chemistry. 285 (2010) 35021–35028. https://doi.org/10.1074/jbc.M110.161372.

[143] N.B. Beaty, D.P. Ballou, The oxidative half-reaction of liver microsomal FAD-containing monooxygenase, J. Biol. Chem. 256 (1981) 4619–4625.

[144] N.B. Beaty, D.P. Ballou, The reductive half-reaction of liver microsomal FAD-containing monooxygenase, J. Biol. Chem. 256 (1981) 4611–4618.

[145] K.C. Jones, D.P. Ballou, Reactions of the 4a-hydroperoxide of liver microsomal flavin-containing monooxygenase with nucleophilic and electrophilic substrates, J. Biol. Chem. 261 (1986) 2553–2559.

[146] L.K. Siddens, S.K. Krueger, M.C. Henderson, D.E. Williams, Mammalian flavin-containing monooxygenase (FMO) as a source of hydrogen peroxide, Biochemical Pharmacology. 89 (2014) 141–147. https://doi.org/10.1016/j.bcp.2014.02.006.

[147] E.J. Rauckman, G.M. Rosen, B.B. Kitchell, Superoxide Radical as an Intermediate in the Oxidation of Hydroxylamines by Mixed Function Amine Oxidase, Mol Pharmacol. 15 (1979) 131–137.

[148] D.M. Ziegler, F.H. Pettit, Formation of an intermediate N-oxide in the oxidative demethylation of N,N-dimethylaniline catalyzed by liver microsomes, Biochemical and Biophysical Research Communications. 15 (1964) 188–193. https://doi.org/10.1016/0006-291X(64)90322-5.

[149] J. Zhang, J.R. Cashman, QUANTITATIVE ANALYSIS OF FMO GENE mRNA LEVELS IN HUMAN TISSUES, Drug Metab Dispos. 34 (2006) 19–26. https://doi.org/10.1124/dmd.105.006171.

[150] I.R. Phillips, E.A. Shephard, Flavin-containing monooxygenases: mutations, disease and drug response, Trends Pharmacol Sci. 29 (2008) 294–301. https://doi.org/10.1016/j.tips.2008.03.004.

[151] R.N. Hines, Developmental and tissue-specific expression of human flavin-containing monooxygenases 1 and 3, Expert Opinion on Drug Metabolism & Toxicology. 2 (2006) 41–49. https://doi.org/10.1517/17425255.2.1.41.

[152] G. Catucci, A. Occhipinti, M. Maffei, G. Gilardi, S.J. Sadeghi, Effect of Human Flavin-Containing Monooxygenase 3 Polymorphism on the Metabolism of Aurora Kinase Inhibitors, International Journal of Molecular Sciences. 14 (2013) 2707–2716. https://doi.org/10.3390/ijms14022707.

[153] G.L. Rosano, E.A. Ceccarelli, Recombinant protein expression in Escherichia coli: advances and challenges, Front Microbiol. 5 (2014) 172. https://doi.org/10.3389/fmicb.2014.00172.

[154] G. Catucci, S.J. Sadeghi, G. Gilardi, A direct time-based ITC approach for substrate turnover measurements demonstrated on human FMO3, Chem Commun (Camb). 55 (2019) 6217–6220. https://doi.org/10.1039/c9cc01356c.

[155] C.R. Nicoll, G. Bailleul, F. Fiorentini, M.L. Mascotti, M.W. Fraaije, A. Mattevi, Ancestral-sequence reconstruction unveils the structural basis of function in mammalian FMOs, Nat Struct Mol Biol. 27 (2020) 14–24. https://doi.org/10.1038/s41594-019-0347-2.

[156] E. Romero, R. Robinson, P. Sobrado, Monitoring the reductive and oxidative half-reactions of a flavin-dependent monooxygenase using stopped-flow spectrophotometry, J Vis Exp. (2012). https://doi.org/10.3791/3803.

[157] H. Shi, G. Timmins, M. Monske, A. Burdick, B. Kalyanaraman, Y. Liu, J.-L. Clément, S. Burchiel, K.J. Liu, Evaluation of spin trapping agents and trapping conditions for detection of cell-generated reactive oxygen species, Archives of Biochemistry and Biophysics. 437 (2005) 59–68. https://doi.org/10.1016/j.abb.2005.02.028.

[158] C. Frejaville, H. Karoui, B. Tuccio, F.L. Moigne, M. Culcasi, S. Pietri, R. Lauricella, P. Tordo, 5-(Diethoxyphosphoryl)-5-methyl-1-pyrroline N-oxide: A New Efficient Phosphorylated Nitrone for the in Vitro and in Vivo Spin Trapping of Oxygen-Centered Radicals, J. Med. Chem. 38 (1995) 258–265. https://doi.org/10.1021/jm00002a007.

[159] I. Mahmood, S.R. Imadi, K. Shazadi, A. Gul, K.R. Hakeem, Effects of Pesticides on Environment, in: K.R. Hakeem, M.S. Akhtar, S.N.A. Abdullah (Eds.), Plant, Soil and Microbes: Volume 1: Implications in Crop Science, Springer International Publishing, Cham, 2016: pp. 253–269. https://doi.org/10.1007/978-3-319-27455-3_13.

[160] R. Betarbet, T.B. Sherer, G. MacKenzie, M. Garcia-Osuna, A.V. Panov, J.T. Greenamyre, Chronic systemic pesticide exposure reproduces features of Parkinson's disease, Nature Neuroscience. 3 (2000) 1301–1306. https://doi.org/10.1038/81834.

[161] A. Ascherio, H. Chen, M.G. Weisskopf, E. O'Reilly, M.L. McCullough, E.E. Calle, M.A. Schwarzschild, M.J. Thun, Pesticide exposure and risk for Parkinson's disease, Annals of Neurology. 60 (2006) 197–203. https://doi.org/10.1002/ana.20904.

[162] van der Mark Marianne, Brouwer Maartje, Kromhout Hans, Nijssen Peter, Huss Anke, Vermeulen Roel, Is Pesticide Use Related to Parkinson Disease? Some Clues to Heterogeneity in Study Results, Environmental Health Perspectives. 120 (2012) 340–347. https://doi.org/10.1289/ehp.1103881.

[163] J.R. Voorhees, M.T. Remy, C.M. Erickson, L.M. Dutca, D.J. Brat, A.A. Pieper, Occupational-like organophosphate exposure disrupts microglia and accelerates deficits in a rat model of Alzheimer's disease, Npj Aging and Mechanisms of Disease. 5 (2019) 1–14. https://doi.org/10.1038/s41514-018-0033-3.

[164] K.M. Hayden, M.C. Norton, D. Darcey, T. Østbye, P.P. Zandi, J.C.S. Breitner, K.A. Welsh-Bohmer, Occupational exposure to pesticides increases the risk of incident AD: The Cache County Study, Neurology. 74 (2010) 1524–1530. https://doi.org/10.1212/WNL.0b013e3181dd4423.

[165] J.R. Richardson, A. Roy, S.L. Shalat, R.T. von Stein, M.M. Hossain, B. Buckley, M. Gearing, A.I. Levey, D.C. German, Elevated Serum Pesticide Levels and Risk for Alzheimer Disease, JAMA Neurology. 71 (2014) 284–290. https://doi.org/10.1001/jamaneurol.2013.6030.

[166] M.C. Henderson, S.K. Krueger, L.K. Siddens, J.F. Stevens, D.E. Williams, S-Oxygenation of the thioether organophosphate insecticides phorate and disulfoton by human lung flavin-containing monooxygenase 2, Biochemical Pharmacology. 68 (2004) 959–967. https://doi.org/10.1016/j.bcp.2004.05.051.

[167] Hodgson E, Levi P E, Pesticides: an important but underused model for the environmental health sciences., Environmental Health Perspectives. 104 (1996) 97–106. https://doi.org/10.1289/ehp.96104s197.

[168] I.G. Denisov, T.M. Makris, S.G. Sligar, I. Schlichting, Structure and Chemistry of Cytochrome P450, Chem. Rev. 105 (2005) 2253–2278. https://doi.org/10.1021/cr0307143.

[169] W.C. Dauterman, Biological and nonbiological modifications of organophosphorus compounds, Bull World Health Organ. 44 (1971) 133–150.

[170] S.J. Sadeghi, S. Ferrero, G. Di Nardo, G. Gilardi, Drug–drug interactions and cooperative effects detected in electrochemically driven human cytochrome P450 3A4, Bioelectrochemistry. 86 (2012) 87–91. https://doi.org/10.1016/j.bioelechem.2012.02.010.

[171] S.J. Sadeghi, A. Fantuzzi, G. Gilardi, Breakthrough in P450 bioelectrochemistry and future perspectives, Biochimica et Biophysica Acta (BBA) - Proteins and Proteomics. 1814 (2011) 237–248. https://doi.org/10.1016/j.bbapap.2010.07.010.

[172] P. Panicco, S. Castrignanò, S.J. Sadeghi, G.D. Nardo, G. Gilardi, Engineered human CYP2C9 and its main polymorphic variants for bioelectrochemical measurements of catalytic response, Bioelectrochemistry. 138 (2021) 107729. https://doi.org/10.1016/j.bioelechem.2020.107729.

[173] H. Cheropkina, G. Catucci, A. Marucco, I. Fenoglio, G. Gilardi, S.J. Sadeghi, Human flavin-containing monooxygenase 1 and its long-sought hydroperoxyflavin intermediate, Biochemical Pharmacology. 193 (2021) 114763. https://doi.org/10.1016/j.bcp.2021.114763.

[174] G. Catucci, I. Polignano, D. Cusumano, C. Medana, G. Gilardi, S.J. Sadeghi, Identification of human flavin-containing monooxygenase 3 substrates by a colorimetric screening assay, Analytical Biochemistry. 522 (2017) 46–52. https://doi.org/10.1016/j.ab.2017.01.024.

[175] F. Zheng, X.-Y. Yang, P.-Q. Bi, M.-S. Niu, C.-K. Lv, L. Feng, X.-T. Hao, K. P. Ghiggino, Improved compatibility of DDAB-functionalized graphene oxide with a conjugated polymer by isocyanate treatment, RSC Advances. 7 (2017) 17633–17639. https://doi.org/10.1039/C6RA28652F.

[176] D. Degregorio, S. D'Avino, S. Castrignanò, G. Di Nardo, S.J. Sadeghi, G. Catucci, G. Gilardi, Human Cytochrome P450 3A4 as a Biocatalyst: Effects of the Engineered Linker in Modulation of Coupling Efficiency in 3A4-BMR Chimeras, Frontiers in Pharmacology. 8 (2017). https://www.frontiersin.org/articles/10.3389/fphar.2017.00121 (accessed October 9, 2022).

[177] V.R. Dodhia, C. Sassone, A. Fantuzzi, G.D. Nardo, S.J. Sadeghi, G. Gilardi, Modulating the coupling efficiency of human cytochrome P450 CYP3A4 at electrode surfaces through protein engineering, Electrochemistry Communications. 10 (2008) 1744–1747. https://doi.org/10.1016/j.elecom.2008.09.007.

[178] T.R. Fukuto, Mechanism of action of organophosphorus and carbamate insecticides., Environmental Health Perspectives. 87 (1990) 245–254. https://doi.org/10.1289/ehp.9087245.

[179] F. Arduini, A. Amine, D. Moscone, G. Palleschi, Biosensors based on cholinesterase inhibition for insecticides, nerve agents and aflatoxin B1 detection (review), Microchim Acta. 170 (2010) 193–214. https://doi.org/10.1007/s00604-010-0317-1.

[180] COMMISSION IMPLEMENTING REGULATION (EU) 2019/ 1606 - of 27 September 2019 - concerning the non-renewal of the approval of the active substance methiocarb, in accordance with Regulation (EC) No 1107 / 2009 of the European Parliament and of the Council concerning the placing of plant protection products on the market, and amending the Annex to Commission Implementing Regulation (EU) No 540 / 2011, (n.d.) 3.

[181] P.E. Levi, E. Hodgson, Stereospecificity in the oxidation of phorate and phorate sulphoxide by purified FAD-containing mono-oxygenase and cytochrome P-450 isozymes, Xenobiotica. 18 (1988) 29–39. https://doi.org/10.3109/00498258809055134.

[182] C. Leoni, F.M. Buratti, E. Testai, The participation of human hepatic P450 isoforms, flavin-containing monooxygenases and aldehyde oxidase in the biotransformation of the insecticide fenthion, Toxicology and Applied Pharmacology. 233 (2008) 343–352. https://doi.org/10.1016/j.taap.2008.09.004.

[183] S. Castrignanò, S.J. Sadeghi, G. Gilardi, Electro-catalysis by immobilised human flavin-containing monooxygenase isoform 3 (hFMO3), in: Analytical and Bioanalytical Chemistry, Springer, 2010: pp. 1403–1409. https://doi.org/10.1007/s00216-010-4014-z.

[184] W.A. Khalil, H.H.A. Sherif, B.A. Hemdan, S.K.H. Khalil, W.E. Hotaby, Biocompatibility enhancement of graphene oxide-silver nanocomposite by functionalisation with polyvinylpyrrolidone, IET Nanobiotechnology. 13 (2019) 816–823. https://doi.org/10.1049/iet-nbt.2018.5321.

[185] D. Scarano, S. Bertarione, F. Cesano, G. Spoto, A. Zecchina, Imaging polycrystalline and smoke MgO surfaces with atomic force microscopy: a case study of high resolution image on a polycrystalline oxide, Surface Science. 570 (2004) 155–166. https://doi.org/10.1016/j.susc.2004.07.024.

[186] F.M. Borodich, X. Jin, A. Pepelyshev, Probabilistic, Fractal, and Related Techniques for Analysis of Engineering Surfaces, Frontiers in Mechanical Engineering. 6 (2020). https://www.frontiersin.org/articles/10.3389/fmech.2020.00064 (accessed October 18, 2022).

[187] B. Han, Y. Zhao, C. Ma, C. Wang, X. Tian, Y. Wang, W. Hu, P. Samorì, Asymmetric Chemical Functionalization of Top-Contact Electrodes: Tuning the Charge Injection for High-Performance MoS2 Field-Effect Transistors and Schottky Diodes, Advanced Materials. 34 (2022) 2109445. https://doi.org/10.1002/adma.202109445.

[188] J. Kim, L.J. Cote, F. Kim, W. Yuan, K.R. Shull, J. Huang, Graphene Oxide Sheets at Interfaces, J. Am. Chem. Soc. 132 (2010) 8180–8186. https://doi.org/10.1021/ja102777p.

[189] H.-W. Tien, Y.-L. Huang, S.-Y. Yang, S.-T. Hsiao, W.-H. Liao, H.-M. Li, Y.-S. Wang, J.-Y. Wang, C.-C.M. Ma, Preparation of transparent, conductive films by graphene nanosheet deposition on hydrophilic or hydrophobic surfaces through control of the pH value, J. Mater. Chem. 22 (2012) 2545–2552. https://doi.org/10.1039/C1JM14564A.

[190] S.-T. Hsiao, C.-C.M. Ma, W.-H. Liao, Y.-S. Wang, S.-M. Li, Y.-C. Huang, R.-B. Yang, W.-F. Liang, Lightweight and Flexible Reduced Graphene Oxide/Water-Borne Polyurethane Composites with High Electrical Conductivity and Excellent Electromagnetic Interference Shielding Performance, ACS Appl. Mater. Interfaces. 6 (2014) 10667–10678. https://doi.org/10.1021/am502412q.

[191] E. Laviron, L. Roullier, C. Degrand, A multilayer model for the study of space distributed redox modified electrodes: Part II. Theory and application of linear potential sweep voltammetry for a simple reaction, Journal of Electroanalytical Chemistry and Interfacial Electrochemistry. 112 (1980) 11–23. https://doi.org/10.1016/S0022-0728(80)80003-9.

[192] A. Fantuzzi, E. Capria, L.H. Mak, V.R. Dodhia, S.J. Sadeghi, S. Collins, G. Somers, E. Huq, G. Gilardi, An Electrochemical Microfluidic Platform for Human P450 Drug Metabolism Profiling, Anal. Chem. 82 (2010) 10222–10227. https://doi.org/10.1021/ac102480k.

[193] S. Benkhaya, S. M' rabet, A. El Harfi, A review on classifications, recent synthesis and applications of textile dyes, Inorganic Chemistry Communications. 115 (2020) 107891. https://doi.org/10.1016/j.inoche.2020.107891.

[194] K.-Y. Choi, A review of recent progress in the synthesis of bio-indigoids and their biologically assisted end-use applications, Dyes and Pigments. 181 (2020) 108570. https://doi.org/10.1016/j.dyepig.2020.108570.

[195] N. Stasiak, W. Kukuła-Koch, K. Głowniak, Modern industrial and pharmacological applications of indigo dye and its derivatives--a review, Acta Pol Pharm. 71 (2014) 215–221.

[196] T.M. Hsu, D.H. Welner, Z.N. Russ, B. Cervantes, R.L. Prathuri, P.D. Adams, J.E. Dueber, Employing a biochemical protecting group for a sustainable indigo dyeing strategy, Nat Chem Biol. 14 (2018) 256–261. https://doi.org/10.1038/nchembio.2552.

[197] C.B. Schimper, C. Ibanescu, T. Bechtold, Surface activation of dyed fabric for cellulase treatment, Biotechnology Journal. 6 (2011) 1280–1285. https://doi.org/10.1002/biot.201100002.

[198] N. Gaboriaud-Kolar, S. Nam, A.-L. Skaltsounis, A Colorful History: The Evolution of Indigoids, in: A.D. Kinghorn, H. Falk, J. Kobayashi (Eds.), Progress in the Chemistry of Organic Natural Products 99, Springer International Publishing, Cham, 2014: pp. 69–145. https://doi.org/10.1007/978-3-319-04900-7_2.

[199] H. Warzecha, A. Frank, M. Peer, E.M.J. Gillam, F.P. Guengerich, M. Unger, Formation of the indigo precursor indican in genetically engineered tobacco plants and cell cultures, Plant Biotechnology Journal. 5 (2007) 185–191. https://doi.org/10.1111/j.1467-7652.2006.00231.x.

[200] J. Song, H. Imanaka, K. Imamura, K. Kajitani, K. Nakanishi, Development of a highly efficient indigo dyeing method using indican with an immobilized β-glucosidase from Aspergillus niger, Journal of Bioscience and Bioengineering. 110 (2010) 281–287. https://doi.org/10.1016/j.jbiosc.2010.03.010.

[201] A.N. Fabara, M.W. Fraaije, An overview of microbial indigo-forming enzymes, Appl Microbiol Biotechnol. 104 (2020) 925–933. https://doi.org/10.1007/s00253-019-10292-5.

[202] S. Namgung, H.A. Park, J. Kim, P.-G. Lee, B.-G. Kim, Y.-H. Yang, K.-Y. Choi, Ecofriendly one-pot biosynthesis of indigo derivative dyes using CYP102G4 and PrnA halogenase, Dyes and Pigments. 162 (2019) 80–88. https://doi.org/10.1016/j.dyepig.2018.10.009.

[203] B.D. Ensley, B.J. Ratzkin, T.D. Osslund, M.J. Simon, L.P. Wackett, D.T. Gibson, Expression of Naphthalene Oxidation Genes in Escherichia coli Results in the Biosynthesis of Indigo, Science. 222 (1983) 167–169. https://doi.org/10.1126/science.6353574.

[204] D. Murdock, B.D. Ensley, C. Serdar, M. Thalen, Construction of Metabolic Operons Catalyzing the De Novo Biosynthesis of Indigo in Escherichia coli, Nat Biotechnol. 11 (1993) 381–386. https://doi.org/10.1038/nbt0393-381.

[205] K.E. O'Connor, S. Hartmans, Indigo formation by aromatic hydrocarbon-degrading bacteria, Biotechnology Letters. 20 (1998) 219–223. https://doi.org/10.1023/A:1005361415496.

[206] B. Bhushan, S. k. Samanta, R. k. Jain, Indigo production by naphthalene-degrading bacteria, Letters in Applied Microbiology. 31 (2000) 5–9. https://doi.org/10.1046/j.1472-765x.2000.00754.x.

[207] D. Alemayehu, L.M. Gordon, M.M. O'Mahony, N.D. O'Leary, A.D.W. Dobson, Cloning and functional analysis by gene disruption of a novel gene involved in indigo production and fluoranthene metabolism in Pseudomonas alcaligenes PA-10, FEMS Microbiology Letters. 239 (2004) 285–293. https://doi.org/10.1016/j.femsle.2004.08.046.

[208] H. Pathak, D. Madamwar, Biosynthesis of Indigo Dye by Newly Isolated Naphthalene-Degrading Strain Pseudomonas sp. HOB1 and its Application in Dyeing Cotton Fabric, Appl Biochem Biotechnol. 160 (2010) 1616–1626. https://doi.org/10.1007/s12010-009-8638-4.

[209] Y. Qu, W. Pi, F. Ma, J. Zhou, X. Zhang, Influence and optimization of growth substrates on indigo formation by a novel isolate Acinetobacter sp. PP-2, Bioresource Technology. 101 (2010) 4527–4532. https://doi.org/10.1016/j.biortech.2010.01.033.

[210] Y. Qu, X. Zhang, Q. Ma, F. Ma, Q. Zhang, X. Li, H. Zhou, J. Zhou, Indigo biosynthesis by Comamonas sp. MQ, Biotechnol Lett. 34 (2012) 353–357. https://doi.org/10.1007/s10529-011-0778-2.

[211] J.P.R. Mercadal, P. Isaac, F. Siñeriz, M.A. Ferrero, Indigo production by Pseudomonas sp. J26, a marine naphthalene-degrading strain, Journal of Basic Microbiology. 50 (2010) 290–293. https://doi.org/10.1002/jobm.200900276.

[212] H.S. Choi, J.K. Kim, E.H. Cho, Y.C. Kim, J.I. Kim, S.W. Kim, A novel flavin-containing monooxygenase from Methylophaga sp. strain SK1 and its indigo synthesis in Escherichia coli, Biochemical and Biophysical Research Communications. 306 (2003) 930–936. https://doi.org/10.1016/S0006-291X(03)01087-8.

[213] A. Singh, N. Singh Chauhan, H.V. Thulasiram, V. Taneja, R. Sharma, Identification of two flavin monooxygenases from an effluent treatment plant sludge metagenomic library, Bioresource Technology. 101 (2010) 8481–8484. https://doi.org/10.1016/j.biortech.2010.06.025.

[214] S.P.L. Ameria, H.S. Jung, H.S. Kim, S.S. Han, H.S. Kim, J.H. Lee, Characterization of a flavin-containing monooxygenase from Corynebacterium glutamicum and its application to production of indigo and indirubin, Biotechnol Lett. 37 (2015) 1637–1644. https://doi.org/10.1007/s10529-015-1824-2.

[215] L. Cheng, S. Yin, M. Chen, B. Sun, S. Hao, C. Wang, Enhancing Indigo Production by Over-Expression of the Styrene Monooxygenase in Pseudomonas putida, Curr Microbiol. 73 (2016) 248–254. https://doi.org/10.1007/s00284-016-1055-3.

[216] T. Heine, C. Großmann, S. Hofmann, D. Tischler, Indigoid dyes by group E monooxygenases: mechanism and biocatalysis, Biological Chemistry. 400 (2019) 939–950. https://doi.org/10.1515/hsz-2019-0109.

[217] E.M.J. Gillam, A.M.A. Aguinaldo, L.M. Notley, D. Kim, R.G. Mundkowski, A.A. Volkov, F.H. Arnold, P. Souček, J.J. DeVoss, F.P. Guengerich, Formation of Indigo by Recombinant Mammalian Cytochrome P450, Biochemical and Biophysical Research Communications. 265 (1999) 469–472. https://doi.org/10.1006/bbrc.1999.1702.

[218] S. Brixius-Anderko, F. Hannemann, M. Ringle, Y. Khatri, R. Bernhardt, An indole-deficient Escherichia coli strain improves screening of cytochromes P450 for biotechnological applications, Biotechnology and Applied Biochemistry. 64 (2017) 315–326. https://doi.org/10.1002/bab.1488.

[219] Q.-S. Li, U. Schwaneberg, P. Fischer, R.D. Schmid, Directed Evolution of the Fatty-Acid Hydroxylase P450 BM-3 into an Indole-Hydroxylating Catalyst, Chemistry – A European Journal. 6 (2000) 1531–1536. https://doi.org/10.1002/(SICI)1521-3765(20000502)6:9<1531::AID-CHEM1531>3.0.CO;2-D.

[220] J. Kim, P. Lee, E. Jung, B.-G. Kim, In vitro characterization of CYP102G4 from Streptomyces cattleya: A self-sufficient P450 naturally producing indigo, Biochimica et Biophysica Acta (BBA) - Proteins and Proteomics. 1866 (2018) 60–67. https://doi.org/10.1016/j.bbapap.2017.08.002.

[221] H. Wang, Z. Wang, C. Wei, J. Wang, Y. Xu, G. Bai, Q. Yao, L. Zhang, Y. Chen, Anticancer potential of indirubins in medicinal chemistry: Biological activity, structural modification, and structure-activity relationship, European Journal of Medicinal Chemistry. 223 (2021) 113652. https://doi.org/10.1016/j.ejmech.2021.113652.

[222] T. Kunikata, T. Tatefuji, H. Aga, K. Iwaki, M. Ikeda, M. Kurimoto, Indirubin inhibits inflammatory reactions in delayed-type hypersensitivity, European Journal of Pharmacology. 410 (2000) 93–100. https://doi.org/10.1016/S0014-2999(00)00879-7.

[223] M. Schäfer, M.L. Semmler, T. Bernhardt, T. Fischer, V. Kakkassery, R. Ramer, M. Hein, S. Bekeschus, P. Langer, B. Hinz, S. Emmert, L. Boeckmann, Small Molecules in the Treatment of Squamous Cell Carcinomas: Focus on Indirubins, Cancers. 13 (2021) 1770. https://doi.org/10.3390/cancers13081770.

[224] D. Minerdi, I. Zgrablic, S.J. Sadeghi, G. Gilardi, Identification of a novel Baeyer-Villiger monooxygenase from Acinetobacter radioresistens: close relationship to the Mycobacterium tuberculosis prodrug activator EtaA, Microbial Biotechnology. 5 (2012) 700–716. https://doi.org/10.1111/j.1751-7915.2012.00356.x.

[225] D. Minerdi, I. Zgrablic, S. Castrignanò, G. Catucci, C. Medana, M.E. Terlizzi, G. Gribaudo, G. Gilardi, S.J. Sadeghi, Escherichia coli Overexpressing a Baeyer-Villiger Monooxygenase from Acinetobacter radioresistens Becomes Resistant to Imipenem, Antimicrobial Agents and Chemotherapy. 60 (2015) 64–74. https://doi.org/10.1128/AAC.01088-15.

[226] G. Catucci, I. Zgrablic, F. Lanciani, F. Valetti, D. Minerdi, D.P. Ballou, G. Gilardi, S.J. Sadeghi, Characterization of a new Baeyer-Villiger monooxygenase and conversion to a solely N-or S-oxidizing enzyme by a single R292 mutation, Biochimica et Biophysica Acta (BBA) - Proteins and Proteomics. 1864 (2016) 1177–1187. https://doi.org/10.1016/j.bbapap.2016.06.010.

[227] G.H. Han, G.H. Gim, W. Kim, S.I. Seo, S.W. Kim, Enhanced indirubin production in recombinant Escherichia coli harboring a flavin-containing monooxygenase gene by cysteine supplementation, Journal of Biotechnology. 164 (2013) 179–187. https://doi.org/10.1016/j.jbiotec.2012.08.015.

[228] E. Banoglu, G.G. Jha, R.S. King, Hepatic microsomal metabolism of indole to indoxyl, a precursor of indoxyl sulfate, Eur. J. Drug Metab. Pharmacokinet. 26 (2001) 235–240. https://doi.org/10.1007/BF03226377.

[229] G. Lano, S. Burtey, M. Sallée, Indoxyl Sulfate, a Uremic Endotheliotoxin, Toxins. 12 (2020) 229. https://doi.org/10.3390/toxins12040229.

[230] S.C. Leong, T.L. Sirich, Indoxyl Sulfate—Review of Toxicity and Therapeutic Strategies, Toxins. 8 (2016) 358. https://doi.org/10.3390/toxins8120358.

[231] C. Gao, G. Catucci, G. Gilardi, S.J. Sadeghi, Binding of methimazole and NADP(H) to human FMO3: In vitro and in silico studies, International Journal of Biological Macromolecules. 118 (2018) 460–468. https://doi.org/10.1016/j.ijbiomac.2018.06.104.

[232] J.R. Cashman, Y. Xiong, J. Lin, H. Verhagen, G. van Poppel, P.J. van Bladeren, S. Larsen-Su, D.E. Williams, In vitro and in vivo inhibition of human flavin-containing monooxygenase form 3 (FMO3) in the presence of dietary indoles, Biochemical Pharmacology. 58 (1999) 1047–1055. https://doi.org/10.1016/S0006-2952(99)00166-5.

[233] F. Valetti, S.J. Sadeghi, Y.T. Meharenna, S.R. Leliveld, G. Gilardi, Engineering multi-domain redox proteins containing flavodoxin as bio-transformer: preparatory studies by rational design, Biosensors and Bioelectronics. 13 (1998) 675–685. https://doi.org/10.1016/S0956-5663(98)00021-9.

[234] G. Catucci, S. Turella, H. Cheropkina, M. De Angelis, G. Gilardi, S.J. Sadeghi, Green production of indigo and indirubin by an engineered Baeyer–Villiger monooxygenase, Biocatalysis and Agricultural Biotechnology. 44 (2022) 102458. https://doi.org/10.1016/j.bcab.2022.102458.

[235] S.P. Hanlon, A. Camattari, S. Abad, A. Glieder, M. Kittelmann, S. Lütz, B. Wirz, M. Winkler, Expression of recombinant human flavin monooxygenase and moclobemide-N-oxide synthesis on multi-mg scale, Chem. Commun. 48 (2012) 6001–6003. https://doi.org/10.1039/C2CC17878H.

[236] R. Oeggl, T. Neumann, J. Gätgens, D. Romano, S. Noack, D. Rother, Citrate as Cost-Efficient NADPH Regenerating Agent, Frontiers in Bioengineering and Biotechnology. 6 (2018). https://www.frontiersin.org/articles/10.3389/fbioe.2018.00196 (accessed October 23, 2022).

[237] E. Krieger, G. Vriend, Models@Home: distributed computing in bioinformatics using a screensaver based approach, Bioinformatics. 18 (2002) 315–318. https://doi.org/10.1093/bioinformatics/18.2.315.

[238] E. Romero, J.R.G. Castellanos, A. Mattevi, M.W. Fraaije, Characterization and Crystal Structure of a Robust Cyclohexanone Monooxygenase, Angewandte Chemie International Edition. 55 (2016) 15852–15855. https://doi.org/10.1002/anie.201608951.

[239] G. Catucci, G. Gilardi, L. Jeuken, S.J. Sadeghi, In vitro drug metabolism by C-terminally truncated human flavin-containing monooxygenase 3, Biochemical Pharmacology. 83 (2012) 551–558. https://doi.org/10.1016/j.bcp.2011.11.029.

[240] E.F. Pettersen, T.D. Goddard, C.C. Huang, G.S. Couch, D.M. Greenblatt, E.C. Meng, T.E. Ferrin, UCSF Chimera—A visualization system for exploratory research and analysis, Journal of Computational Chemistry. 25 (2004) 1605–1612. https://doi.org/10.1002/jcc.20084.

[241] G.H. Han, S.E. Bang, B.K. Babu, M. Chang, H.-J. Shin, S.W. Kim, Bio-indigo production in two different fermentation systems using recombinant Escherichia coli cells harboring a flavin-containing monooxygenase gene (fmo), Process Biochemistry. 46 (2011) 788–791. https://doi.org/10.1016/j.procbio.2010.10.015.

[242] H.-J. Kim, S. Jang, J. Kim, Y.-H. Yang, Y.-G. Kim, B.-G. Kim, K.-Y. Choi, Biosynthesis of indigo in Escherichia coli expressing self-sufficient CYP102A from Streptomyces cattleya, Dyes and Pigments. 140 (2017) 29–35. https://doi.org/10.1016/j.dyepig.2017.01.029.

[243] J. Du, D. Yang, Z.W. Luo, S.Y. Lee, Metabolic engineering of Escherichia coli for the production of indirubin from glucose, Journal of Biotechnology. 267 (2018) 19–28. https://doi.org/10.1016/j.jbiotec.2017.12.026.

[244] D.E.T. Pazmiño, R. Snajdrova, D.V. Rial, M.D. Mihovilovic, M.W. Fraaije, Altering the Substrate Specificity and Enantioselectivity of Phenylacetone Monooxygenase by Structure-Inspired Enzyme Redesign, Advanced Synthesis & Catalysis. 349 (2007) 1361–1368. https://doi.org/10.1002/adsc.200700045.

[245] J. Kim, J. Lee, P.-G. Lee, E.-J. Kim, W. Kroutil, B. Kim, Elucidating Cysteine-Assisted Synthesis of Indirubin by a Flavin-Containing Monooxygenase, ACS Catal. 9 (2019) 9539–9544. https://doi.org/10.1021/acscatal.9b02613.

[246] V. Joosten, W.J. van Berkel, Flavoenzymes, Current Opinion in Chemical Biology. 11 (2007) 195–202. https://doi.org/10.1016/j.cbpa.2007.01.010.

[247] H.J. Cho, H.Y. Cho, K.J. Kim, M.H. Kim, S.W. Kim, B.S. Kang, Structural and functional analysis of bacterial flavin-containing monooxygenase reveals its ping-pong-type reaction mechanism, Journal of Structural Biology. 175 (2011) 39–48. https://doi.org/10.1016/j.jsb.2011.04.007.

[248] Q. Sun, J. Leng, L. Tang, L. Wang, C. Fu, A Comprehensive Review of the Chemistry, Pharmacokinetics, Pharmacology, Clinical Applications, Adverse Events, and Quality Control of Indigo Naturalis, Frontiers in Pharmacology. 12 (2021). https://www.frontiersin.org/articles/10.3389/fphar.2021.664022 (accessed October 23, 2022).

# Acknowledgements

There are many people to acknowledge who have helped me over my years as a PhD student. The work in this dissertation would not have been possible without the technical and personal support from these many individuals.

First, I would like to express my sincere and warm gratitude to my supervisor, Prof. Sheila J. Sadeghi, who have always encouraged me to have confidence in the work I have done and what I was capable of doing. She allowed me to pursue projects that I was particularly interested in while always guiding me toward success. I firmly believe I would not have accomplished the completion of this work without her advice and example.

I am grateful to Prof. Gianfranco Gilardi for the discussions during group meetings that helped me sort out the technical and scientific details of my work. It was an honor for me to be a part of the research group under his supervision.

Additionally, I would like to thank the members of my dissertation committee, Dr. Caroline Emilie Paul, Dr. Giulia Di Rocco, Prof. Frank Hollmann and Prof. Antonio Ranieri. Their guidance has directly helped me through constructive criticism to improve the scientific path of this dissertation.

With all my heart I am grateful to Prof. Galina Dovbeshko, Prof. Gianmario Martra and Dr. Pavlo Ivanchenko, who always believed in my ability to be successful in the scientific area.

I am indebted to my colleagues for supporting me all these years. Many thanks for all these good moments to Prof. Giovanna Di Nardo, Prof. Francesca Valetti, Dr. Gianluca Catucci, Dr. Oleksii Skorokhod, Dr. Elena Gazzano, Dr. Silvia Castrignano, Dr. Arianna Marucco, Dr. Danilo Correddu, Dr. Jose Francisco Gasteazoro Pineiro, Dr. Chao Zhang, Alessandro Della Costa, Simone Turella, Daniele Giuriato, Sabrina Helmy Aly, and to my dear Claudia Grillo who became my best friend and who gave me huge support in the most difficult moments.

I would like to thank my family for their personal and emotional support during all this time, for their love and for patiently waiting for all these years. Their words of encouragement and constant support made this all possible.